Observations and Assessment of Iron Oxide Nanoparticles in Metal-Polluted Mine Drainage within a Steep Redox Gradient, and a Comparison to Synthetic Analogs

Carol A. Johnson

Dissertation submitted to the faculty of the Virginia Polytechnic Institute and State University in partial fulfillment of the requirements for the degree of

Doctor of Philosophy
In
Geosciences

Michael F. Hochella, Jr, chair
Bojeong Kim
Mitsuhiro Murayama
Amy J. Pruden-Bagchi
J. Donald Rimstidt
Madeline E. Schreiber

August 28, 2014
Blacksburg, VA

Keywords: green rust, ferrihydrite, iron cycling, contaminant uptake, polycrystallinity, transmission electron microscopy, crystal growth, silica

OBSERVATIONS AND ASSESSMENT OF IRON OXIDE NANOPARTICLES IN METAL-POLLUTED MINE DRAINAGE WITHIN A STEEP REDOX GRADIENT, AND A COMPARISON TO SYNTHETIC ANALOGS

Carol A. Johnson

ABSTRACT

The complex interactions at the interfaces of minerals, microbes, and metals drive the cycling of iron and the fate and transport of metal(loid)s in contaminated systems. The former uranium mine near Ronneburg, Germany is one such system, where slightly acidic mine drainage crossing a steep redox gradient (groundwater outflow into a stream) forms and transforms iron (oxy)hydroxide nanoparticles. These particles interact with toxic metal(loid)s in water and sediments. Iron oxidizing and reducing bacteria also play a role in these processes. Biogeochemical reactions are influenced by nanoscale properties, and thus it is critical to probe environmental samples with appropriate techniques such as analytical transmission electron microscopy (TEM). This dissertation presents two studies on the iron (oxy)hydroxide mineral nanoparticles found in the Ronneburg mine drainage system.

The first study uses TEM in conjunction with bulk analytical techniques to demonstrate the complexity of iron (oxy)hydroxide transformations at the steep redox gradient, and the partitioning of metal(loid)s within those mineral phases. An important result was the identification of Zn-bearing green rust platelets in the anoxic outflow water. Green rust minerals have only been identified in nature a handful of times, and we believe this work to be only the second to examine naturally occurring green rust using high resolution TEM (HR-TEM). Downstream of the outflow, aggregates of poorly crystalline iron oxide spheroids co-precipitated with amorphous silica formed and settled to the stream bed, where they aged to form nanoparticulate goethite and sequestered metals such as As and Zn. However, significant concentrations of Zn and Ni remained in the dissolved/nano (< 0.1 um) water fraction and continued downstream.

The second study demonstrates that natural green rust nanoparticles and their synthetic analogs can be complex polycrystalline phases composed of crystallites only a few nanometers in size, and often include nano-regions of amorphous material. In addition to the typical pseudo-hexagonal platelet morphology, green rust nanorods were synthesized, which has not previously been reported. This work has important implications for the reactivity of green rust with biogeochemical interfaces in natural, anthropogenic, and industrial systems.

A third study, presented in the appendix, characterizes the bacterial community at the Ronneburg mine drainage site and highlights iron oxidizers such as *Gallionella* sp., in particular those that form stalks of iron oxide nanoparticles. These biogenic stalks also contribute to the uptake of metal contaminants in water and sediments.

The science of iron cycling is complex. It requires field-based exploration to enrich the contributions made by experimental, laboratory and modeling studies. This dissertation adds another chapter in the search for filling in missing pieces of this interconnected system.

ACKNOWLEDGEMENTS

First and foremost I thank my advisor, Mike Hochella, for his guidance and mentorship these past six years. He let me take the reins of my entire dissertation and have true ownership of it, as an independent scientist. I thank Kirsten Küsel at the FSU Jena, Germany for welcoming me into her lab for eight months in 2011, for letting me work so closely with her students, and for pushing me to go into the field that last time in October when I didn't want to. It was an absolute pleasure working as a team with Maria Fabisch and Gina Freyer. I thank all the scientists at FSU Jena who helped me in some way with instrumentation and field work assistance. And of course, thanks to the entire Küsel research group for your support and friendship during my stay in a foreign land, and putting up with my German.

I have many people to thank for helping me gain expertise with TEM, a very difficult instrument to master: Mitsu Murayama, Chris Winkler, Steve McCartney and Niven Monsegue at the ICTAS NCFL at Virginia Tech, and Andras Kovacs at the Ernst Ruska Centre in Jülich, Germany.

I cannot thank enough my amazing colleagues and friends, past and present. The Environmental Nanoscience and Technology (ENT) lab members (from multiple departments) inspired me with their intelligence and high standards to do interdisciplinary research. The members of the Hochella, Dove, Schreiber, and Michel groups in the Dept. of Geosciences were also incredibly helpful and supportive. Thanks especially to Rebecca French for mentoring me and being a great friend. Thanks to my committee for their support and constructive criticism, and to the support staff at the Dept. of Geosciences and ICTAS for all that they do.

Finally, thanks to my family for bringing me up as an independent woman, and to Param Pati and our dog Lucy for their love and keeping me sane.

ATTRIBUTIONS

Several colleagues and collaborators aided in the research and writing for the manuscripts produced from this dissertation. A brief description of their contributions is below.

Prof. Michael F. Hochella Jr. (Dept. of Geosciences, Virginia Tech) was the primary research advisor and PhD committee chair. He provided general scientific guidance and support with writing all of the chapters, as well as financial support.

Prof. Kirsten Küsel (Institute of Ecology, Friedrich Schiller University Jena, Germany) was the supervisor for my research stay in Germany for eight months in 2011. She provided general scientific guidance and support with writing Chapter 2 and Appendices D and E.

Prof. Mitsuhiro Murayama (Dept. of Materials Science and Engineering, Virginia Tech) was a committee member and provided substantial assistance through discussions and editing of Chapter 3. He also collected some TEM data.

Maria Fabisch (Ph.D. candidate) and **Gina Freyer** (M.Sc.) (Institute of Ecology, Friedrich Schiller University Jena, Germany) were close collaborators for all fieldwork, sample preparation, and editing for Chapter 2. Appendices D and E are a part of Maria's Ph.D. dissertation.

Dr. Manuel Caraballo (former Postdoc in Dept. of Geosciences, Virginia Tech) provided guidance with sequential extraction, extensive assistance with interpretation of geochemical data and helped edit Chapter 2.

TABLE OF CONTENTS

LIST OF FIGURES

LIST OF TABLES

1. INTRODUCTION

In early 2011, the former uranium mine near Ronneburg, Germany had a very visible, concerning problem – contaminated drainage water from the underground mine had flooded a drainage creek, overwhelming the containment systems that were in place. The cloudy-orange suspension spilled over the small dam and flowed downstream, through small towns and eventually into a river in the city of Gera. As is common for mine drainage areas, the orange precipitates were iron oxides, and the nature of this particular outflow provided a unique opportunity to study the iron oxide geochemistry through a very sharp redox boundary as the mine drainage crossed the transition zone between the anoxic subsurface and the oxic surface. This led to the following questions: How were the orange iron oxide particles forming and transforming as they crossed this transition zone? Were these particles playing a role in the transport of metal contaminants downstream? Or were the contaminant metals being sequestered in the creek sediments? My collaborators, geomicrobiologists at the Friedrich Schiller University Jena (Germany), and I sought answers to these questions. The geomicrobiologists focused on the role of iron-oxidizing bacteria, while I studied the nanoscale structure of the iron oxide particles in the drainage water and underlying sediments at this site.

Similar scenarios of mine drainage affecting downstream environments happen all over the world, related to all types of mining operations. Acid mine drainage (AMD) occurs when sulfate-reducing bacteria, oxygen and water react with displaced waste rock to form sulfuric acid. This acid dissolves minerals, and releases metals and metalloids that are often a serious environmental and human health concern. Iron is the most abundant metal in these systems, and iron oxy(hydroxide) nanoparticles which commonly form in these environments are known to be highly reactive towards coexisting metal(loid) contaminants. They often carry toxic metals great

distances from the source (Hassellöv and von der Kammer 2008; Plathe et al. 2010; Guo and Barnard 2013). Nanoparticles differ from larger materials in that although they may exhibit essentially the same internal composition and structure, they express a wide range of physical and chemical properties depending on their exact size and shape (Waychunas et al. 2005; Hochella et al. 2008). The size limit for this 'nanobehavior' is typically only up to a few tens of nanometers in at least one dimension (Hochella et al. 2008).

There is a great need for the continued study of nanoparticles and their behavior in environmental settings in order to inform future laboratory studies and help close the lab-to-field extrapolation gap. Vignati et al. (2007) proposed a conceptual strategy for this general scenario starting with the identification of the issue, then performing carefully-planned fieldwork, followed by laboratory studies with environmentally-relevant conditions which can be used to propose a model, and iterative feedback loops to validate the model. Starting with laboratory experiments can provide interesting insights into chemical behavior in simple systems, but it is difficult to extrapolate to more complex systems and prove environmental relevance. Thus, in this dissertation work I started with field studies, then pursued one interesting aspect with a more simplistic laboratory system. Since the primary analysis tool, electron microscopy, does not allow for in situ measurements of the particles in the environmental system, I used sampling methods to obtain nanoparticles from both oxic and anoxic waters and sediments to be as representative as reasonably possible. Transmission electron microscopy (TEM) grids of oxidized waters were prepared in the field, and anoxic water and sediment samples were prepared within 24 hours in an anoxic chamber.

In the second chapter of this dissertation, I demonstrate the complexity of the formation and transformation of iron oxy(hydroxide) nanoparticles within the steep redox gradient of

groundwater outflow into a stream at the former uranium mine near Ronneburg, Germany. In addition, the role of these nanoparticles in metal(loid) uptake and transport was also evaluated. A major finding was the identification and nanoscale analysis of pseudo-hexagonal nanoplatelets of Zn-bearing green rust in the outflowing groundwater. Green rust is rarely observed in the environment due to its rapid oxidation in air (Legrand et al. 2004; Wang et al. 2013), and it has remained highly elusive for years. Anoxic preparation of outflow water and all sediment samples was critical in order to capture and preserve green rust. As scientists have discovered with other elusive and metastable minerals such as ferrihydrite and schwertmannite (Bigham and Nordstrom 2000; Hochella 2005; Gautier et al. 2006; Benzerara et al. 2011; Marescotti et al. 2012 and references therein), these phases can be key in the biogeochemical cycling of iron and other elements, as well as pollutant uptake and transformation processes (Poincare et al. 2000; Pepper et al. 2003; Chaves et al. 2007), and we believe that green rust is no exception to this principle.

A variety of analytical tools across multiple scales were used to characterize the elemental composition and structure of nanoparticles from the water and sediment that I studied, including X-ray diffractometry (XRD), inductively-coupled-plasma mass spectrometry (ICP-MS) of filtered water fractions and sequentially-extracted sediments, and transmission electron microscopy (TEM) including energy dispersive X-ray spectroscopy (EDS), selected area electron diffraction (SAED), and high resolution (HR) imaging. Using these techniques, I was able to provide some insights into the complexity of iron oxide materials in such a dynamic system far from equilibrium, and try to reconcile the broad results from bulk techniques with the unique nanoscale features observed.

Indeed, the aggregates of iron (oxy)hydroxide nanoparticles and colloids were involved in metal(loid) uptake and collection in the creek bank and bottom sediments, though major metals such as Zn and Ni were found primarily in the dissolved and nano (< 100 nm) water fraction. At less than 100 nm in this study, we did not differentiate the smallest nanoparticle fraction with those species that were fully dissolved. Nanospheres of poorly crystalline iron oxides in the water grew larger and formed goethite nanoneedles at their surfaces after sedimentation and aging, which could result in a greater reactive surface for metal(loid) uptake. Amorphous silica co-precipitation with the iron oxides was also prevalent throughout the samples, though the effect on metal(loid) sorption was not determined. This study, titled "Observations and assessment of iron oxide and green rust nanoparticles in metal-polluted mine drainage within a steep redox gradient," was published in *Environmental Chemistry* in August 2014.

The green rust discovered in the Ronneburg mine drainage area showed several fascinating structural features, and this made it well worth examining in detail for the final part of this dissertation. Detailed TEM studies of green rust are rare, especially for natural samples (Zegeye et al. 2012). All previously published work seems to imply that pseudo-hexagonal green rusts are single crystals. However, as we show in chapter 3, they are in fact not coherent structures but polycrystalline mosaics that are often misaligned crystallographically. In addition to the TEM techniques used in the field study, for the first time dark field (DF) imaging was applied to green rust minerals to pinpoint the areas of different crystallographic orientation. In addition to examining natural green rusts in outflow water and sediment, sulfate green rust was synthesized in the laboratory in order to compare its nanoscale structure and determine if it is a reasonable analog to natural samples. The morphology varied with different synthesis conditions,

and a new nanorod morphology was discovered which was previously unknown for green rust. However, the pseudo-hexagonal platelets of sulfate green rust synthesized in the presence of amorphous silica had similar polycrystalline mosaic textures to natural green rust materials and could therefore be considered reasonable analogs. This study is in preparation for submission to *American Mineralogist*.

Detailed studies of iron oxide nanoparticle and colloidal behavior such as this should be of particular interest to scientists studying contaminant transport and remediation, element cycling by microbes, fate and transport of engineered metal oxide nanoparticles in the environment, and those trying to bridge laboratory experiments with the natural environment. The characterization of nanoparticles and colloids from dynamic, complex environmental systems at multiple scales allows for a more robust view on iron oxide evolution and interaction with metal(loid) contaminants. In addition, this dissertation provides the most comprehensive study to date on the nanoscale nature of both natural and synthetic green rusts, which will help scientists in the future to understand their behavior in environmental systems.

In addition to the work presented in the following two chapters of this dissertation, I contributed to other projects involving metal-mineral-microbe interactions at the former Ronneburg mine in Germany. I have included one co-authored paper in Appendix D, titled "Dominance of '*Gallionella capsiferriformans*' and heavy metal retention by stalk-forming iron oxidizers in metal-rich mine water discharge", which was recently submitted to *Geobiology*. I contributed to this work by 1) sampling and helping to extract the DNA from some of the water and sediment samples, and 2) developing the method to prepare TEM grids of *Gallionella*-like stalks after collection onto glass slides *in situ*, and analyzing those stalks by TEM.

Our understanding of the fate and transport of metal contaminants in the former

Ronneburg uranium mining district has greatly benefitted from the combination of geoscience, chemistry, microbiology, and materials science knowledge and approaches. Interdisciplinary collaborations such as these are critically important in order to fully respect the wide variety of interactions in complex systems.

1.1. References

Benzerara, K., Miot, J., Morin, G., Ona-Nguema, G., Skouri-Panet, F., and Férard, C. (2011) Significance, mechanisms and environmental implications of microbial biomineralization. Comptes Rendus Geoscience, 343, 160–167.

Bigham, J.M., and Nordstrom, D.K. (2000) Iron and Aluminum Hydroxysulfates from Acid Sulfate Waters. In C.N. Alpers, J.L. Jambor, and D.K. Nordstrom, Eds., Reviews in Mineralogy and Geochemistry: Sulfate minerals: crystallography, geochemistry, and environmental significance pp. 351–403. Mineralogical Society of America.

Chaves, L.H.G., Curry, J.E., Stone, D.A., and Chorover, J. (2007) Fate of nickel ion in (II-III) hydroxysulphate green rust synthesized by precipitation and coprecipitation. Revista Brasileira de Ciência do Solo, 31, 813–818.

Gautier, J., Grosbois, C., Floc'h, J.P., and Martin, F. (2006) Transformation of natural As-associated ferrihydrite downstream of a remediated mining site. European Journal of Mineralogy, 18, 187–195.

Guo, H., and Barnard, A.S. (2013) Naturally occurring iron oxide nanoparticles: morphology, surface chemistry and environmental stability. Journal of Materials Chemistry A, 1, 27.

Hassellöv, M., and von der Kammer, F. (2008) Iron oxides as geochemical nanovectors for metal transport in soil-river systems. Elements, 4, 401–406.

Hochella Jr, M.F., Lower, S.K., Maurice, P.A., Penn, R.L., Sahai, N., Sparks, D.L., and Twining, B.S. (2008) Nanominerals, mineral nanoparticles, and Earth systems. Science, 319, 1631–5.

Hochella Jr, M.F. (2005) Environmentally important, poorly crystalline Fe/Mn hydrous oxides: Ferrihydrite and a possibly new vernadite-like mineral from the Clark Fork River Superfund Complex. American Mineralogist, 90, 718–724.

Legrand, L., Mazerolles, L., and Chaussé, A. (2004) The oxidation of carbonate green rust into ferric phases:solid-state reaction or transformation via solution. Geochimica et Cosmochimica Acta, 68, 3497–3507.

Marescotti, P., Carbone, C., Comodi, P., Frondini, F., and Lucchetti, G. (2012) Mineralogical and chemical evolution of ochreous precipitates from the Libiola Fe–Cu-sulfide mine (Eastern Liguria, Italy). Applied Geochemistry, 27, 577–589.

Pepper, S.E., Bunker, D.J., Bryan, N.D., Livens, F.R., Charnock, J.M., Pattrick, R.A.D., and Collison, D. (2003) Treatment of radioactive wastes: An X-ray absorption spectroscopy study of the reaction of technetium with green rust. Journal of Colloid and Interface Science, 268, 408–412.

Plathe, K.L., von der Kammer, F., Hassellöv, M., Moore, J., Murayama, M., Hofmann, T., and Hochella, M.F. (2010) Using FlFFF and aTEM to determine trace metal–nanoparticle associations in riverbed sediment. Environmental Chemistry, 7, 82.

Poincare, H., Loyaux-Lawniczak, S., Refait, P., Ehrhardt, J.-J., Lecomte, P., and Genin, J.-M.R. (2000) Trapping of Cr by formation of ferrihydrite during the reduction of chromate ions by Fe(II) - Fe(III) hydroxysalt green rusts. Environmental Science & Technology, 34, 438–443.

Vignati, D.A.L., Ferrari, B.J.D., and Dominik, J. (2007) Laboratory-to-field extrapolation in aquatic sciences. Environmental Science & Technology, 41, 1067–1073.

Wang, X., Liu, F., Tan, W., Feng, X., and Koopal, L.K. (2013) Transformation of hydroxycarbonate green rust into crystalline iron (hydr)oxides: Influences of reaction conditions and underlying mechanisms. Chemical Geology, 351, 57–65.

Waychunas, G.A., Kim, C.S., and Banfield, J.F. (2005) Nanoparticulate iron oxide minerals in soils and sediments: unique properties and contaminant scavenging mechanisms. Journal of Nanoparticle Research, 7, 409–433.

Zegeye, A., Bonneville, S., Benning, L.G., Sturm, A., Fowle, D.A., Jones, C., Canfield, D.E., Ruby, C., MacLean, L.C., Nomosatryo, S., and others (2012) Green rust formation controls nutrient availability in a ferruginous water column. Geology, 40, 599–602.

2. OBSERVATIONS AND ASSESSMENT OF IRON OXIDE AND GREEN RUST NANOPARTICLES IN METAL-POLLUTED MINE DRAINAGE WITHIN A STEEP REDOX GRADIENT

Carol A. Johnson,[A,B,F] Gina Freyer,[B] Maria Fabisch,[B] Manuel A. Caraballo,[A,C,D] Kirsten Kusel,[B,E] and Michael F. Hochella Jr[A]

[A]Department of Geosciences, Virginia Tech, 4044 Derring Hall, 1405 Perry Street, Blacksburg, VA 24061, USA.

[B]Institute of Ecology, Friedrich Schiller University Jena, Dornburger Strasse 159, D-07743 Jena, Germany.

[C]Geology Department, University of Huelva, Campus 'El Carmen', Avenida 3 de Marzo s/n, E-21071 Huelva, Spain.

[D]Mining Engineering Department, University of Chile, Avenida Tupper 2069, 8370451 Santiago, Chile.

[E]German Centre for Integrative Biodiversity Research (iDiv) Halle-Jena-Leipzig, Deutscher Platz 5e, D-04103 Leipzig, Germany.

Environmental Chemistry. **2014**, *11*, 377–391.
http://www.publish.csiro.au/nid/188/paper/EN13184.htm

2.1. Environmental context

Legacy contamination from mining operations is a serious and complex environmental problem. We examine a former uranium mine where groundwater leaving the site enters a stream with chemically dramatic effects resulting in a fundamental change in the way contaminant metals are transported to the surface environment. The results are important for our understanding of how these contaminants are dispersed, and how they could interact with the biosphere.

2.2. Abstract

In this study of iron- and silica-bearing nanoparticle and colloid aggregates in slightly acidic mine drainage, we combine bulk scale geochemistry techniques with detailed nanoscale analyses using high-resolution transmission electron microscopy (HR-TEM) to demonstrate the

complexity of iron oxide formation and transformation at a steep redox gradient (groundwater outflow into a stream), and the resulting role in metal(loid) uptake. We also identified pseudohexagonal nanosheets of Zn-bearing green rust in outflowing groundwater using HR-TEM. This is only the second study where green rust has been identified in groundwater, and the second to examine naturally occurring green rust with analytical TEM. In aerated downstream waters, we found aggregates of 20–200 nm of poorly crystalline iron oxide particles. Inductively coupled plasma–mass spectrometry (ICP-MS) analysis of water fractions shows that most elements such as Ni and Zn are found almost exclusively in the dissolved–nanoparticulate (<0.1 μm) fraction, whereas Cu and As were primarily associated with suspended particles. In the underlying sediments composed of deposited particles, goethite nanoneedles formed on the ferrihydrite surfaces of larger aggregated particles (100–1000 nm), resulting in more reactive surface area for metal(loid) uptake. Sequential extraction of sediments shows that many metal(loid)s, particularly As and Zn, are associated with iron oxides identified as ferrihydrite–schwertmannite and goethite. Amorphous silica co-precipitation with iron oxides is prevalent at all sampling sites, but its effect on metal(loid) sorption is unknown.

2.3. Introduction

Earth scientists have become deeply interested in probing the role of nanosized materials in the environment, especially in the last 15 years. Despite efforts to understand the distribution of nanomaterials in the environment (Hochella et al. 2008, 2012), what forms these materials take (Perret et al. 2000; Kim et al. 2010; French et al. 2012; Guo and Barnard 2013; Guo et al. 2013; S.-G. Lu et al. 2013), how they are modified during their lifetime (Perret et al. 2000; Guo and Barnard 2013; Guo et al. 2013) and how they interact with a vast array of living and non-living components of the critical zone (Penn et al. 2001; Carbone et al. 2005; Genovese and

Mellini 2007; Hiemstra et al. 2010; S.-G. Lu et al. 2013), it often seems that more questions are generated than answered. Nanomaterials differ from larger materials in that although they may exhibit essentially the same internal composition and structure, they express a wide range of physical and chemical properties depending on their exact size and shape (Waychunas et al. 2005; Hochella et al. 2008). Examples of material properties that commonly change at the nanoscale include surface reactivity (i.e. sorption and surface complexation), stability, electronic behavior and optical properties. In most cases, the size limit for 'nanobehavior' is only up to a few tens of nanometers in at least one dimension (Hochella et al. 2008). The reactivity of nanoparticles in the 10-nm range can be so important that only a small percentage of those particles can account for the overall reactivity of a system (Hochella et al. 2012). The reactive aspects that are particularly interesting when studying environmental contamination and remediation involving nanomaterials are dissolution–recrystallization and cation–anion sorption. For example, iron oxyhydroxide nanoparticles have been shown to be highly reactive towards metal(loid) pollutants and can carry them great distances from the pollution source (Hassellöv and von der Kammer 2008; Plathe et al. 2010; French et al. 2012; Guo and Barnard 2013).

In order to predict how nanomaterials will interact with the environment, it is critical to understand their characteristics on the nanoscale. Scientists are increasingly using high resolution transmission electron microscopy (HR-TEM) to examine discrete nanoparticle assemblies in nature (Hochella et al. 1999; Banfield et al. 2000; Carbone et al. 2005; Genovese and Mellini 2007; Plathe et al. 2010; French et al. 2012; Marescotti et al. 2012; Lu et al. 2013) and other complex environments (Kim et al. 2010, 2012) because bulk analytical techniques and most other analytic techniques are not sensitive to varying degrees of crystallinity and composition on a nanoparticle-by-nanoparticle basis. Sampling nanomaterials from their native environment and

examining them compositionally and structurally with TEM is as close as scientists can get to visually understanding their real-life complexity. The alternative is to simulate natural conditions in the laboratory. Despite the advantages that this may have, even the most complex simulated natural water or soil column will not account for all components and interactions in a natural system. TEM, along with special sample preparations that are often critical, can complement in situ geochemical measurements as well as traditional bulk characterisation methods in order to understand the role of nanomaterials in complex matrices.

Nanoparticles formed by natural processes, but as a result of highly disturbed environments, are deemed 'incidental nanoparticles'. The role of these incidental nanoparticles to take up co-existing pollutants and transport them downstream can change depending on the geochemical conditions, and there are many knowledge gaps in our understanding of these processes. Metals can be transported by nanoparticles, larger colloids, organic material or stay truly dissolved. Our study follows the lead of some previous studies (Hochella et al. 1999; Carbone et al. 2005; Gautier et al. 2006; Genovese and Mellini 2007; French et al. 2012), which take a nanoscale look at iron oxide nanoparticle formation and subsequent transformation in metal polluted natural waters. A geochemically dynamic metal polluted creek was selected where slightly acid waters transition from an underground anoxic reducing environment to an oxic and slightly more oxidizing one. In this study, analytical TEM was used to lead traditional mineralogy and hydrochemistry techniques in order to (1) identify the structure and composition of inorganic colloids and nanomaterials found in this aqueous environment, (2) characterize the transformations by these colloids and nanomaterials as a result of changes in hydrogeochemical conditions and (3) analyze these colloids and nanomaterials for their associations with metal(loid) contaminants within this slightly acidic aquatic system.

2.4. Materials and methods

2.4.1. Field site background and description

One of the largest uranium mining operations in the world to date took place in eastern Germany between 1945 and German reunification in 1990. The Ronneburg Mining District was the largest mine in the region, included both underground and open pit operations, and produced over 113,000 t of uranium (Paul et al. 2006) primarily through heap-leaching with sulfuric acid. After the mines were closed, two main remediation strategies were implemented at the Ronneburg mine, namely: (1) backfilling of the open pit with waste rock from the leaching heaps, to prevent further acid mine drainage (AMD) and (2) flooding of the underground mine and injection of alkali to buffer the water to a more neutral pH (Paul et al. 2006). As the water table rose, a section of the local drainage creek (Gessen Creek) was blocked off and a pumping station was installed to collect the contaminated outflow water which was then treated at an on-site treatment plant (Paul et al. 2006).

Constituents of special concern include nickel, uranium, sulfate, zinc, cobalt, cadmium and radon (Geletneky et al. 2002; Wismut GmbH 2011). In 2010, the water table rose above the creek level and contaminated water from the underground mine reached the surface at different locations and started to flow down a hillside into the creek. This newly created minewater outflow area expanded and became an ideal site to study the potential generation, transformations and environmental role of iron nanominerals and colloids in metal polluted water in a rapid transition from a reducing and anoxic environment to an oxidising one.

Three sampling sites were chosen (Figure 2.1) along the outflow path to the Gessen Creek and sampled extensively on July 18 and October 25, 2011. The first sampling point was

located where large amounts of groundwater reached the surface and some small limestone boulders for consolidation covered the site. This will be referred to hereafter as the 'outflow' site (Figure 2.1b). The outflow water flows approximately 20 m to the bank of Gessen Creek, where red-orange terraces were actively forming ('terraces' site, Figure 2.1c). The sampling site adjacent to the terraces is referred to as the 'creek' site (Figure 2.1c).

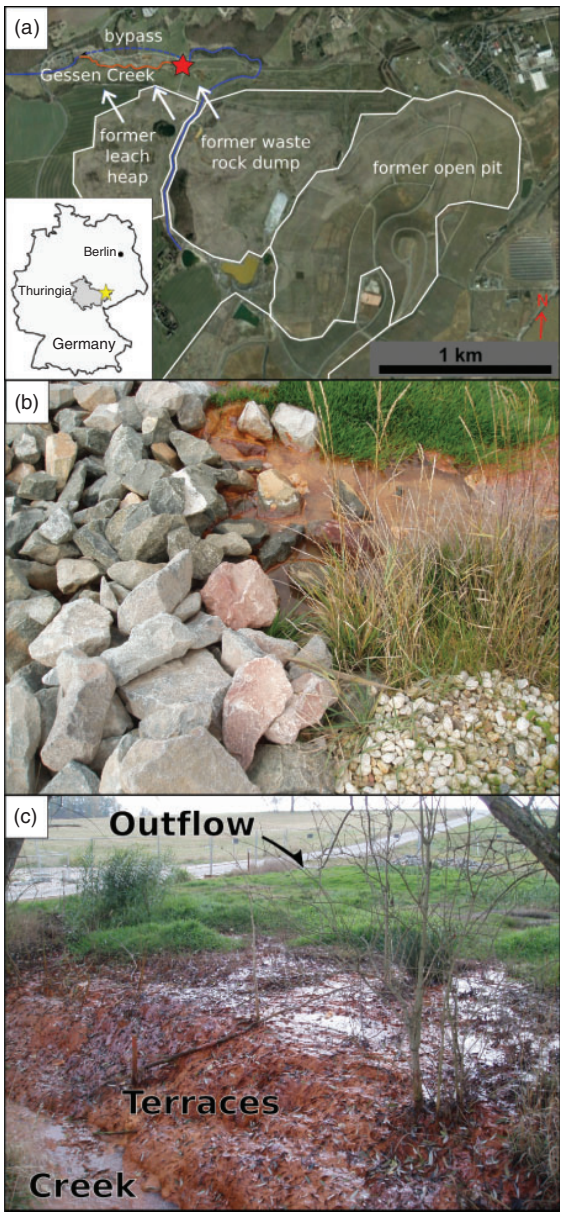

Figure 2.1. a) Satellite view (Google Maps, 2011) of the former Ronneburg uranium mining district; the red star is the sampling location, the light blue arrows show the general direction of the hydrologic gradient, (b) photo of the outflow site in October 2011, (c) photo of the outflow, terraces and creek sites in October 2011.

2.4.2. Water and solid sampling

Water and sediment porewater geochemistry was measured directly in the field using portable meters. The pH was measured using a pH probe (pH330, WTW GmbH, Munich, Germany) with an internal temperature sensor (and SenTix 41, WTW) and calibrated using a three-point curve (4.01, 7.00, 10.00, WTW). Electrical conductivity was measured using a conductivity probe (LF TetraCon 325, WTW; conductivity meter LF 330, WTW). Dissolved oxygen in water samples (CellOx 325, WTW; voltmeter Oxi 330, WTW) was measured after calibration against water-saturated air. The redox potential probe (Ag/AgCl with 3 M KCl In-Laboratory Redox Pro ORP, Mettler Toledo, Columbus, OH, USA; voltmeter pH323, WTW) was checked using a 475 mV standard solution (Hamilton Bonaduz, Bonaduz, Switzerland). In order to correct redox potential measurements to the standard hydrogen electrode (SHE) and calculate pe (logarithm of electron concentration), the measured value was first corrected for temperature using the conversion table provided by Hamilton, and then applied to the following equation (Nordstrom and Wilde 2005):

$$Eh_{\text{Corr.}} = Eh_{\text{Field}} + 224.4 – 0.7T \quad (1)$$

where $Eh_{Corr.}$ corresponds to the redox potential corrected to the SHE, Eh_{Field} is the temperature-corrected field measurement and T (°C) is the temperature. pe is calculated using the equation (Deutsch 1997)

$$pe = \frac{F}{2.303RT} Eh_{Corr} \quad (2)$$

where F is Faraday's constant and R is the universal gas constant.

Water and sediment samples were collected in triplicate. From the outflow site, because of access difficulties, a full suite of water samples were only collected on October 25, 2011. Samples were taken aseptically into sterile plastic 50-mL centrifuge tubes from the outflow, terrace and creek sites. Care was taken to avoid exposure to excess air, and tubes were capped underwater (for water samples) or filled to the top (sediment samples) before capping. Water and sediment samples were stored on ice packs for a few hours until storage at 4°C in the laboratory.

2.4.3. Water analytical methods

Immediately upon arrival to the laboratory on the sampling day, water samples were vacuum filtered through 0.45-µm cellulose acetate membranes (Sartorius AG, Göttingen, Germany) followed by 0.1-µm cellulose nitrate membranes (Whatman Ltd, Kent, UK). Water samples of each fraction were saved to give unfiltered, 0.1 to 0.45 µm and <0.1 µm fractions. These fractions were acidified with 7 N HCl or HNO_3 and stored at 4°C. The unfiltered fractions of some samples did not completely dissolve so they were filtered again through 0.2-µm cellulose acetate syringe filters; we do not expect the loss of a few non-iron particles to have a significant affect on our results. Metals and other elements of interest (Al, As, Ba, Ca, Cd, Ce, Co, Cr, Cs, Cu, Fe, K, Li, Mg, Mn, Mo, Na, Ni, Pb, Si, Sr, Ti, U, V and Zn) were analysed by inductively coupled plasma–mass spectrometry (ICP-MS) (X-Series II, ThermoFisher Scientific, Bremen, Germany) and inductively coupled plasma–optical emission spectrometry (ICP-OES) (725 ES, Varian Inc., Palo Alto, CA, USA) at the Institute of Geosciences at the Friedrich Schiller University Jena, Germany. A mixture of single-element standard solutions (Merck, Whitehouse Station, NJ, USA) was used for instrument calibration and the calibration curves were deemed acceptable if standard reference materials were within 10 % of the certified values.

Samples were run in triplicate, and the detection limit was calculated based on the following equation:

$$\text{Detection limit} = \frac{\text{dilution factor} \times 3 \times \sqrt{2\sigma_{\text{abs}}}}{S} \quad (3)$$

where σ_{abs} is the absolute standard deviation of the blank sample (water and acid) and S is the sensitivity (intensity, concentration). Sample carryover was prevented by using 'intelligent flushing,' where the flushing proceeds until the count rate is below a certain value.

Phenanthroline was used as a complexing agent for the spectrophotometric determination of Fe^{II} (modified from Tamura et al. (1974).) in water and sediment porewater at all sites in triplicate. In the field, water samples were collected in 50-mL plastic tubes, filtered through a 0.2-µm cellulose acetate syringe filter (Roth) and acidified with 7 M HCl. Sediment samples were centrifuged and the supernatant anoxically sampled in the laboratory a few hours after sampling, filtered through a 0.2-µm syringe filter and acidified. Following addition of acetate buffer and 1,10-phenanthrolinium chloride monohydrate, the absorbance was measured at a wavelength of 512 nm (Hach, Lange DR 3800). A linear Fe^{II} standard curve was prepared in 0.5 M HCl using $FeSO_4 \cdot 7H_2O$ at concentrations from 5 to 500 µM (R^2 >0.9997 for water analyses and >0.9935 for sediment analyses).

A reaction of barium chloride gelatin with the water samples was used to determine dissolved sulfate concentrations by means of a spectrophotometric method (Tabatabai 1974). In the field, samples were filtered through a 0.2-µm syringe filter (PDVF, Carl Roth) and acidified. A white $BaSO_4$ precipitate formed and the turbidity (absorbance) was measured at a wavelength of 420 nm. A linear standard calibration curve was prepared in ultrapure water using $MgSO_4 \cdot 7H_2O$ at concentrations from 50 to 1000 µM (R^2 > 0.9973).

2.4.4. Solid analytical methods

Sediments from October 25th were frozen upon return to the laboratory and freeze-dried under vacuum. After drying, samples were ground to a fine powder and analysed by X-ray diffraction (XRD, D8 Advance, Bruker AXS GmbH, Karlsruhe, Germany, $Cu_{K\alpha}$ source operated at 40 kV and 40 mA) from 5 to 70° at a step size of 0.02°, dwell time of 0.5 s per step, and with sample rotation at 30 rpm. Suspended particles in selected water samples were filtered through a 0.45-µm cellulose acetate membrane (Sartorius) and dried in air on the membrane. Dried material was placed on Si low-background plates for analysis by XRD (same parameters as for sediment samples).

For all sediment samples, wet/dry mass ratios were measured gravimetrically following drying (Kelvitron t, Heraeus Holding, Hanau, Germany) at 105 °C. Sediment density was determined gravimetrically for 1 mL of wet sediment in triplicate using a modified plastic syringe. Density and wet/dry ratios (Table A.3) were used in various constituent concentration calculations.

In order to have a better understanding of the mineral components of the sediment, particularly the distribution of iron between various fractions including poorly crystalline iron oxides and crystalline iron oxides, an established sequential extraction procedure was used (Caraballo et al. 2009; Caraballo et al. 2011; Dold et al. 2013). Sediments collected on July 18, 2011 from the terrace and creek sites were centrifuged and the pore water was removed in an anoxic chamber. Samples were then freeze-dried and thereafter stored in air. For the sequential extraction, a blank with ultrapure water only was treated in the same way as the samples throughout all extraction steps, which are explained in Table 2.1. The procedures for steps 1–4 and 6 were taken from Caraballo et al. with some minor changes (2009). Step 5 is part of the

standard BCR (European Union Community Bureau of Reference) procedure (Rauret et al. 1999; Macías et al. 2012). Sequential extraction procedures may have some inherent issues that require careful interpretation of the data. In this regard, extraction times and the ratios of solvent to sediment were tested for similar (poorly crystalline Fe and Al oxide) sediments from AMD remediation sites by Caraballo et al. (2009). Extractions of both terrace and creek sediment samples were performed in triplicate. For the elements reported in this study, except Na, the standard deviations were less than 10% for at least 50% of the extraction steps across both terrace and creek samples. For specifics, see the error bars in Figure 2.5 and standard deviation values in Table A.4 in Appendix A. Fe recoveries (Equation 4) are 81–83%, which is acceptable considering that a small amount of material was lost during the supernatant removal steps.

Table 2.1. Sequential extraction procedure

Sequential extraction step	Expected dissolved phases
1) Water soluble fraction: 100-mg sample + 20-mL ultrapure water, shaken for 14.5 h at room temperature (RT)	Secondary sulfates and other salts
2) Sorbed and exchangeable fraction: 20 mL of 1 M NH_4-acetate (pH 4.5 buffer), shaken 1–1.25 h at RT	Calcite, sorbed and exchangeable ions
3) Poorly ordered Fe^{III} oxyhydroxides and oxyhydroxysulfates: 20 mL of 0.2 M NH_4-oxalate (pH 3 buffer), shaken for 30 min in darkness	Mainly 2-line ferrihydrite and schwertmannite
4) Highly ordered Fe^{III} hydroxides and oxides: 20 mL of 0.2 M NH_4-oxalate (pH 3 buffer), ~80 °C water bath for 1 h	Goethite, jarosite, 6-line ferrihydrite and hematite
5) Oxidizable phases including organics and sulfides: 10 mL of conc. H_2O_2 was added for 1 h at RT, covered in ~85 °C water bath for 1 h, uncovered and evaporated down to <3 mL. Repeated.	Organic matter, metal sulfides
6) Pseudo-digestion residue: aqua regia (3 : 1 conc. HCl/HNO_3) uncovered for 17–19 h, and then 80–95 °C to dryness.	Residue other than silicates

The sediment samples were also analysed by XRD after the selective mineral dissolution (third step of the sequential extraction design to dissolved poorly ordered Fe^{III} oxyhydroxides and oxyhydroxysulfates) and compared with the starting (original) diffraction pattern. The

Rigaku MiniFlexII XRD instrument (Rigaku Americas, The Woodlands, TX, USA) was operated under the following conditions: $Cu_{K\alpha}$ source at 30 kV and 15 mA, 0.3° per step and 3 s per step, from 10° to 70° 2θ with sample rotation. Samples were applied with ethanol onto low-background silica plates for analysis.

Sediment samples from all sequential extraction steps, including pseudo-total and total digests, were analysed by ICP-MS (X-Series, Thermo Electron, Waltham, MA, USA) per Standard Method 3125-B (APHA et al. 1998). Elemental concentrations below the minimum reporting level (MRL, EPA Method 218.7, listed in Table A.2) (Zaffiro et al. 2011) for each element were set to zero for further calculations, although it is possible that elements at concentrations below that level were present. The blank sample was subtracted from all samples for each matching fractionation step. As an internal check for percentage recovery of each element, the following calculation was performed (Macías et al. 2012):

$$\text{Recovery (\%)} = \frac{\text{Step 1} + \text{Step 2} + \text{Step 3} + \text{Step 4} + \text{Step 5} + \text{Step 6}}{\text{Pseudo-total dgestion}} \times 100 \qquad (4)$$

The major elements had recoveries of 80 to 120 %.

2.4.5. Electron microscopy

Preparation methods were carefully chosen in order to analyse mineral nanoparticles in water and sediment samples by electron microscopy. In all cases where there was a liquid sample (water samples and re-suspended sediment samples), TEM grids (lacey carbon on 400 mesh gold, Electron Microscopy Sciences) were prepared by pipetting a 7-µL drop onto the grid and wicking away gently from underneath with a lint-free wipe or glass fibre filter, and then rinsing with ultrapure water two times to remove salts using the same drop and wick method. Grids were prepared in the field as well as on the same day in the laboratory and after all other processing

steps in order to make sure that the aging process of the refrigerated samples over time was well understood (Figure A1). In addition, in an attempt to look at microbe–mineral associations by TEM, traditional methods were modified to fix bacteria in water samples (Dykstra 1993; Glauert and Lewis 1998). Sediment and outflow water sample grids were stored in a N_2-purged plastic storage container (Sample Saver, South Bay Technology Inc, San Clemente, CA, USA) to limit contact with air and prevent oxidation during long-term storage.

Scanning electron microscopy (SEM, Ultra-Plus SEM with field emission gun (FEG), ZEISS, Oberkochen, German, or Quanta 600 FEG SEM, FEI, Hillsboro, OR, USA) was first used to survey the TEM grids to note approximate particle size, morphology and elemental composition. TEM instruments used for further structural and elemental characterisation included a Philips EM 420 (120 kV, Philips, Eindhoven, the Netherlands), FEI Tecnai G^2 (200 kV, FEI, Eindhoven, the Netherlands) and multiple FEI Titans (300 kV, FEI, Eindhoven, the Netherlands). Fast Fourier transform (FFT) patterns calculated from HR-TEM images and selected area electron diffraction (SAED) patterns were analysed with the programs *ImageJ* (NIH – National Institutes of Health, Bethesda, MD, USA) and *Digital Micrograph* (Gatan Inc., Pleasanton, CA, USA). *TEM Imaging and Analysis* (TIA, FEI, Hillsboro, OR, USA) software was used to semiquantitatively analyse the energy-dispersive X-ray spectroscopy (EDS) spectra.

2.5. Results and discussion

2.5.1. Geochemistry and composition of mine drainage water

The Gessen Creek receives highly polluted, slightly acidic water from a neutralised underground mine, as well as groundwater from underneath the nearby former waste heap piles in the mining area. The physicochemical parameters as well as the water chemistry observed in

the two sampling campaigns (July and October 2011) were fairly similar; therefore, for the sake of simplicity, the hydrochemical behaviour of the system will be summarised using mainly one sampling campaign (October 2011). The pH varies from slightly acidic (pH 5.75 at the outflow site) to almost neutral (pH of 6.34) as it flows over the creek bank (terraces) and stays approximately constant at 6.10 after mixing with creek water (Figure 2.2). The redox potential (pe) clearly reflects the conditions of a reducing underground environment (outflow pe of 4.4) slightly evolving to a more oxidizing environment (creek pe of 5.2). In agreement with this, dissolved oxygen (DO) also marks a transition from an almost anoxic underground environment (outflow DO of 0.6 mg L^{-1}) to an open-air system (creek DO of 5.0 mg L^{-1}) with an expected DO maximum at the cascades (terraces DO of 8.5 mg L^{-1}) attributable to turbulence and agitation of the water (Figure 2.2). Dissolved–nanoparticulate iron concentrations (defined by the <0.1-μm filter fraction) entirely correspond to ferrous iron as determined spectrophotometrically (Table A.1). We don't expect any significant ferrous iron contribution from Fe^{II}-bearing minerals that passed through the filter membrane, because they were typically much larger than 100 nm in at least two dimensions as we show later by TEM. Contact with air leads to rapid oxidation of Fe^{II} to Fe^{III} in near-neutral mine drainages (Bigham and Nordstrom 2000), and the subsequent precipitation of Fe^{III} mineral phases (e.g. ferrihydrite or goethite). Despite this known rapid oxidation, there is still a reasonably high concentration of dissolved Fe^{II} in the sediment porewater (Table A.3). Sulfate concentrations in the dissolved–nanoparticulate fraction are not statistically different as the water flows from the outflow site to the terrace and creek sites, possibly indicating that there is not a significant amount of sulfate that is precipitating out with the iron. This hypothesis will be tested in the mineralogical study of the particulate matter and

sediment performed in the next section. A more detailed description of the water composition is offered in Appendix A (Table A.1).

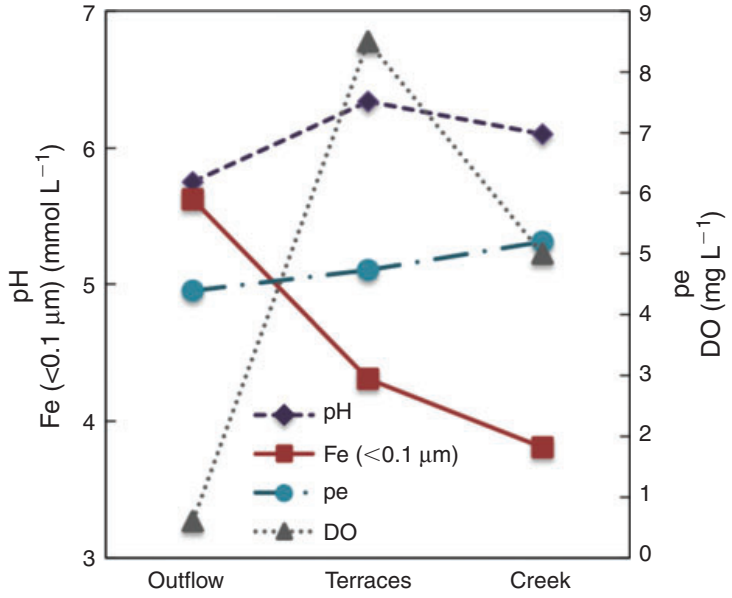

Figure 2.2. pH, pe, dissolved oxygen (DO) and dissolved–nanoparticulate Fe concentration in water at the three sampling sites. The terrace site is 20 m downstream from the outflow site, and the creek site is 2-m downstream from the terrace site. Sampling date: 25 October 2011.

In order to obtain a better idea of the transport of contaminants in the Gessen Creek, the partitioning of elements between the particle-associated (unfiltered minus 0.1-µm filtered waters) and the dissolved–nanoparticulate (0.1-µm filtered waters) fractions were studied (Figure 2.3). Iron is the dominant metallic constituent in this system, being the primary source of suspended particulates as well as the main metallic component of the dissolved–nanoparticulate fraction. Iron in the dissolved–nanoparticulate fraction shows a decreasing trend (from the outflow to the creek) for both sampling dates, supporting the idea of Fe^{II} oxidation followed by the rapid precipitation and settling of Fe^{III} mineral phases. As shown, total iron concentrations in July are higher at the terraces than the outflow, likely because the water sample is reflecting the effect of re-suspended iron particles because of the turbulent regime of these waters. Silicon, manganese

and aluminium (in that order) are the other major components, whereas nickel, zinc and cobalt are also significant, and copper, uranium and arsenic appear in trace concentrations. It is important to notice that 21–33 % of the silicon in the water is associated with suspended particles, and follows a similar trend for iron, whereas aluminium is almost entirely particle-associated. Co-precipitation with various iron oxides is likely, especially for Si (Hochella et al. 1999; Cismasu et al. 2011; French et al. 2012), as shown by TEM in Figure 2.6 and Figure 2.7. Aluminium can be incorporated into iron oxides (Cismasu et al. 2011), but can also take the form of hydrobasaluminite. Clay minerals have not been found by XRD nor TEM, and are likely not a major source of Al and Si in suspended particulates.

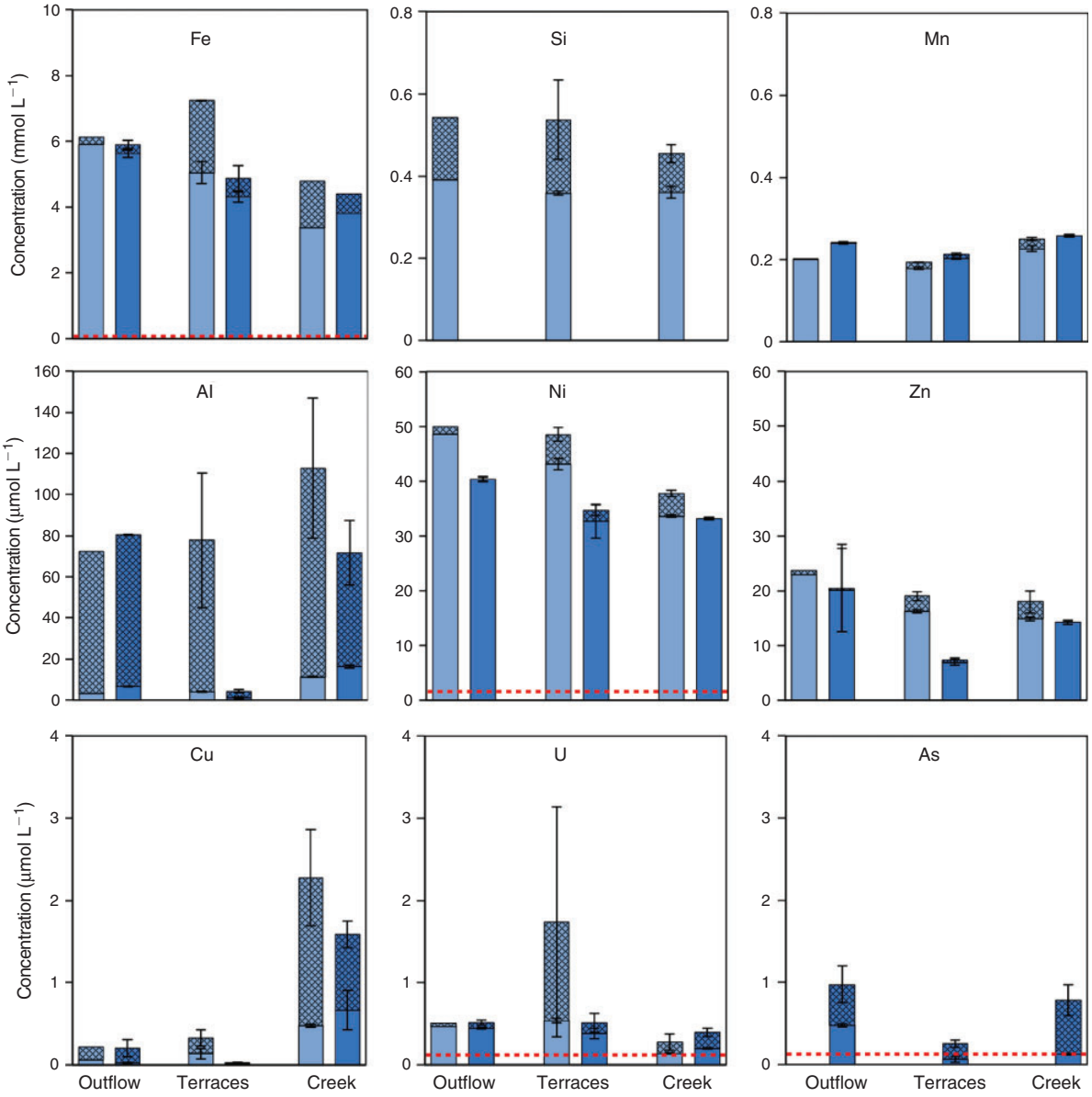

Figure 2.3. Major, minor and trace elements in water samples from 18 July (light blue) and 25 October 2011 (darker blue). Bars represent the total concentration in the water (unfiltered water samples). Each bar has been divided in two regions corresponding to: (a) the effect of particulate matter (> 0.1 μm) in water (obtained by subtracting the elemental concentration of the 0.1-μm filtered samples of the concentration of the unfiltered samples, and marked with a cross-hatch pattern) and (b) the < 0.1 μm m fraction, which includes dissolved species and nanoparticles (represented by the unmarked section of the column). Red dashed line corresponds to the World Health Organization maximum contaminant level (2011).

The metal contaminants of highest concentration in the water (Ni and Zn) are in the dissolved–nanoparticulate fraction, and only a small portion is associated with particulates. At

the terrace and creek sites, Cu is primarily associated with the particulate fraction as well. The elements with the lowest total concentrations in the water (Cu, U, Cr, As and Pb) are commonly associated with iron oxides in slightly acidic pH environments (Lee et al. 2002), and thus could have already been sequestered in the subsurface. Nickel tends to sorb to iron oxides at higher pHs (Arai 2008), although the specifics of metal sorption are highly dependent on ionic strength, sorbent mineralogy and size, and presence of passivating or competing species.

A significant dilution effect in the waters moving from the terraces to the creek can be ruled out based on the small (10 %) decrease observed for Na, a conservative element in these types of environments (Table A.2). Furthermore, some elements (Mn, Al, Co, Cu and As) show a higher concentration in the creek than along the terraces. These results are characteristics of several water sources (including Figure A.2a). As observed in the field, the sources for the creek site, other than a large area of water flowing over the terraces, include groundwater infiltrating through the creek bottom and drainage pipes collecting the outflowing water from other former waste rock piles nearby.

For the metal(loids) that are regulated by the World Health Organization's health-based drinking water guidelines, Al, Mn, Ni, U, As and Cd exceed their limits (World Health Organization 2011), whereas Cu, Cr, Pb, and Zn do not (Figure 2.3). See Table A.2 in Appendix A for a complete list of element concentrations.

2.5.2. Mineralogical and chemical composition of sediments

The terrace sediments are in the form of a hard crust that varies in colour from orange-brown to reddish-brown with softer, more orange material underneath. The opposite is observed for the creek sediments, which are lighter on the crust and more reddish-brown below a

centimetre deep. Creek sediments are also looser and finer than terrace sediments. Some field pictures are offered in Appendix A (Figure A.2).

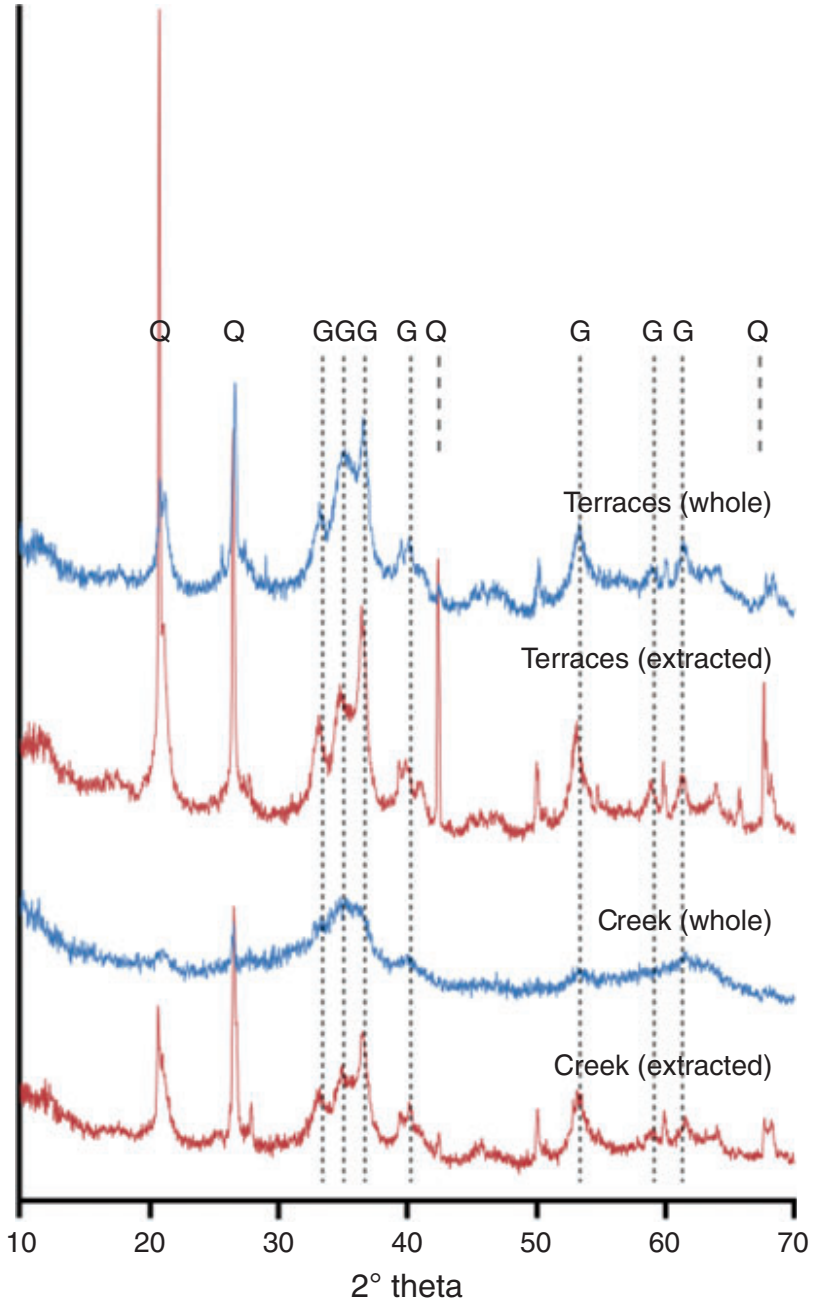

Figure 2.4. X-Ray diffraction spectra of terrace and creek sediments before and after the selective dissolution of the poorly crystalline iron mineral phases. G, main goethite peaks; Q, main quartz peaks. *y*-axis is the relative intensity.

As shown by XRD, the terrace sediments are mainly comprised by goethite, an iron(III) oxyhydroxide (Figure 2.4 and Table 2.2). The diffraction patterns for the creek sediment have much broader and difficult-to-resolve peaks; however, as a first approximation, it can be inferred that diffraction peaks from goethite are more difficult to observe because of the diffraction maxima of several other very poorly crystalline mineral phases. In general, if all of the main goethite peaks are present, it is clear that goethite is present. This complex diffraction pattern has been frequently reported for AMD systems (Bigham and Nordstrom 2000; Caraballo et al. 2009). Ferrihydrite (2-line and 6-line) and schwertmannite all have very broad peaks (especially in the range 32°–38° 2Θ), and have commonly been reported as constituents of these multiphase iron sediments. The terraces are similar to iron stromatolites, frequently seen in other metal-polluted creeks, which are mainly comprised of different layers of aged minerals like goethite, or jarosite in lesser amounts, as well as other detrital minerals (e.g. quartz) and poorly crystalline iron minerals (e.g. ferrihydrite or schwertmannite); in contrast, loose and fresh poorly crystalline iron minerals typically form the creek bed (Sanchez-Espana et al. 2007; Caraballo et al. 2011; Perez-Lopez et al. 2011). This same pattern is observed in Gessen Creek with goethite and an as-yet undetermined poorly crystalline iron mineral phase as the main constituents of the sediment (Figure 2.4).

Table 2.2. Comparison of d-spacings (Å) between those measured by X-ray diffraction (XRD) and fast Fourier transform (FFT) in the sediments and likely iron oxyhydroxide mineral phases

XRD of samples taken on October 25, 2011. FFT of high resolution transmission electron microscopy (HR-TEM) areas on aggregates shown in Figure 2.6. Ranges listed are not accounting for broad ring widths, they are ranges of d-spacings across five different HR-TEM areas. Goethite (synth.) data are from International Centre for Diffraction Data (ICDD) Powder Diffraction File (PDF) card #01-081-0462 (Hazemann et al. 1991), goethite and '6-line' ferrihydrite data are from Bigham and Nordstrom (2000).

Site	XRD	FFT	Goethite (synth.)	Goethite	'6-line' Ferrihydrite
Terraces	7.39				
	5.19	4.98	5.11	4.91	
		4.75–4.77			
	4.19		4.19	4.18	
	3.36		3.39	3.37	
	3.28				
		2.90–2.94			
	2.70			2.69	
		2.58–2.62	2.58	2.58	
	2.54	2.51–2.54	2.53		2.54
	2.45	2.43–2.46	2.45	2.45	
		2.37–2.38	2.31		
	2.24	2.20–2.23	2.19	2.25	2.24
	1.94	2.09–2.15	2.10	1.91	1.97
	1.72	1.72	1.72	1.72	1.71
	1.63	1.65	1.66		
	1.57	1.60	1.61	1.56	
	1.51		1.51	1.51	1.51
	1.46		1.45		1.46
Creek	7.67				
		4.64			
	4.22	4.18	4.19	4.18	
	3.36		3.39	3.37	
		2.94			
		2.88			
		2.82			
	2.68	2.64	2.70	2.69	
	2.55		2.53	2.58	2.54
			2.49		
	2.45	2.47	2.45	2.45	
		2.42			
		2.37			
	2.25	2.23	2.26	2.25	2.24
		2.07	2.10		
		1.97	2.01	1.91	1.97
		1.80–1.84	1.83		
	1.71	1.68–1.74	1.69	1.72	1.71
		1.58–1.61	1.61		
	1.50		1.51	1.51	1.51
	1.46	1.40–1.43	1.42, 1.45		1.46

To obtain a better understanding of the poorly crystalline phases, as well as how the different metal(loids) are distributed among the different mineral phases in the sediments (what mineral hosts them and how mobile they are), the solid samples were submitted to a sequential extraction procedure specifically designed for iron rich sediments (Caraballo et al. 2009; Dold et al. 2013). By visually comparing the diffraction patterns before and after the selective dissolution of the poorly crystalline Fe mineral phases (Figure 2.4), it is clear that the creek sediments are composed of a significant amount of that poorly crystalline material in addition to goethite. In contrast, the difference between the terrace sediment diffraction patterns before and after the selective dissolution is hardly noticeable and therefore confirms that poorly crystalline iron oxides are a lesser component.

The Fe/S molar ratio is typically used as an additional parameter to discern between schwertmannite and ferrihydrite. Using Fe and S concentrations from the third step of the sequential extraction (Figure 2.5 and Table A.4), Fe/S molar ratios of 21.2 and 4.3 were obtained for the terrace and creek sediments, respectively. The Fe/S molar ratio of schwertmannite typically ranges from 4 to 8 (Bigham and Nordstrom 2000), although a recent study compiling data for almost 50 natural pure schwertmannite samples over the last 15 years has shown how schwertmannite Fe/S molar ratios (although exhibiting a higher sample population region between 4 and 6), can span values from 3.77 to 15.53 (Caraballo et al. 2013). The sequential extraction results seem to line up with the idea of ferrihydrite being the main poorly crystalline iron mineral phase in the terrace sediments, whereas schwertmannite would be the one for the creek sediments. However, data from the sequential extraction and XRD are not enough to completely understand the mineralogy of the system, as shown in the discussion of the TEM results in the following section.

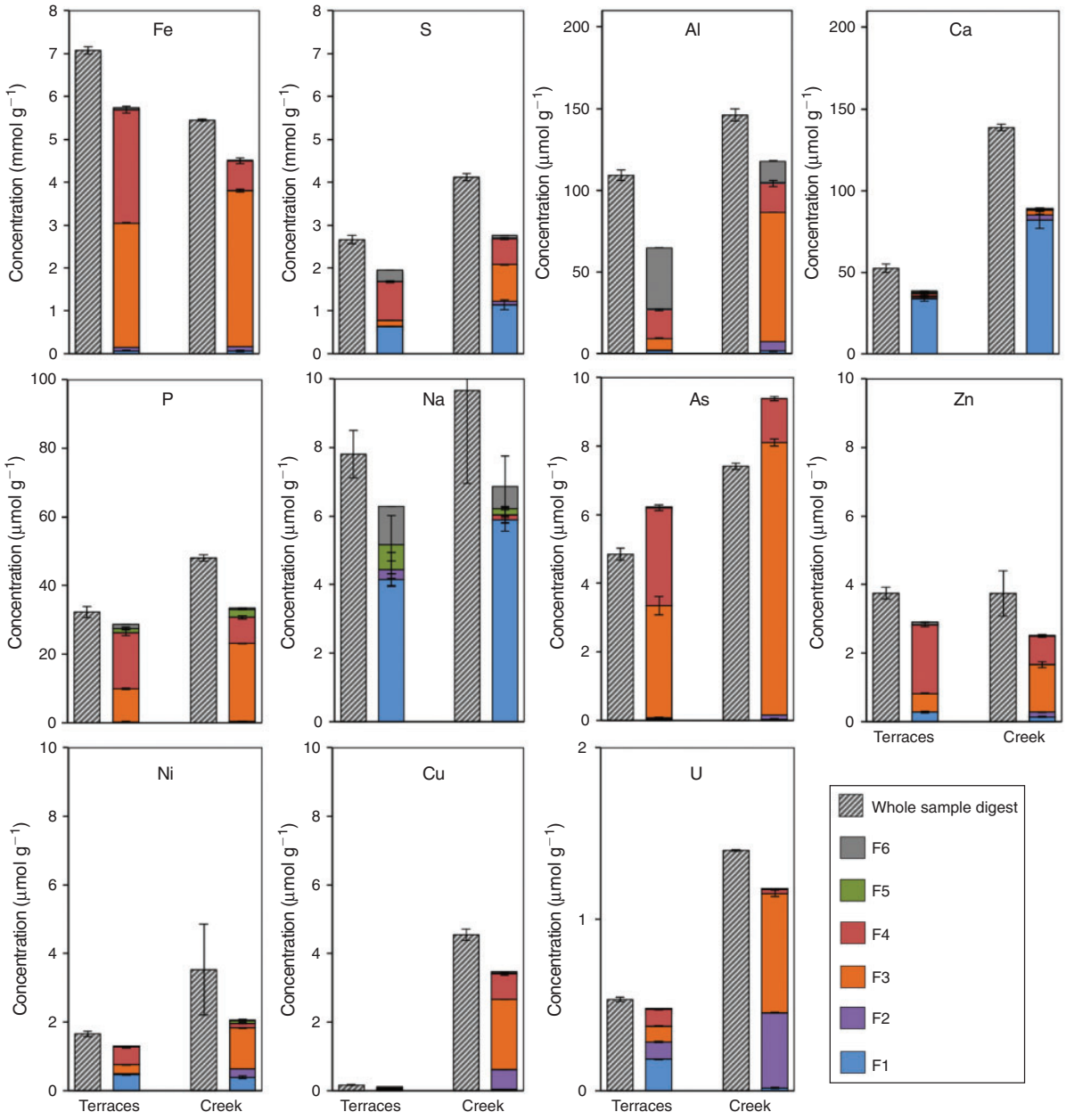

Figure 2.5. Results from the sequential extraction of the terrace and creek sediments. Error bars are based on sample triplicates. Theoretical fractions are as follows: F1, water soluble; F2, sorbed and exchangeable; F3, poorly ordered Fe^{III} oxyhydroxides and oxyhydroxysulfates; F4, highly ordered Fe^{III} oxides and hydroxides; F5, oxidizable phases including organics and sulfides; F6, pseudo-digest residue. 'Whole sample digest' is an aqua regia digest of the non-selectively fractioned samples.

Another useful piece of information obtained from the sequential extraction is the amount of Fe corresponding to schwertmannite–ferrihydrite (fraction 3) or to goethite (fraction 4). As

shown in Figure 2.4, the Fe content is almost equally distributed between the 3rd and 4th fractions for the terrace sediments, whereas Fe from the creek sediment is mainly hosted in the poorly crystalline Fe minerals (fraction 3).

Sulfur is, besides iron, the most important component of the terrace and creek sediments (Figure 2.4). Because of the lack of any sulfur in the oxidisable fraction of the sequential extraction (fraction 5, specifically selected to target organic material and sulfides), as well as the hydrochemistry of the waters generating these precipitates, it is reasonable to assume that sulfur in the sediments will be predominantly in the form of sulfate. As shown in Figure 2.5, a significant amount of this sulfate is water-soluble (fraction 1) forming sulfate salts with other elements (mainly with Ca, in the form of gypsum, but also Na, Ni, Si, Zn and U). Sulfur released during the 4th step of the sequential extraction is likely associated with goethite.

The remaining elements analysed (Al, As, Cu, Ni, P, U and Zn) are primarily released during the third and fourth steps of the sequential extraction, showing a clear dependence on schwertmannite–ferrihydrite and goethite selective dissolution (Figure 2.5). These particular metal(loid)–iron oxide associations are quite common in slightly acidic and circum-neutral mine drainage systems (Hochella et al. 1999; Genovese and Mellini 2007; Heikkinen and Räisänen 2009) and are predicted by laboratory experiments and modelling (Dyer et al. 2004), although the extent and type of association is quite variable. The transformation of ferrihydrite to goethite at pH 6 has been shown to increase the extent of nickel sorption (and likely structural incorporation) (Ford et al. 1997). Although the presence of Cu in the terrace sediments is negligible, a noticeable amount is observed in the creek sediment (Figure 2.5). This uneven distribution can be explained by the very low Cu concentration in the outflow and terrace waters, whereas the creek waters (and especially the suspended particles) showed a much higher Cu

concentration. It is also important to notice how an important proportion of the recovered Ni and U are obtained in the first and second steps of the sequential extraction, showing a higher mobility and availability for these two elements. The results from these sequential extractions prove to be a valuable complementary technique to TEM analysis of the sediment particles, by which no metals were detected by EDS presumably because of a detection limit of ~0.1 atomic percent.

2.5.3. Characterization of colloids and nanoparticles suspended in water

XRD of suspended particulates from water samples at the terrace and creek sites shows weak, broad peaks that match the broad peaks from the creek sediment, as well as sharp quartz peaks (Figure A.3). The general location of the broad peaks match the major peaks of the iron oxide (ferrihydrite and goethite) sediments, possibly indicating the presence of amorphous iron oxides. Obvious secondary precipitates, such as salts, are not identifiable here, and are not observed by TEM. As a result of the minimal amount of material on the filters, the poorly crystalline nature of these solids, and the preparation in air, TEM provides a much more accurate picture of the mineral phases suspended in the Gessen Creek water.

The anoxic and slightly reducing mine-water effluent from the outflow site has suspended particles that are primarily pseudo-hexagonal platelets of Zn-bearing green rust (Figure 2.6a). Although some studies have described green rust in reduced soils (Feder et al. 2005; Rennert et al. 2012; Trolard and Bourrié 2012) and sediments (Wankel et al. 2012), this paper is one of very few to report the presence of a member of the green rust mineral family in natural waters (Christiansen et al. 2009; Zegeye et al. 2012). The mine effluent shows an abundance of flat platelets with rounded corners (circle in Figure 2.6a). The rounded corners could be attributed to an incipient stage of dissolution. Others are pseudo-hexagons with straight edges and sharp

corners. These morphologies are similar to those found in groundwater by Christiansen et al. (2009). Measurements of the platelets aligned perpendicular to the grid surface show that they are ~10–20 nm in thickness, which matches a reported thickness of sulfate green rust measured using AFM (Skovbjerg 2005). Although many of the green rust particles have diameters of up to a micrometer, they can still be mobile through the subsurface by micrometer or larger sized channels. This situation is likely a result of the high rate of water flow and soil removal at the outflow site. In this study, the presence of green rust particles in the water samples was not observed by XRD because the samples likely oxidised during sample preparation and storage in air.

Both SAED (Figure 2.6a) of multiple particles and FFT patterns (Figure 2.6c) of HR-TEM images show the crystalline nature of these platelets, with two main crystal lattice plane *d*-spacings of 2.47 and 1.44 Å, giving a *d*-spacing ratio of 0.58. This compares most closely to green rust II ($Fe_2(OH,SO_4)_{4.88}$, Powder Diffraction File (PDF) card #00-041-0014) (Vins et al. 1987) *d*-spacings of 2.48 and 1.46 Å, and also to the *d*-spacing at 2.48 Å of sulfate green rust (PDF card #00-013-0090) (Bernal et al. 1959). The *d*-spacing ratio of 0.58 from Figure 2.6c is representative of at least seven platelets and one aggregate (Figure 2.6a) in the outflow sample analysed by SAED or FFT, and they are comparable to SAED patterns of sulfate green rust in the literature (Ahmed et al. 2010; Pantke et al. 2012) when specific *d*-spacings are not reported. It is important to note that ferrihydrite, goethite and hematite also have similar *d*-spacings and *d*-spacing ratios, although the geochemical conditions in the outflow water are not favourable for the formation or persistence of these iron(III) minerals. The unique particle morphology and FFT/SAED patterns support the generic characterisation of these platelets as green rusts (although the specific type of green rust cannot be assigned at this point).

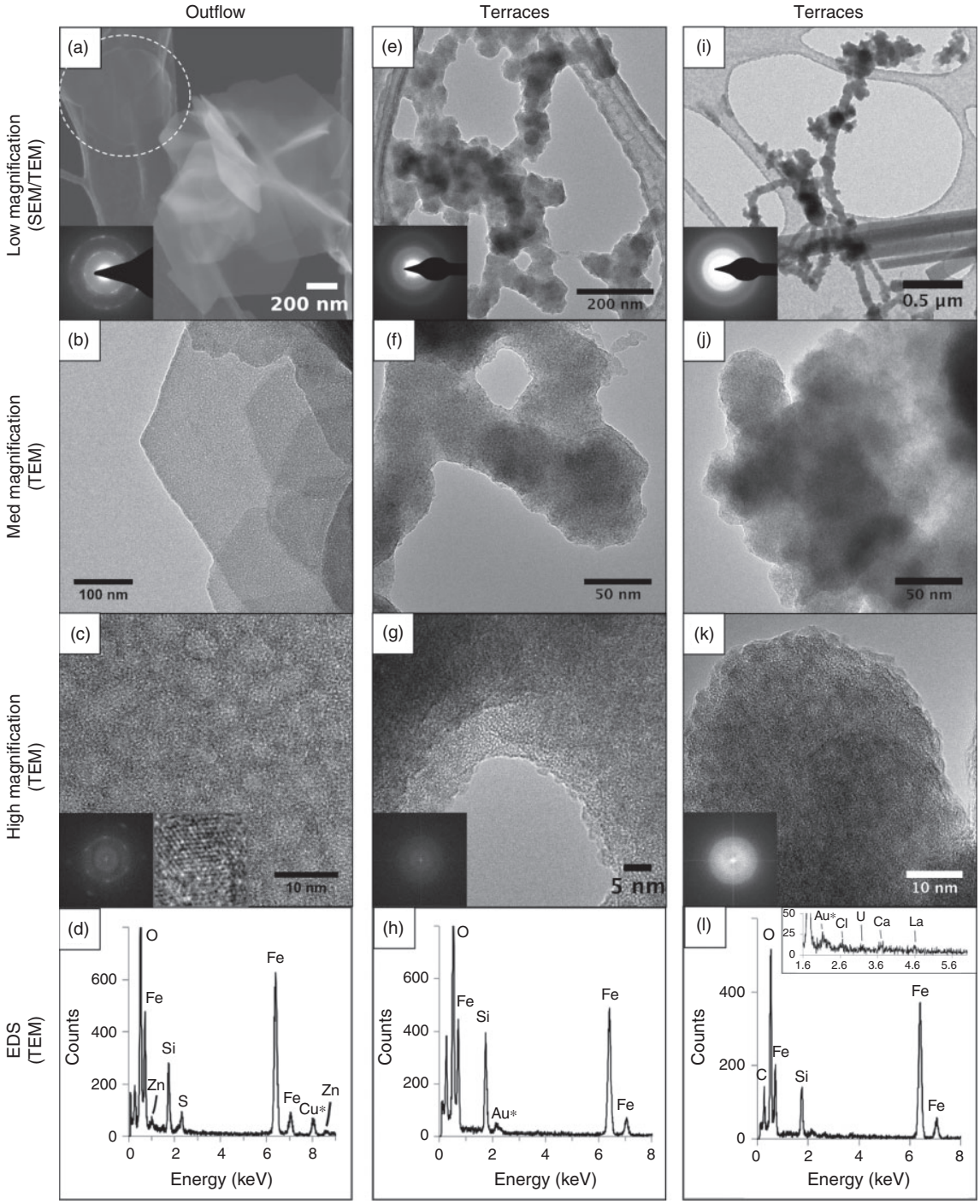

Figure 2.6. Representative examples of the suspended particles found in the outflow and terrace water samples. Creek suspended particles are not shown due to their similarity (and no additional information) when compared with particles at the terrace site. Each column includes the same area with different views: low magnification scanning electron microscopy (SEM) (a) or transmission electron microscopy (TEM) (e and i), medium magnification TEM (b, f and j), high-resolution TEM (c, g and k) and TEM energy-dispersive X-ray spectroscopy (EDS) (d, h and i). Insets are selected area electron diffraction (a, e, i) or fast Fourier transform (c, g, k) patterns from which d-spacings can be calculated. In the EDS spectra, Au peaks come from the TEM grid mesh and the Cu peak in (d) comes from the TEM grid holder. The darker areas in (c) are nanocrystalline and their lattice fringes are visible when the image is enlarged. The circle in (a) indicates a green rust nanosheet with rounded edges, likely due to dissolution.

Elemental analysis (TEM EDS) of the green rust platelets (Figure 2.6d) shows that Fe, O and Si are the major elements, where the Si is likely occurring as patches of amorphous silica co-precipitated with the green rust crystallites. Sulfur appears to be a minor component, showing a (semi-quantitative EDS) Fe/S ratio of 9:1. This ratio is larger than for ideal sulfate green rust II ($Fe^{2+}_4Fe^{3+}_2(OH)_{12}SO_4 \cdot 8H_2O$) (Simon et al. 2003). The formulae for different green rusts are continuously re-evaluated and modified, as shown by Mills et al. (2012) who recently recommended the re-definition of the mineral fougerite from its previously accepted formula of $(Fe^{2+},Mg)_6Fe^{3+}_2(OH)_{18} \cdot 4H_2O$ to a new formula that includes interlayer carbonate ions: $Fe_4^{2+}Fe_2^{3+}(OH)_{12}[CO_3] \cdot 3H_2O$. It may not be unreasonable to assume that naturally occurring green rusts could have a variety of anions in their interlayer. The green rusts found in the mine outflow in this study could include some interlayer sulfate, or simply carbonate and hydroxide, which we cannot quantify by TEM EDS.

A few areas containing many green rust platelets were analysed by TEM EDS (including those in Figure 2.6a) and a trace Zn signal was consistently found in all of them. Finding Zn associated with the green rust platelets (typically >0.1μm) is unexpected, considering that only a small portion of the Zn in the outflow water is associated with the particulate fraction (Figure 2.3). Zinc incorporation into synthetic sulfate green rust structures has been previously described (Ahmed et al. 2008) as well as proposed during the passive treatment of acid mine drainage (Caraballo et al. 2011). This is the first time that Zn-containing green rust has been reported forming part of the particulate fraction in surface waters. These observations are a clear example of the importance that mineral nanoparticles can have as transporters for metal pollutants in subsurface waters.

As a result of rapid oxidation, by the time the slightly acidic outflow water reaches the terrace and creek sites, the composition and morphology of the suspended particles change drastically. The majority of the suspended particles are tightly aggregated iron-rich spheroids co-precipitated with amorphous silica (see Figure 2.6e, i). The primary particles are relatively smooth (some have a bumpy texture) and are approximately 20–200 nm in diameter, which is fairly consistent across all sites from water samples prepared in the field and in the laboratory on the same day. SAED does not indicate crystallinity. However, with so many primary particles being relatively thick and electron dense, SAED might not be effective at finding nanocrystalline areas; HR-TEM is limited to examining just the edges of particles in these cases. Suspended particles in the water at the terrace and creek sites show a strong resemblance; therefore (for the sake of simplicity) the discussion has been limited to the creek sample.

Elemental analysis (TEM EDS) of multiple particles in an aggregate consistently shows Fe, O and Si as the dominant components with occasional traces of P, Al or alkali cations. In Figure 2.6i, typical spheroids seem to be clumped onto a more continuous nanowire structure of the same basic composition – Fe, Si, O. This particular area is highlighted here because traces of uranium and cesium were found in the area shown in Figure 2.6j, and is the only area of particles in terrace and creek water that we have found trace heavy metals. The bulk concentration of metals associated with suspended particles is likely too low to detect trace elements, and TEM EDS requires at least 0.1 atomic percent in order measure the signal.

2.5.4. Characterization of colloids and nanoparticles in sediment

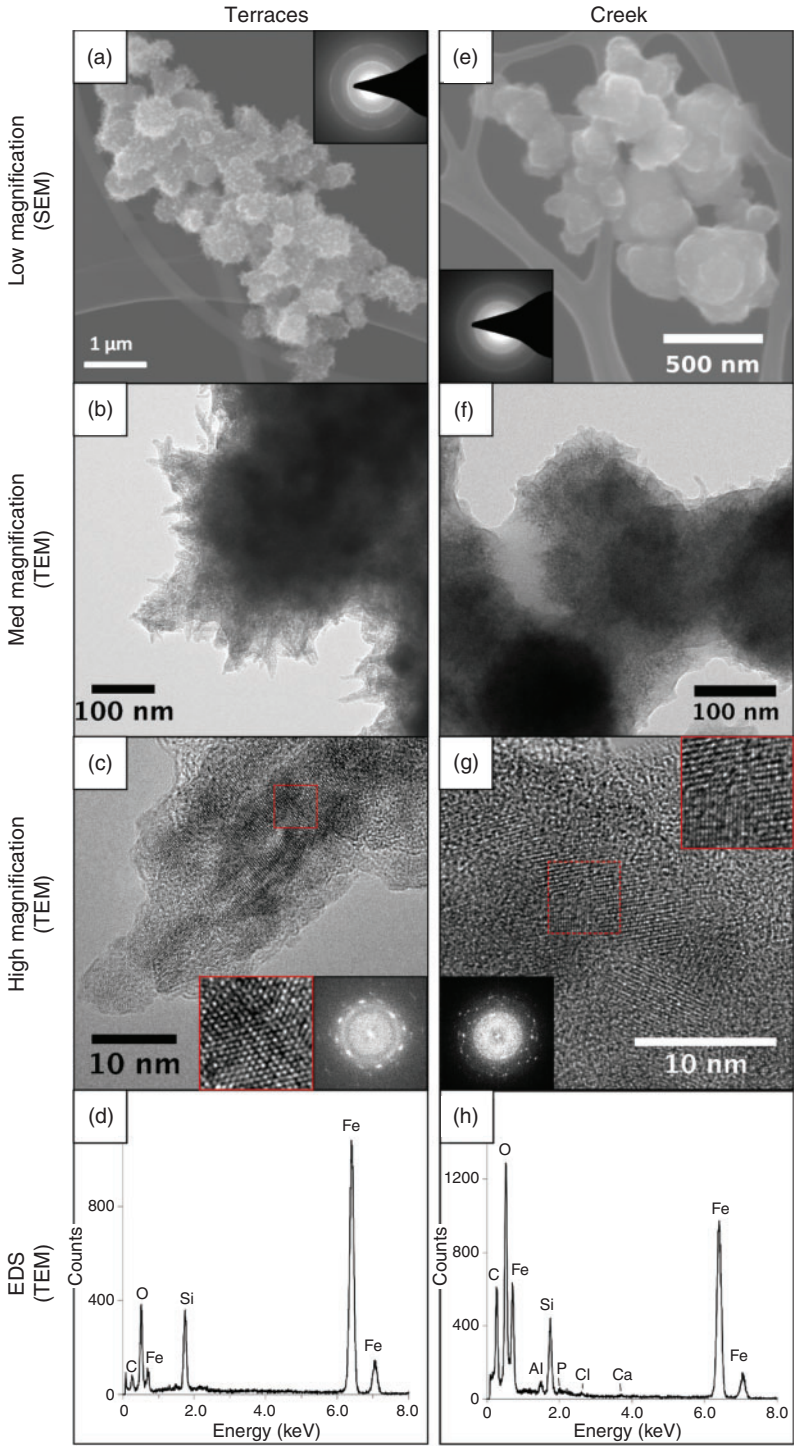

Figure 2.7. Selected representative examples of the typical particles found in the sediments at the terrace and creek sites. The samples were fixed with glutaraldehyde before transmission electron microscopy grid preparation. Insets are selected area electron diffraction patterns from smaller areas of the aggregate (a, e) and fast Fourier transform patterns calculated from the entire respective image (c, g).

Iron oxide particles in the sediment exhibit different morphological characteristics compared with those suspended in the water. The primary rounded particles of the aggregates tend to be larger (~100–1000 nm in diameter) than suspended ones (~20–200 nm in diameter). In addition to this distinct difference in size, spikes or needles are readily growing out of the spheroids in the terrace sediments (Figure 2.7a-c) that somewhat resemble the typical 'pincushion morphology' of schwertmannite. Creek sediments do not typically have needles that are as long (Figure 2.7g) as the terrace sample. Other than at the first couple of tens of nanometers from the edge, the particles are too thick to image the lattice fringes and thus it is very difficult to determine the structure of the core.

The crystalline domains of these sediment particles, often only a few nanometres in size, are not always straightforward to identify. A comparison of the *d*-spacings measured by FFT (Figure 2.7) and XRD (Figure 2.4) in the terrace and creek sediments and a selected list of *d*-spacings for goethite and 6-line ferrihydrite are shown in Table 2.2. The main *d*-spacings from 2-line ferrihydrite, 6-line ferrihydrite, schwertmannite and goethite are approximately the same (2.54 and 1.51 Å) (Bigham and Nordstrom 2000), but the number and sharpness of peaks in their XRD patterns increases in this order as the degree of crystallinity increases. Schwertmannite can be ruled out for the aggregates similar to those in Figure 2.7 because there is no sulfur. At least for the sediment particles shown in this paper, the nanocrystalline areas observed by HR-TEM at the edges and in the needles that form are primarily ferrihydrite transitioning to goethite, although some more crystalline areas of goethite do exist (data not shown). This transition of nanocrystalline domains from a poorly crystalline to a more crystalline phase (goethite) has also been observed for natural samples of schwertmannite (French et al. 2012).

TEM-EDS of areas encompassing portions of sediment particle aggregates show that they have a similar composition to the suspended particles – primarily Fe, O and Si. In addition, small amounts of P, Cl and Ca were sometimes detected. Bulk analyses of sediment show that P is primarily associated with iron oxide fractions, although Ca was not and Cl was below the minimum reporting level (Figure 2.5). We did not find any contaminant metals associated with terrace and creek sediment particles by TEM EDS. Again, trace elements at concentrations of less than 0.1 atomic percent are difficult to detect.

2.6. Summary, overall assessment and implications

Detailed studies of iron oxide nanoparticle and colloidal behaviour should be of particular interest to scientists studying contaminant transport and remediation, element cycling by microbes, fate and transport of engineered metal oxide nanoparticles in the environment and those trying to bridge laboratory experiments with the natural environment. The current study of slightly acidic mine drainage outflow has shown that analysing environmental constituents on the nanoscale in addition to the traditional bulk scale is critical for a more complete understanding of complex metal polluted systems. Proper sample preparation and storage is also critical in order to capture phases that are unstable in air (e.g. Zn-bearing green rust). The multi-scale analyses of water and sediment samples from multiple sites along a redox gradient allow a more detailed and robust view of the evolution of the formation and transformation of iron oxide nanoparticles and colloids. For example, in this particular study, it has been shown how Zn-bearing green rust platelets exit the groundwater outflow of metal polluted waters. These platelets are known to be highly unstable in surface oxic conditions and may only be stable for minutes to hours (Legrand et al. 2004; Wang et al. 2013). Dissolved Fe^{2+} in the water oxidises rapidly and, along with Fe^{3+} released from the dissolving green rust, results in aggregates of amorphous or poorly crystalline

Si-rich spheroids approximately 20–200 nm in diameter. As the particles aggregate and settle as streambed sediments (in addition to other processes like direct precipitation of minerals in the sediment), crystallisation begins to occur in a much slower step that will eventually result in minute bladed goethite crystals growing from the surfaces of the existing particles. Although the aggregate particles may not be nanosized, they are composed of smaller particles with nanocrystalline structure and features that very likely make them more reactive than larger, more homogenous particles. For example, such nano-needles probably increase the reactive surface area for metal(loid) sorption.

As a result of the relatively homogenous nature of the suspended solids and sediments in the Gessen Creek outflow, sediment sequential extractions and water fractions provide a good idea of the distribution of metal(loid)s between water and solid phases. Some contaminants are associated with suspended particles and partition to the sediments, such as As, Zn and Cu, whereas others are associated with more mobile fractions (Ni, U). Despite strong associations of metal(loid)s with particulates, they are still easily transported downstream. Sediments are easily re-mobilised, for example during erosion of the terraces and turbulence in the creek during high flow events.

Abiotic and biotic processes are likely both involved in the oxidation and reduction of iron oxide nanoparticles and colloids at this site, as with any other mine drainage system. At a pH of ~6, abiotic oxidation by dissolved oxygen should dominate in fully oxygenated water (Williamson et al. 2006), but biotic iron oxidation still occurs along oxygen gradients (Sobolev and Roden 2002; Langwaldt and Puhakka 2003; Emerson et al. 2010). In conjunction with this research, Fabisch et al. (unpublished, see Appendix D) have found high abundances of *Gallionella* spp. in water and sediment at the outflow, terrace and creek sites, especially in the

creek sediment, but also at other creek sites in the area (Fabisch et al. 2013). *Gallionella* are microaerophilic, chemolithotrophic iron oxidizers (Hallbeck et al. 1993) that release long polymers at approximately pH 6 and higher that act as nucleating sites for amorphous and poorly crystalline iron oxides such as ferrihydrite (Banfield et al. 2000; Søgaard et al. 2001; Chan et al. 2009). Their presence at high heavy metal concentrations suggests that these organisms exhibit a greater metal tolerance than shown before. Detailed genomic analysis has recently revealed that *Gallionella* ES-2 is equipped to deal with metals and other environmental toxicants in its environment (Emerson et al. 2013). If sediment conditions become more reduced, there is a potential for metal release following biotic Fe^{III} reduction as demonstrated by Burkhardt et al. (2010) using microcosms of Gessen Creek bank soil. However, in a different study, stimulation of sulfate-reducing bacteria was shown to increase Ni (and sometimes Zn) attenuation in similar Gessen Creek soil microcosms, while U was released (Sitte et al. 2010). Bacteria involved in iron cycling in Gessen Creek bank soils have shown metal tolerance at metal concentrations well above those reported in this current study (Burkhardt et al. 2011).

Iron cycling processes are important in a wide variety of environments besides mine drainage, such as nutrients for phytoplankton that sequester CO_2 in the ocean (Nodwell and Price 2001), stratified lakes (Taillefert and Gaillard 2002; Reiche et al. 2011; S. Lu et al. 2013), intertidal marshes (Johnston et al. 2011) and in acidic, oxic environments beneath polar glaciers (Raiswell et al. 2008, 2009), to name just a few. Within this broader context, this study adds another chapter in the search for filling in missing pieces of the science of iron cycling, which is clearly highly complex and convoluted, needing field-based exploration such as the one presented here to enrich contributions made by experimental, laboratory and modelling studies.

2.7. Acknowledgements

Carol A. Johnson was financially supported by the National Science Foundation (NSF) Integrative Graduate Education and Research Trainee- ship program (grant DGE-0504196) and the NSF and the Environmental Protection Agency (EPA) through the Center for the Environmental Impli- cations of NanoTechnology (CEINT) (NSF Cooperative Agreement EF-0830093). Maria Fabisch was financially supported by the graduate research training group 'Alteration and element mobility at the microbe- mineral interface' (GRK 1257), which is funded by the German Research Foundation (Deutsche Forschungsgemeinschaft, DFG). Manuel A. Caraballo was financially supported by the Spanish Ministry of Education and the Post-doctoral International Mobility Sub-program IþDþi 2008– 2011. The authors also acknowledge the following scientists for their valuable assistance: G. Büchel for insights on the field site (Institute for Geosciences, Friedrich Schiller University (FSU) Jena, Jena, Germany); A. Kovacs (Ernst-Ruska Centre, Jülich, Germany) and M. Murayama (ICTAS Nanoscale Characterization and Fabrication Laboratory, Virginia Tech) for analytical TEM assistance and discussions; K. Eusterhues and K.-U. Totsche for SEM access, M. Wierzbiczka-Wieczorek for XRD data collection, D. Merten for ICP-AES and ICP-MS measurements (FSU Jena); J. Parks for ICP-MS measurements (Department of Civil and Environmental Engineering, Virginia Tech); H. Hildebrand for ICP-AES measurements (Helmholtz Centre Dresden-Rossendorf, Leipzig, Germany).

2.8. References

Ahmed, I.A.M., Shaw, S., and Benning, L.G. (2008) Formation of hydroxysulphate and hydroxycarbonate green rusts in the presence of zinc using time-resolved in situ small and wide angle X-ray scattering. Mineralogical Magazine, 72, 159–162.

Ahmed, I.A.M., Benning, L.G., Kakonyi, G., Sumoondur, A.D., Terrill, N.J., and Shaw, S. (2010) Formation of green rust sulfate: a combined in situ time-resolved X-ray scattering and electrochemical study. Langmuir, 26, 6593–6603.

APHA, AWWA, and WEF (1998) Standard Methods for Examination of Water and Wastewater, 20th ed. American Public Health Association, Washington DC.

Arai, Y. (2008) Spectroscopic evidence for Ni(II) surface speciation at the iron oxyhydroxides-water interface. Environmental Science & Technology, 42, 1151–1156.

Banfield, J.F., Welch, S.A., Zhang, H., Ebert, T.T., and Penn, R.L. (2000) Aggregation-based crystal growth and microstructure development in natural iron oxyhydroxide biomineralization products. Science, 289, 751–754.

Bernal, J., Dasgupta, D., and Mackay, A. (1959) The oxides and hydroxides of iron and their structural inter-relationships. Clay Minerals Bulletin, 4, 15–30.

Bigham, J.M., and Nordstrom, D.K. (2000) Iron and aluminum hydroxysulfates from acid sulfate waters. In C.N. Alpers, J.L. Jambor, and D.K. Nordstrom, Eds., Sulfate Minerals: Crystallography, Geochemistry, and Environmental Significance pp. 351–403. Reviews in Mineralogy, Mineralogical Society of America, Chantilly, Virginia.

Burkhardt, E.-M., Akob, D.M., Bischoff, S., Sitte, J., Kostka, J.E., Banerjee, D., Scheinost, A.C., and Küsel, K. (2010) Impact of biostimulated redox processes on metal dynamics in an iron-rich creek soil of a former uranium mining area. Environmental Science & Technology, 44, 177–183.

Burkhardt, E.-M., Bischoff, S., Akob, D.M., Büchel, G., and Küsel, K. (2011) Heavy metal tolerance of Fe(III)-reducing microbial communities in contaminated creek bank soils. Applied and Environmental Microbiology, 77, 3132–3136.

Caraballo, M.A., Rotting, T.S., Nieto, J.M., and Ayora, C. (2009) Sequential extraction and DXRD applicability to poorly crystalline Fe- and Al-phase characterization from an acid mine water passive remediation system. American Mineralogist, 94, 1029–1038.

Caraballo, M.A., Macías, F., Nieto, J.M., Quispe, D., and Ayora, C. (2011) Hydrochemical performance and mineralogical evolution of a dispersed alkaline substrate (DAS) remediating the highly polluted acid mine drainage in the full-scale passive treatment of Mina Esperanza (SW Spain). American Mineralogist, 96, 1270–1277.

Caraballo, M.A., Sarmiento, A.M., Sánchez-Rodas, D., Nieto, J.M., and Parviainen, A. (2011) Seasonal variations in the formation of Al and Si rich Fe-stromatolites in the highly polluted acid mine drainage of Agua Agria Creek (Tharsis, SW Spain). Chemical Geology, 284, 97–104.

Caraballo, M.A., Rimstidt, J.D., Macias, F., Nieto, J.M., and Hochella Jr, M.F. (2013) Metastability, nanocrystallinity and pseudo-solid solution constraints to schwertmannite solubility. Chemical Geology, 360/361, 22–31.

Carbone, C., Di Benedetto, F., Marescotti, P., Martinelli, A., Sangregorio, C., Cipriani, C., Lucchetti, G., and Romanelli, M. (2005) Genetic evolution of nanocrystalline Fe oxide and oxyhydroxide assemblages from the Libiola mine (eastern Liguria, Italy): structural and microstructural investigations. European Journal of Mineralogy, 17, 785–795.

Chan, C.S., Fakra, S.C., Edwards, D.C., Emerson, D., and Banfield, J.F. (2009) Iron oxyhydroxide mineralization on microbial extracellular polysaccharides. Geochimica et Cosmochimica Acta, 73, 3807–3818.

Christiansen, B.C., Balic-Zunic, T., Dideriksen, K., and Stipp, S.L.S. (2009) Identification of green rust in groundwater. Environmental Science & Technology, 43, 3436–3441.

Cismasu, A.C., Michel, F.M., Tcaciuc, A.P., Tyliszczak, T., and Brown, Jr, G.E. (2011) Composition and structural aspects of naturally occurring ferrihydrite. Comptes Rendus Geoscience, 343, 210–218.

Deutsch, W. (1997) Groundwater Geochemistry: Fundamentals and Applications to Contamination p. p.35. CRC Press, Boca Raton, FL.

Dold, B., Gonzalez-Toril, E., Aguilera, A., Lopez-Pamo, E., Cisternas, M.E., Bucchi, F., and Amils, R. (2013) Acid rock drainage and rock weathering in Antarctica: Important sources for iron cycling in the Southern Ocean. Environmental Science & Technology, 47, 6129–6136.

Dyer, J. A., Trivedi, P., Scrivner, N.C., and Sparks, D.L. (2004) Surface complexation modeling of zinc sorption onto ferrihydrite. Journal of Colloid and Interface Science, 270, 56–65.

Dykstra, M.J. (1993) A manual of applied techniques for biological electron microscopy. Plenum Press, New York.

Emerson, D., Fleming, E.J., and McBeth, J.M. (2010) Iron-oxidizing bacteria: an environmental and genomic perspective. Annual Review of Microbiology, 64, 561–583.

Emerson, D., Field, E.K., Chertkov, O., Davenport, K.W., Goodwin, L., Munk, C., Nolan, M., and Woyke, T. (2013) Comparative genomics of freshwater Fe-oxidizing bacteria: implications for physiology, ecology, and systematics. Frontiers in microbiology, 4, 254.

Fabisch, M., Beulig, F., Akob, D.M., and Küsel, K. (2013) Surprising abundance of Gallionella-related iron oxidizers in creek sediments at pH 4.4 or at high heavy metal concentrations. Frontiers in Microbiology, 4, 1–12.

Feder, F., Trolard, F., Klingelhöfer, G., and Bourrié, G. (2005) In situ Mössbauer spectroscopy: Evidence for green rust (fougerite) in a gleysol and its mineralogical transformations with time and depth. Geochimica et Cosmochimica Acta, 69, 4463–4483.

Ford, R.G., Bertsch, P.M., and Farley, K.J. (1997) Changes in transition and heavy metal partitioning during hydrous iron oxide aging. Environmental Science and Technology, 31, 2028–2033.

French, R.A., Caraballo, M.A., Kim, B., Rimstidt, J.D., Murayama, M., and Hochella Jr, M.F. (2012) The enigmatic iron oxyhydroxysulfate nanomineral schwertmannite: Morphology, structure, and composition. American Mineralogist, 97, 1469–1482.

Gautier, J., Grosbois, C., Floc'h, J.P., and Martin, F. (2006) Transformation of natural As-associated ferrihydrite downstream of a remediated mining site. European Journal of Mineralogy, 18, 187–195.

Geletneky, J.W., Buechel, G., and Paul, M. (2002) Impact of acid rock drainage in a discrete catchment area of the former uranium mining site of Ronneburg (Germany). In 9th International Tailings and Mine Waste Conference pp. 67–72. Swets & Zeitlinger.

Genovese, A., and Mellini, M. (2007) Ferrihydrite flocs, native copper nanocrystals and spontaneous remediation in the Fosso dei Noni stream, Tuscany, Italy. Applied Geochemistry, 22, 1439–1450.

Glauert, A.M., and Lewis, P.R. (1998) Practical Methods in Electron Microscopy Vol. 17: Biological Specimen Preparation for Transmission Electron Microscopy pp. 40–43. Portland Press, London.

Guo, H., and Barnard, A.S. (2013) Naturally occurring iron oxide nanoparticles: morphology, surface chemistry and environmental stability. Journal of Materials Chemistry A, 1, 27.

Guo, H., Xu, H., and Barnard, A.S. (2013) Can hematite nanoparticles be an environmental indicator? Energy & Environmental Science, 6, 561.

Hallbeck, L., Ståhl, F., and Pedersen, K. (1993) Phylogeny and phenotypic characterization of the stalk-forming and iron-oxidizing bacterium *Gallionella ferruginea*. Journal of General Microbiology, 139, 1531–5.

Hassellöv, M., and von der Kammer, F. (2008) Iron oxides as geochemical nanovectors for metal transport in soil-river systems. Elements, 4, 401–406.

Hazemann, J.-L., Berar, J.F., and Manceau, A. (1991) Rietveld studies of the aluminium-iron substitution in synthetic goethite. Materials Science Forums, 79-82, 821–826.

Heikkinen, P.M., and Räisänen, M.L. (2009) Trace metal and As solid-phase speciation in sulphide mine tailings – Indicators of spatial distribution of sulphide oxidation in active tailings impoundments. Applied Geochemistry, 24, 1224–1237.

Hiemstra, T., Antelo, J., Rahnemaie, R., and Riemsdijk, W.H. Van (2010) Nanoparticles in natural systems I: The effective reactive surface area of the natural oxide fraction in field samples. Geochimica et Cosmochimica Acta, 74, 41–58.

Hochella Jr, M.F., Moore, J.N., Golla, U., and Putnis, A. (1999) A TEM study of samples from acid mine drainage systems: Metal-mineral association with implications for transport. Geochimica et Cosmochimica Acta, 63, 3395–3406.

Hochella Jr, M.F., Lower, S.K., Maurice, P.A., Penn, R.L., Sahai, N., Sparks, D.L., and Twining, B.S. (2008) Nanominerals, mineral nanoparticles, and Earth systems. Science, 319, 1631–1635.

Hochella Jr, M.F., Aruguete, D., and Kim, B. (2012) Naturally occurring inorganic nanoparticles: General assessment and a global budget for one of Earth's last unexplored major geochemical components. In A.S. Barnard and H. Guo, Eds., Nature's Nanostructures pp. 1–31. Pan Stanford Pte Ltd.

Johnston, S.G., Keene, A.F., Burton, E.D., Bush, R.T., and Sullivan, L.A. (2011) Iron and arsenic cycling in intertidal surface sediments during wetland remediation. Environmental Science & Technology, 45, 2179–85.

Kim, B., Park, C.-S., Murayama, M., and Hochella Jr, M.F. (2010) Discovery and characterization of silver sulfide nanoparticles in final sewage sludge products. Environmental Science & Technology, 44, 7509–7514.

Kim, B., Murayama, M., Colman, B.P., and Hochella, M.F. (2012) Characterization and environmental implications of nano- and larger TiO(2) particles in sewage sludge, and soils amended with sewage sludge. Journal of Environmental Monitoring, 14, 1129–1137.

Langwaldt, J.H., and Puhakka, J.A. (2003) Competition for oxygen by iron and 2,4,6-trichlorophenol oxidizing bacteria in boreal groundwater. Water Research, 37, 1378–1384.

Lee, G., Bigham, J.M., and Faure, G. (2002) Removal of trace metals by coprecipitation with Fe, Al and Mn from natural waters contaminated with acid mine drainage in the Ducktown Mining District, Tennessee. Applied Geochemistry, 17, 569–581.

Legrand, L., Mazerolles, L., and Chaussé, A. (2004) The oxidation of carbonate green rust into ferric phases: solid-state reaction or transformation via solution. Geochimica et Cosmochimica Acta, 68, 3497–3507.

Lu, S., Chourey, K., Reiche, M., Nietzsche, S., Shah, M.B., Neu, T.R., Hettich, R.L., and Küsel, K. (2013) Insights into the structure and metabolic function of microbes that shape pelagic

iron-rich aggregates (“iron snow”). Applied and Environmental Microbiology, 79, 4272–4281.

Lu, S.-G., Sun, F.-F., and Zong, Y.-T. (2013) Occurrence, structure and mineral phases of nanoparticles in an anthrosol. Pedosphere, 23, 273–280.

Macías, F., Caraballo, M.A., and Nieto, J.M. (2012) Environmental assessment and management of metal-rich wastes generated in acid mine drainage passive remediation systems. Journal of Hazardous Materials, 229-230, 107–114.

Marescotti, P., Carbone, C., Comodi, P., Frondini, F., and Lucchetti, G. (2012) Mineralogical and chemical evolution of ochreous precipitates from the Libiola Fe–Cu-sulfide mine (Eastern Liguria, Italy). Applied Geochemistry, 27, 577–589.

Mills, S.J., Christy, A.G., Génin, J.-M.R., Kameda, T., and Colombo, F. (2012) Nomenclature of the hydrotalcite supergroup: Natural layered double hydroxides. Mineralogical Magazine, 76, 1289–1336.

Nodwell, L.M., and Price, N.M. (2001) Direct use of inorganic colloidal iron by marine mixotrophic phytoplankton. Limnology and Oceanography, 46, 765–777.

Nordstrom, D.K., and Wilde, F.D. (1998) Reduction-Oxidation Potential (Electrode Method). In F.D. Wilde and D.B. Radtke, Eds., U.S. Geological Survey TWRI Book 9: Handbooks for Water-Resources Investigations. U.S. Geological Survey.

Pantke, C., Obst, M., Benzerara, K., Morin, G., Ona-Nguema, G., Dippon, U., and Kappler, A. (2012) Green rust formation during Fe(II) oxidation by the nitrate-reducing Acidovorax sp. strain BoFeN1. Environmental Science & Technology, 46, 1439–1446.

Paul, M., Gengnagel, M., and Baacke, D. (2006) Integrated water protection approaches under the WISMUT project: The Ronneburg case. In B.J. Merkel and A. Hasche-Berger, Eds., Uranium in the Environment: Mining Impact and Consequences pp. 369–379. Springer-Verlag, Berlin.

Penn, R.L., Oskam, G., Strathmann, T.J., Searson, P.C., Stone, A.T., and Veblen, D.R. (2001) Epitaxial assembly in aged colloids. Journal of Physical Chemistry B, 105, 2177–2182.

Perez-Lopez, R., Asta, M.P., Roman-Ross, G., Nieto, J.M., Ayora, C., and Tuccoulou, R. (2011) Synchrotron-based X-ray study of iron oxide transformations in terraces from the Tinto-Odiel river system: Influence on arsenic mobility. Chemical Geology, 280, 336–343.

Perret, D., Gaillard, J.-F., Dominik, J., and Atteia, O. (2000) The diversity of natural hydrous iron oxides. Environmental Science & Technology, 34, 3540–3546.

Plathe, K.L., von der Kammer, F., Hassellöv, M., Moore, J., Murayama, M., Hofmann, T., and Hochella, M.F. (2010) Using FlFFF and aTEM to determine trace metal–nanoparticle associations in riverbed sediment. Environmental Chemistry, 7, 82.

Raiswell, R., Benning, L.G., Davidson, L., and Tranter, M. (2008) Nanoparticulate bioavailable iron minerals in icebergs and glaciers. Mineralogical Magazine, 72, 345–348.

Raiswell, R., Benning, L.G., Davidson, L., Tranter, M., and Tulaczyk, S. (2009) Schwertmannite in wet, acid and oxic microenvironments beneath polar and polythermal glaciers. Geology, 37, 431–434.

Rauret, G., López-Sánchez, J.F., Sahuquillo, A., Rubio, R., Davidson, C., Ure, A., and Quevauviller, P. (1999) Improvement of the BCR three step sequential extraction procedure prior to the certification of new sediment and soil reference materials. Journal of Environmental Monitoring, 1, 57–61.

Reiche, M., Lu, S., Ciobota, V., Neu, T.R., Nietzsche, S., Rösch, P., Popp, J., and Küsel, K. (2011) Pelagic boundary conditions affect the biological formation of iron-rich particles (iron snow) and their microbial communities. Limnology and Oceanography, 56, 1386–1398.

Rennert, T., Eusterhues, K., De Andrade, V., and Totsche, K.U. (2012) Iron species in soils on a mofette site studied by Fe K-edge X-ray absorption near-edge spectroscopy. Chemical Geology, 332-333, 116–123.

Sanchez-Espana, J., Pastor, E.S., and Lopez-Pamo, E. (2007) Iron terraces in acid miner drainage systems: A discussion about the organic and inorganic factors involved in their formation through observations from the Tintillo acidic river (Rio Tinto mine, Huelva, Spain). Geosphere, 3, 133–151.

Simon, L., François, M., Refait, P., Renaudin, G., Lelaurain, M., and Génin, J.-M.R. (2003) Structure of the Fe(II-III) layered double hydroxysulphate green rust two from Rietveld analysis. Solid State Sciences, 5, 327–334.

Sitte, J., Akob, D.M., Kaufmann, C., Finster, K., Banerjee, D., Burkhardt, E.-M., Kostka, J.E., Scheinost, A.C., Büchel, G., and Küsel, K. (2010) Microbial links between sulfate reduction and metal retention in uranium- and heavy metal-contaminated soil. Applied and Environmental Microbiology, 76, 3143–3152.

Skovbjerg, L.L. (2005) Reduction of hexavalent chromium by green rust sulphate: Determination of end product and reduction mechanism. University of Copenhagen.

Sobolev, D., and Roden, E.E. (2002) Evidence for rapid microscale bacterial redox cycling of iron in circumneutral environments. Antonie van Leeuwenhoek, 81, 587–597.

Søgaard, E.G., Aruna, R., Abraham-Peskir, J., and Bender Koch, C. (2001) Conditions for biological precipitation of iron by *Gallionella ferruginea* in a slightly polluted ground water. Applied Geochemistry, 16, 1129–1137.

Tabatabai, M.A. (1974) A rapid method for determination of sulfate in water samples. Environmental Letters, 7, 237–243.

Taillefert, M., and Gaillard, J.-F. (2002) Reactive transport modeling of trace elements in the water column of a stratified lake: iron cycling and metal scavenging. Journal of Hydrology, 256, 16–34.

Tamura, H., Goto, K., Yotsuyanagi, T., and Nagayama, M. (1974) Spectrophotometric determination of iron(II) with 1,10-phenanthroline in the presence of large amounts of iron(III). Talanta, 21, 314–318.

Trolard, F., and Bourrié, G. (2012) Fougerite a natural layered double hydroxide in gley soil: habitus, structure, and some properties. In M. Valaskova and G.S. Martynkova, Eds., Clay Minerals in Nature - Their Characterization, Modification, and Application pp. 171–188. InTech.

Vins, J., Subrt, J., Zapletal, Z., and Hanousek, F. (1987) Preparation and properties of green rust type substances. Collection of Czechoslovak Chemical Communications, 52, 93–102.

Wang, X., Liu, F., Tan, W., Feng, X., and Koopal, L.K. (2013) Transformation of hydroxycarbonate green rust into crystalline iron (hydr)oxides: Influences of reaction conditions and underlying mechanisms. Chemical Geology, 351, 57–65.

Wankel, S.D., Adams, M.M., Johnston, D.T., Hansel, C.M., Joye, S.B., and Girguis, P.R. (2012) Anaerobic methane oxidation in metalliferous hydrothermal sediments: influence on carbon flux and decoupling from sulfate reduction. Environmental Microbiology, 14, 2726–2740.

Waychunas, G.A., Kim, C.S., and Banfield, J.F. (2005) Nanoparticulate iron oxide minerals in soils and sediments: unique properties and contaminant scavenging mechanisms. Journal of Nanoparticle Research, 7, 409–433.

Williamson, M.A., Kirby, C.S., and Rimstidt, J.D. (2006) Iron dynamics in acid mine drainage. In 7th International Conference on Acid Rock Drainage (ICARD) pp. 2411–2423. American Society of Mining and Reclamation, St. Louis, MO.

Wismut GmbH (2011) Umweltbericht 2010 pp. 1–94. Chemnitz.

World Health Organization (2011) Chemical Aspects. In Guidelines for drinking-water quality pp. 155–201. WHO Press, Geneva, Switzerland.

Zaffiro, A., Zimmerman, M., Wendelken, S., Smith, G., and Munch, D. (2011) Method 281.7: Determination of hexavalent chromium in drinking water by ion chromatoraphy with post-

column derivatization and UV-visible spectroscopic detection. Environmental Protection Agency, Cincinnati, OH.

Zegeye, A., Bonneville, S., Benning, L.G., Sturm, A., Fowle, D.A., Jones, C., Canfield, D.E., Ruby, C., MacLean, L.C., Nomosatryo, S., and others (2012) Green rust formation controls nutrient availability in a ferruginous water column. Geology, 40, 599–602.

3. POLYCRYSTALLINITY OF GREEN RUST MINERALS AND THEIR SYNTHETIC ANALOGS: IMPLICATIONS FOR PARTICLE FORMATION AND REACTIVITY IN COMPLEX SYSTEMS

Carol A. Johnson,[A] Mitsuhiro Murayama,[B] Kirsten Küsel,[C,D] and Michael F. Hochella, Jr.[A]

[A]Department of Geosciences, Virginia Polytechnic and State University, 1405 Perry St, Blacksburg, VA 24061, USA

[B]Department of Materials Science and Engineering, Virginia Polytechnic and State University, 445 Old Turner St, Blacksburg, VA 24061, USA

[C]Institute of Ecology, Friedrich Schiller University Jena, Dornburgerstrasse 159, D-07743 Jena, Germany

[D]German Centre for Integrative Biodiversity Research (iDiv) Halle-Jena-Leipzig, Deutscher Platz 5e, D-04103 Leipzig, Germany

To be submitted to American Mineralogist

3.1. Abstract

We demonstrate in this study that natural green rust nanoparticles and their synthetic analogs can be complex polycrystalline phases composed of crystallites only a few nanometers in size, and often include nano-regions of amorphous material. The natural green rusts are Zn-bearing pseudo-hexagonal platelets previously identified by us in the contaminated mine drainage of the former Ronneburg uranium mine in Germany (Johnson et al. 2014). We also identified Ni- and Cu-bearing green rust platelets in the sediment underlying the drainage outflow 20 m downstream, and, using dark field transmission electron microscopy (DF-TEM), found that these natural green rusts are not usually structurally-coherent single crystals. Synthetic sulfate green rusts are also polycrystalline and composed of crystallites of only a few nanometers in size, though different synthesis conditions produced different variations on this theme. While pseudo-hexagonal platelets are the typical morphology of green rust, we also synthesized green rust nanorods, which has not previously been reported. In addition to the known characteristics of green rusts (including very large aspect ratio and surface area to volume ratio, and the redox

properties allowed by the structural mixture of Fe^{II} and Fe^{III}), these polycrystalline platelets exhibit a high abundance of defect sites and likely a rough surface topography. The combination of these characteristics has important implications for the reactivity of green rust with biogeochemical interfaces in natural, anthropogenic, and industrial systems.

3.2. Introduction

There are many complex factors that influence mineral interactions with the surrounding components of Earth systems. Composition, surface atomic structure, crystal morphology, size, surface charge and surface topography are just a few mineral properties that affect their behavior in these complex natural settings (Hochella et al. 2012 and references therein). Nanoparticles have especially high reactivity compared to larger particles due to their small size (high surface area to volume ratio) and comparatively high-energy surface topography and atomic structure. Nanoparticles of the extensive family of iron oxides and their role in the overall biogeochemical cycling of iron in, on, and above the Earth has been comprehensively studied, as well as the intimate link with the fate and transport of environmental pollutants (e.g. Banfield and Zhang 2001; Waychunas et al. 2005; Raiswell 2011; Taylor and Konhauser 2011; Dong and Lu 2012; and many references therein). Even though these are not new concepts, geochemists continue to discover nanoscale nuances about iron oxide mineral structure and composition that change the way we think about their interactions with environmental systems. For example, schwertmannite is an iron oxyhydroxysulfate phase that is considered to be a mineral, but upon careful examination by high resolution transmission electron microscopy (HR-TEM), was found to consist of both nanocrystalline and amorphous domains (French et al. 2012). The long-range order that is fundamental to the definition of a mineral does not exist in these natural samples. Studies like these that use analytical TEM techniques are useful for determining heterogeneities

in nanoscale composition and structure, which highly influence a mineral's reactivity with its surroundings. Minerals with shorter range order, abundant structural defects, and variable/gradational compositions are likely quite common in nature (Caraballo et al. in press, and references therein).

In the complex system of anoxic underground mine drainage, another example of an iron oxide mineral, green rust, was found that appears to contain both areas of crystalline and amorphous material (Johnson et al. 2014), which warranted further investigation. Green rusts are a family of minerals that contain both reduced and oxidized iron species (Fe^{II} and Fe^{III}) within two iron hydroxide layers (aka a layered double hydroxide, or LDH), separated by an interlayer containing a wide array of anions and cations somewhat analogous to clays (Trolard and Bourrié 2012). They typically are found as very thin pseudo-hexagonal platelets, from a very few to a few tens of nanometers thick (Christiansen et al. 2009; Trolard and Bourrié 2012; Johnson et al. 2014). Keeping in mind that the crystal repeat distance in the plate thickness direction is close to one nanometer, these plates that are typically hundreds to thousands of nanometers wide have an exceptionally high surface to volume ratio. This, combined with the mixed valence states of iron present (plus other crystal structural elements discovered in this study and discussed in detail below), results in a high potential for chemical reaction.

In nature, green rusts have been found to take up Ni (Zegeye et al. 2012) and Zn (Johnson et al. 2014). Synthesized green rusts have been shown to reduce a variety of metals (coupled to structural Fe^{II} oxidation) such as Cr^{VI} (Williams and Scherer 2001; Skovbjerg et al. 2006) and Ag^{I}, Ag^{III}, Cu^{II}, and Hg^{II} (O'Loughlin et al. 2003), to reduce or dechlorinate organics such as CCl_4 (Erbs et al. 1999) and dichloroethylene (Han et al. 2012), and to sorb As (Jönsson and Sherman 2008) and Ni (Parmar and Beveridge 2001). Green rusts are also commonly found as a

corrosion product of steels (Stampfl 1969; Swietlik et al. 2012), and have applications in industry (Ayala-Luis et al. 2010).

Research on the structure and reactivity of the green rust family has increased considerably in the past decade. Nevertheless, compared to other iron oxide minerals such as goethite, hematite, or even poorly crystalline ferrihydrite and schwertmannite, large gaps in a thorough understanding of green rusts remain. Green rust was only first positively identified in nature in 1997, in a reductomorphic soil (Trolard et al. 1997), and since then has only been conclusively identified in relatively few natural sites for example in groundwater (Christiansen et al. 2009), mine drainage sediments (Bearcock et al. 2006), an iron-rich lake (Zegeye et al. 2012), and a mofette soil (Rennert et al. 2012). It can form biotically from the bacterial reduction of various iron oxides such as lepidocrocite (Ona-Nguema et al. 2002; O'Loughlin et al. 2007; Jorand et al. 2013), ferrihydrite (Kukkadapu et al. 2004), and hydrous ferric oxide (Parmar and Beveridge 2001). Green rust can also form abiotically via the reduction of ferric oxides as well as the oxidation of dissolved Fe^{II} (Géhin et al. 2002; Ruby et al. 2003).

A specific type of green rust, fougerite, was only accepted as the first green rust mineral in 2004 (Trolard et al. 2007), but the structures and formulas for different green rusts are continuously re-evaluated and modified (Mills et al. 2012). For example, Simon et al. (2003) determined sulfate green rust (GR-SO_4, $Fe^{II}_4Fe^{III}_2(OH)_{12}\ SO_4 \bullet \sim 8H_2O$) to be in the $P\bar{3}1m$ space group (#162) with lattice parameters of $a = b = 5.524$ Å, c = 11.011 Å, and an interlayer arrangement characteristic of the hydrotalcite group (within the hydrotalcite supergroup). Then Christiansen et al. (2009) further refined the formula for sulfate green rust to be $NaFe^{II}_6Fe^{III}_3(SO_4)_2(OH)_{18} \bullet 12H_2O$ (now designated GR-Na,SO_4), thereby rearranging the SO_4^{2-} molecules in the interlayer and showing how Na^+ is necessary for charge balance. The

crystallographic space group for GR-Na,SO_4 is $P\bar{3}$ (#147) with $a = b = 9.529$ Å, $c = 10.969$ Å and an interlayer arrangement characteristic of the nikischerite group (still within the hydrotalcite supergroup) (Christiansen et al. 2009).

Green rust minerals are generally thought to be geochemically important and widespread in anoxic settings. We suspect that it is only rarely collected in the field and preserved for analysis because it is exceptionally ephemeral under oxidizing conditions. In addition, while studies on synthetic green rusts have been performed in order to try to better understand their formation and reactivity, it is important that the synthetic particles are reasonably similar to ones that are found in nature. Structure and composition are two critical mineral attributes that can be probed at the nanoscale with analytical TEM, making this a logical starting point for the comparison between natural and synthetic green rusts. The only published studies that include HR-TEM of green rusts indicate that they were single, coherent crystals (Skovbjerg et al. 2006; Zegeye et al. 2012), but our previous work has shown the possibility of less coherent nano-sized domains in the green rust from mine drainage outflow (Johnson et al. 2014). In this study, we examined more thoroughly the same green rust particles from this outflow, as well as additional green rusts from sediments at the site, using dark field (DF) TEM. DF-TEM can be used to understand the structural coherency of the particles. It provides information about whether a particle is a single continuous crystal or polycrystalline. Polycrystalline materials will exhibit light and dark areas in the DF image, and fast Fourier transform (FFT) patterns calculated from HR-TEM images (equivalent to electron diffraction patterns) will show crystallite rotation and tilting. These same techniques, along with compositional analysis (nanoscale energy dispersive x-ray spectroscopy) were applied to sulfate green rusts that we synthesized in the laboratory to

see if they exhibited similar features. With this information, we infer possible formation mechanisms and potential effect on reactivity.

3.3. Materials and methods

3.3.1. Natural green rust sampling and site characterization

Green rust mineral nanoparticles were identified in the anoxic outflow from the former Ronneburg uranium mine as previously reported in Johnson et al. (2014). Green rust particles were also identified in the sediment of iron-rich terraces at the same site, where the drainage water flows over a creek bank 20 m from the site of outflow. Sampling details, including the geochemical characteristics of water and sediment along the flow path, can be found in Johnson et al. (2014). Critical details are described here in brief. Water samples at the outflow site were collected by filling 50-mL plastic centrifuge tubes to the top, without headspace in order to reduce exposure to air. Sediment samples from the terrace site were also collected in a similar manner. Samples were handled thereafter in an anoxic chamber, and sediments were additionally diluted with deoxygenated ultrapure water (18.2 MΩ, flushed with N_2, Milli-Q Advance, Millipore). The pH of the outflow water on October 25, 2011 (the date green rust was found) was 5.75, with an Eh of 260 mV (corrected to the standard hydrogen electrode) and a dissolved oxygen concentration of 0.6 mg/L. The concentration of dissolved (< 0.2 um) Fe^{II} is 5.6 (0.1) mM, and dissolved SO_4^{2-} is 40 (9) mM. In addition, the microbial community has been characterized and a number of iron oxidizing bacteria (related to *Gallionella spp.*, 49% of the community) and iron reducing bacteria (related to *Albidoferax ferrireducens* and *Geobacter spp*, 21%) were found in the outflow water on October 25, 2011 (Fabisch et al., submitted).

3.3.2. Green rust synthesis

Sulfate green rust was synthesized via a co-precipitation synthesis method based on the methods from Géhin et al. (2002) and Ruby et al. (2003, 2006). A solution of NaOH was added via a slow titration or a fast addition to a solution of hydrated Fe^{II} and Fe^{III} sulfate salts ($FeSO_4 \bullet 7H_2O$, JT Baker, ACS reagent, freshly purchased and stored at 4°C; $Fe_2(SO_4)_3 \bullet nH_2O$, reagent brand and grade given in Table 3.1, with approximately six waters of hydration as determined by ICP-AES). The syntheses were performed both in air with ultrapure water (Barnstead Nanopure, 18.2 MΩ) and in an anoxic chamber (Coy, N_2 gas with 1% H_2) with deoxygenated ultrapure water (boiled and purged with N_2) in order to determine if anoxic conditions were necessary for green rust formation. The key reaction parameters were the molar ratios nFe^{II}/nFe^{III} and nOH^-/nFe_{total}, which were varied, and given in Table 3.1 along with the general reaction conditions. The syntheses have been re-named GR-A, GR-B, GR-C and GR-D. Not all attempted syntheses are described here.

Table 3.1. Synthesis conditions where sulfate green rust II was formed according to XRD.
Concentrations are in moles per liter (M), ratios are molar (n) ratios.

Synth. name	$[Fe^{II}]$ (M)	$[Fe^{III}]$ (M)	nFe^{II}/nFe^{III}	$[Fe_{total}]$ (M)	nFe^{III}/nFe_{total}	Fe_{soln} (L)	nOH^-/nFe_{total}	$[OH^-]$ (M)	OH^- added (L)	Anoxic?	Dumped or titrated OH^-?
GR-A	0.134	0.062	2.15	0.196	0.32	0.1	2.04	0.80	0.05	Yes	titrated
GR-B	0.144	0.055	2.63	0.199	0.28	0.1	2.01	0.40	0.10	No	dumped
GR-C	0.144	0.055	2.60	0.199	0.28	0.1	2.06	0.41	0.10	Yes	dumped
GR-D	0.075	0.082	0.91	0.160	0.48	0.1	1.03	0.41	0.04	Yes	titrated

$Fe_2(SO_4)_3 \bullet nH_2O$ reagents used: 97%, "pentahydrate," Acros Organics (GR-A); puriss p.a., 21-23% Fe basis, Sigma-Aldrich (GR-B, C); GR grade, EM Science (GR-D).

3.3.3. Transmission electron microscopy

Aliquots from both natural and synthetic samples were diluted with anoxic ultrapure water. A 10-uL drop was placed on a TEM grid (lacey carbon on copper mesh, Electron

Microscopy Sciences, or ultrathin carbon on lacey carbon on copper mesh, Ted Pella), and was immediately wicked away with a lint-free wipe, followed by rinsing twice with ultrapure deoxygenated water to remove salts while preventing oxidation. Sample grids were stored anoxically in a N_2-flushed plastic container (SampleSaver, South Bay Technologies). Scanning electron microscopy (SEM, FEI Quanta 600 and LEO Zeiss 1550 with field emission sources) was first used to scan the grids for areas of interest, followed by further analysis by TEM (primarily JEOL 2100 with a LaB_6 thermionic source operated at 200kV, also FEI Titan with a field emission source operated at 300kV). To mitigate beam damage, we reduced the beam current by over 80% by using a 50 μm C2 aperture (compared to a 120 μm one) and a medium spot size. Structural information was obtained by both selected area electron diffraction (SAED) of large areas and fast Fourier transformation (FFT) of high-resolution images (HR-TEM) and analyzed using the program *Digital Micrograph* (Gatan Inc). Dark field (DF) imaging was used to obtain information on the polycrystalline nature of the particles by placing a small (5 μm) objective aperture around the center beam and tilting the beam until the hkl reflection of interest (in SAED mode) was aligned with the aperture. In imaging mode, all areas of the crystal that diffract the electrons to that particular hkl appear bright. Particles that are single crystals will appear as one bright area, while polycrystalline particles will exhibit a bright spotty pattern with dark areas in-between. Elemental composition was obtained by energy dispersive X-ray spectroscopy (EDS), and semi-quantitative atomic percentages were calculated with the ratio (thin film approximation) standardless method using the program *Analysis Station* (JEOL Ltd). Nanoprobe EDS was performed on the FEI Titan operated in scanning transmission electron microscopy (STEM) mode, and Si/Fe atomic ratios were calculated using the program *TEM Imaging and Analysis* (TIA, FEI).

3.3.4. X-ray diffractometry

Sample aliquots were filtered through a 0.45-μm membrane and rinsed with a 1:1 solution of glycerol to deoxygenated ultrapure water, which allowed the material to be stable in air for at least 24 hours (as determined by comparing the XRD patterns at the beginning and end of this period). Material was scraped off the filters, lightly smeared onto a zero background silica plate or flat aluminum plate and analyzed (MiniFlexII, Rigaku, Cu Kα source, 30 kV, 15 mA, 0.02-0.5 °/step, 2 s/step, sample rotation). Some preferential orientation along the basal (001) plane occurred with this technique. An estimation of crystallite size based on peak broadening was calculated using the Scherrer equation, $L_{hkl} = \frac{K\lambda}{\beta_{hkl} cos\theta}$, where L is the crystallite size perpendicular to the hkl crystallographic plane, λ = the X-ray wavelength, β = is the full width at half maximum of the XRD peak in radians, and θ is the Bragg diffraction angle (Scherrer 1918; Lavina et al. 2014). K is the Scherrer constant, or shape factor, which varies around unity (e.g. 0.89 for a spherical crystallite with no lattice strain (Klug and Alexander 1974), 0.94 for a cube (Klug and Alexander 1974), and 0.998 for a right cylinder (Vargas et al. 1983)). Crystallite size estimations are over-estimations due to a variety of factors that can cause peak broadening, including instrument factors and crystallite strain in addition to crystallite size and shape (Klug and Alexander 1974; Lavina et al. 2014). The Scherrer equation is only valid for crystallites less than about 100 nm (Lavina et al. 2014).

3.4. Results

3.4.1. Natural green rust

Pseudo-hexagonal green rust platelets up to approximately 1 μm in diameter were found in microoxic, slightly acidic mine groundwater outflow site in samples taken from the former

Ronneburg uranium mine (Germany) as was previously described in Johnson et al. (2014). In this study, we characterized them further by TEM. Many other platelets were smaller and exhibited rounder edges, possibly in various stages of dissolution, but had the exact same electron diffraction pattern as the pseudo-hexagonal platelets. Thus, we believe they have very similar crystal structures. The hexagonal electron diffraction pattern (e.g. Figure 3.2c) exhibited by the natural particles is not unique to green rust. The d-spacing values (2.56 ± 0.07 and 1.50 ± 0.03 Å) actually match those for hematite oriented along the [001] zone axis (c-axis) (2.52 and 1.45 Å for hematite, compared to 2.76 and 1.59 Å for sulfate green rust), but they also exactly match the pattern and d-spacings for the synthetic materials in this study, which were verified to be sulfate green rust by XRD. The hkl reflection indices are identical for hematite and sulfate green rust oriented along the [001], and we will therefore refer to indices instead of d-spacings when discussing SAED and DF imaging. Throughout the remainder of this paper, we have chosen the sulfate green rust II structure ($P\bar{3}1m$) proposed by Simon et al. (2003) as our reference structure.

HR-TEM of the platelets as previously reported (Johnson et al. 2014) indicated the possibility of a non-coherent green rust crystal structure, due to the presence of both amorphous areas and nano-sized crystallites that were perhaps slightly misaligned. In this study, STEM EDS with a spot size of approximately 1 nm was used to compare the compositions of the dark (crystalline) and light (amorphous) regions of one platelet, as shown in Figure 3.1. Dark regions had lower Si/Fe ratios (e.g. 0.12, 0.19 in two measurements made) compared to the light regions (e.g. 0.44, 0.47). Interestingly, Zn and S were associated with the dark regions but not the light regions.

These results led to further investigations with a combination of HR-TEM and DF imaging, as shown in Figure 3.2. The platelet shown in Figure 3.2a,b has a pseudo-hexagonal morphology, and its SAED pattern (Figure 3.2c) shows a hexagonal arrangement with slightly elongated spots that is typical of these platelets. Based on the assumed crystal structure, the pattern was indexed to be a [001] zone axis pattern. Three DF images of the platelet (Figure 3.2d-f) were taken by selecting the 030, $\bar{3}30$, and $\bar{3}00$ reflections (circled in Figure 3.2c) in order to examine the coherence of the platelet crystallinity. The crystallites contributing to the chosen reflection are represented in the image by bright areas, which in this case are only a few nm in diameter (2.0 ± 1.1 nm as determined from 50 measurements). Additional pseudo-hexagonal platelets were chosen for DF imaging; these produced similar results. Lattice fringes are difficult to see in the HR-TEM images (Figures 3.2g, i, j, l) but weak FFT spots are present (Figures 3.2h, k). FFT patterns calculated from whole HR-TEM images (e.g. inset in Figure 3.2g) matched the SAED patterns well. When comparing FFTs from different areas of the particle, the reflections represented by the brightest spots were slightly different (Figures 3.2h, k), though they were aligned, meaning that different areas of the particle were tilted with respect to each other. Semi-quantitative analysis of the EDS spectrum (Figure 2m) gave an atomic Fe/S ratio of 14, which is higher than typically reported values of sulfate green rust, which range from 4.5-6 for the structural formulas considered here (Simon et al. 2003; Christiansen et al. 2009). A significant Si peak is also present, along with a trace amount of Zn, very similar to what was reported for other green rust particles in Johnson et al. (2014).

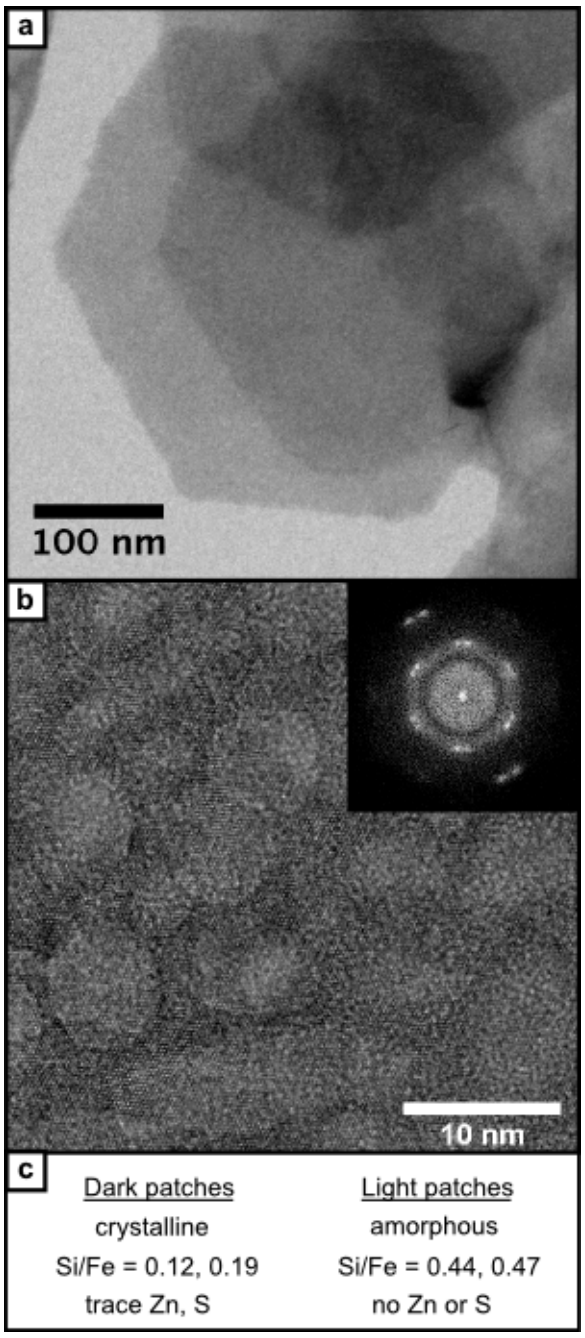

Figure 3.1. Pseudo-hexagonal natural green rust platelet from mine drainage outflow water. (a) TEM image of an aggregate of platelets, (b) HR-TEM image showing dark and light patches, with an inset of the FFT pattern showing the two stacked particles slightly rotated crystallographically with respect to each other, (c) results from comparing the STEM EDS (1 nm spot size) analyses of two dark and two light patches (EDS data not shown).

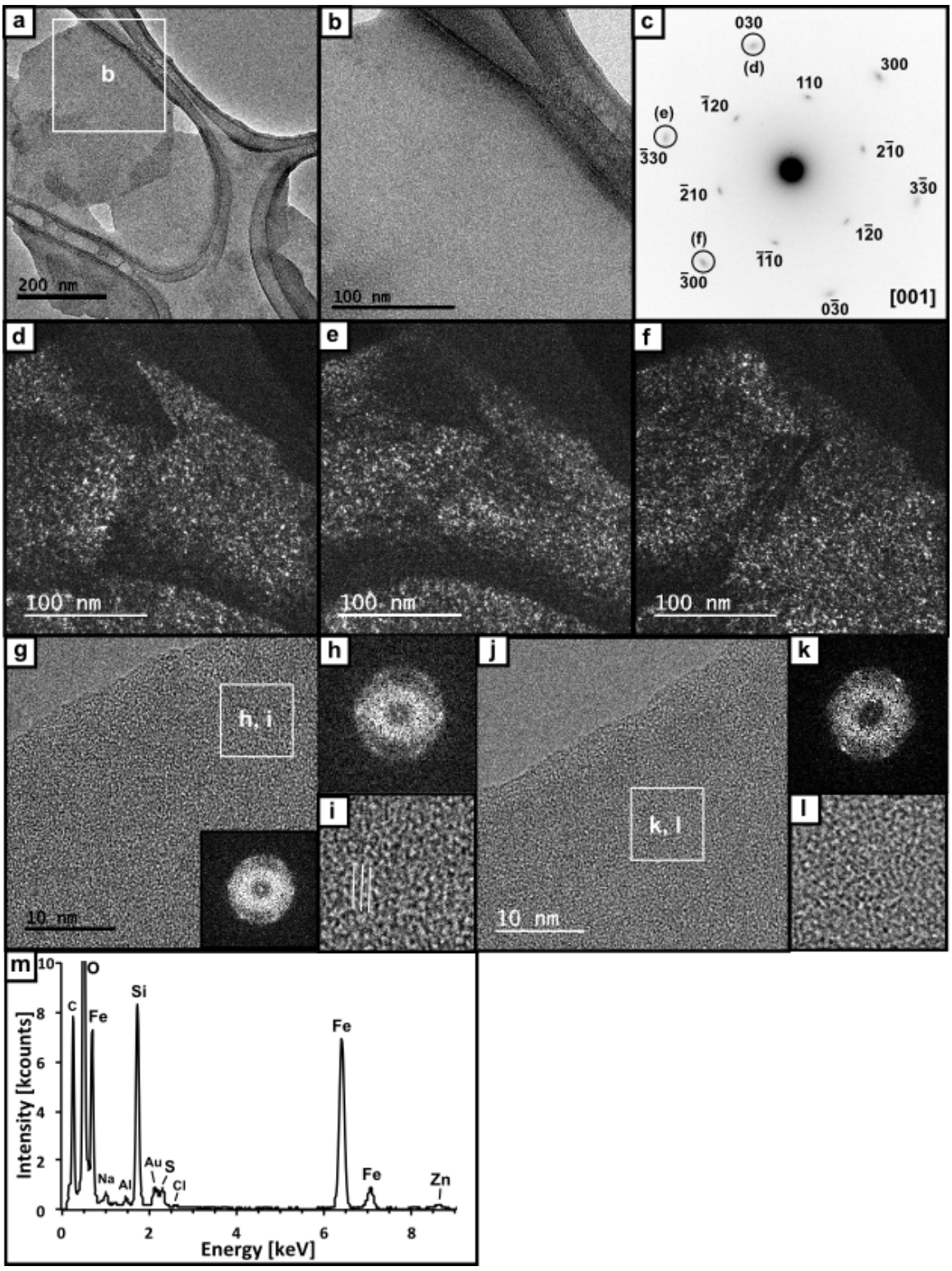

Figure 3.2. Pseudo-hexagonal green rust platelet from outflow water. (a) TEM image of an aggregate of platelets, (b) bright field image of the inset in (a), (c) SAED pattern of the same approximate area, indexed and the spots used for DF imaging are circled and labeled, (d)-(f) DF images of the same area as (b), (g) and (i) HR images showing small areas of lattice fringes, (h) FFT of (g) showing faint spots matching the SAED pattern, (j) EDS spectrum.

Green-rust pseudo-hexagonal platelets were also found in the sediment at the Ronneburg uranium mine drainage terrace site, shown here in Figure 3.3. Having been exposed to atmospheric oxygen more than the particles in the outflow site (Figure 3.2), these platelets may have oxidized to ferric green rust while keeping their basic morphology, but they still show characteristics very similar to the platelets found at the groundwater outflow site. Smaller aggregates of unidentified iron oxides were commonly found on the surface of the platelets (dark patches on the platelets in Figures 3.3a, b). SAED patterns of the sediment platelets (Figure 3.3c) can be indexed in the same way as platelets from the outflow, based on the green rust structure $P\bar{3}1m$ and [001] zone axis orientation, and the general particle size and morphology are also similar. DF imaging (Figures 3.3d-f) of particular hkl reflections (circled in Figure 3.3c) also clearly show bright areas a few nanometers in diameter, indicating that these are not coherent single crystals, similar to those seen in Figure 3.2. The iron oxide precipitates on the surface of the platelet (dark areas in Figure 3.3a) do not contribute to the primary hexagonal SAED pattern (Figure 3.3c) and do not light up during DF imaging using those particular reflections. HR-TEM shows a crystalline area with amorphous patches (Figures 3.3g, h) but not all areas look like this one. Similarly to the outflow platelets, FFTs from different areas of the particle are aligned but some areas of the particle are tilted with respect to each other (data not shown). S is only present in trace amounts and the Fe/S atomic ratio calculated from the EDS spectrum is 58.5. Also present in trace amounts are the metals Ni and Cu, not previously found on these types of particles at the Ronneburg site (Johnson et al. 2014). The Cu signal is not from the grid mesh, which is made of gold, nor the sample holder, which is made of Be.

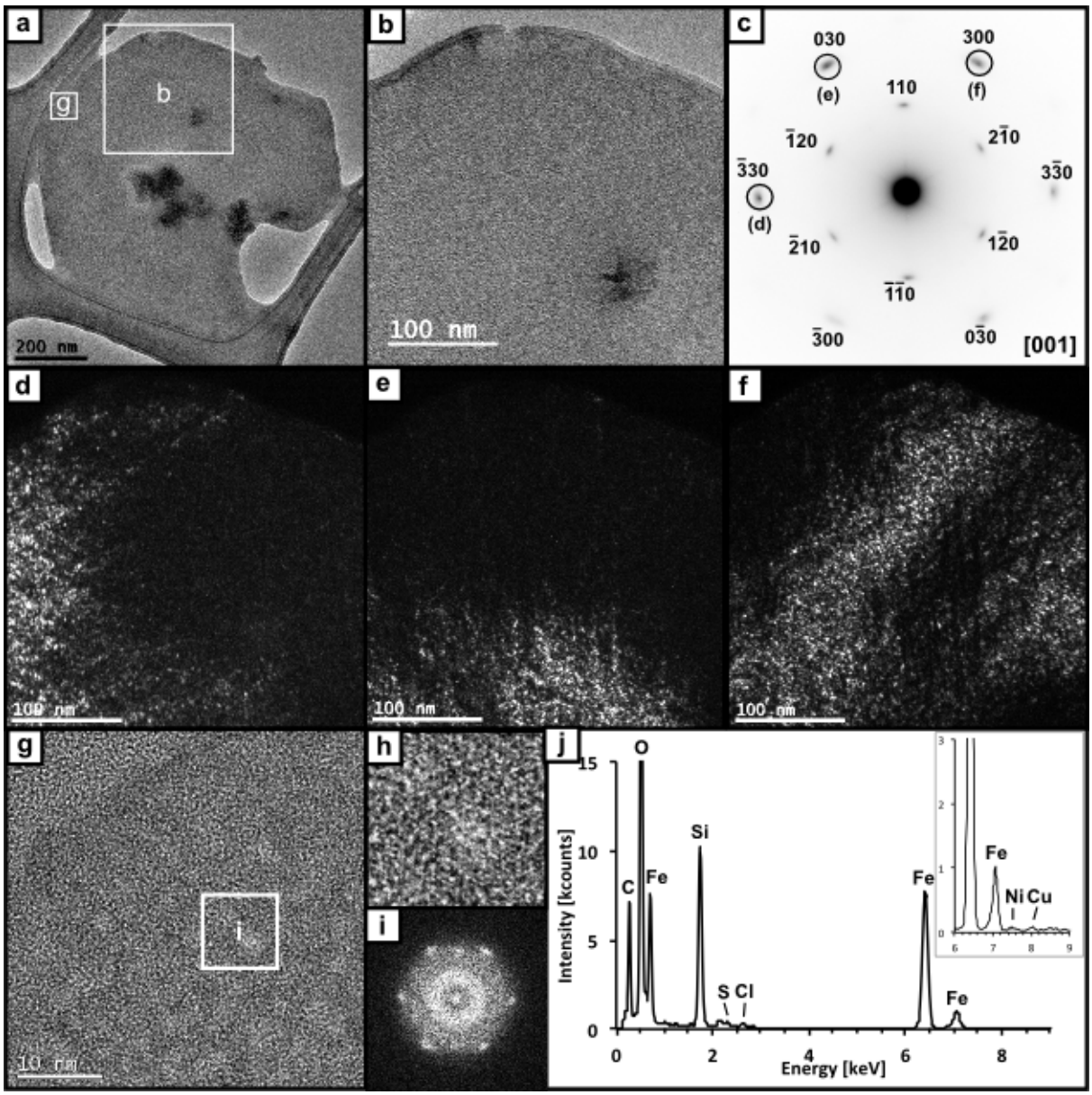

Figure 3.3. Pseudo-hexagonal natural green rust platelet from mine drainage terrace sediment. (a) TEM image of a platelet; (b) bright field image of the inset in (a); (c) inverted and indexed SAED pattern of the same approximate area, with the spots used for DF imaging circled and labeled; (d)-(f) DF images of the same area as (b); (g) HR image showing mosaic of lattice fringes and amorphous patches; (h) enlarged area of (g) showing the fringes more clearly; (i) FFT of (g) showing faint spots matching the SAED pattern with one set of additional spots; (j) EDS spectrum of whole platelet, with inset showing trace Ni and Cu.

3.4.2. Synthetic green rust

GR-SO_4 was successfully produced under a variety of conditions using four synthesis procedures (Table 3.1). Photos showing the color changes during synthesis reactions from

transparent yellow-orange to opaque dark olive green during titrations or fast addition of NaOH to initial Fe^{II}/Fe^{III} solutions (starting pH 1.5-3.0 depending on reagent brands used) are shown in Appendix B (Figure B.1). During titrations, when NaOH solution was added drop-wise with rapid mixing until a pH between 7 and 8, the sudden locally high pH caused dark precipitates to form that eventually dispersed or dissolved as the solution equilibrated at lower pH. Over months of time, the solutions equilibrated at a pH of approximately 5-6.

XRD data are shown for each synthesis in Figure 3.4 and Tables 3.2 and 3.3. Green rust was the predominant product, and only minor amounts of magnetite and/or amorphous silica are present. Material sampled either immediately or within 1-2 days exhibited the sharp diffraction peaks of GR-SO_4 (001), (002), and (003) planes, and they appeared to be very stable over many months when stored anoxically. The only exception to the stability was GR-D, possibly because the final product in the reaction vessel was in close proximity to an orange oxidized layer at the surface of the reaction solution. The crystallite sizes perpendicular to each hkl plane, calculated using the Scherrer equation with $K = 1$, are shown in Table 3.4. The averages (with standard deviations) over all sulfate green rust peaks in each sample were 24(9) (GR-A), 25(12) (GR-B), 28(7) nm (GR-C), and 18(5) nm (GR-D). The average crystallite sizes for just the 001, 002 and 003 peaks (corresponding approximately the particle thickness if it is only one crystallite thick) are 26(2) nm (GR-A), 26(2) nm (GR-B), 27(2) nm (GR-C), and 15(1) nm (GR-D).

In the following paragraphs, we will discuss the results from the nanoscale characterization of the four synthetic green rust products by analytical TEM. A comparison of crystallographic d-spacings measured using XRD, SAED and FFT is presented in Tables 3.2 and 3.3, and Fe/S atomic ratios calculated from EDS spectra are shown in Table 3.5.

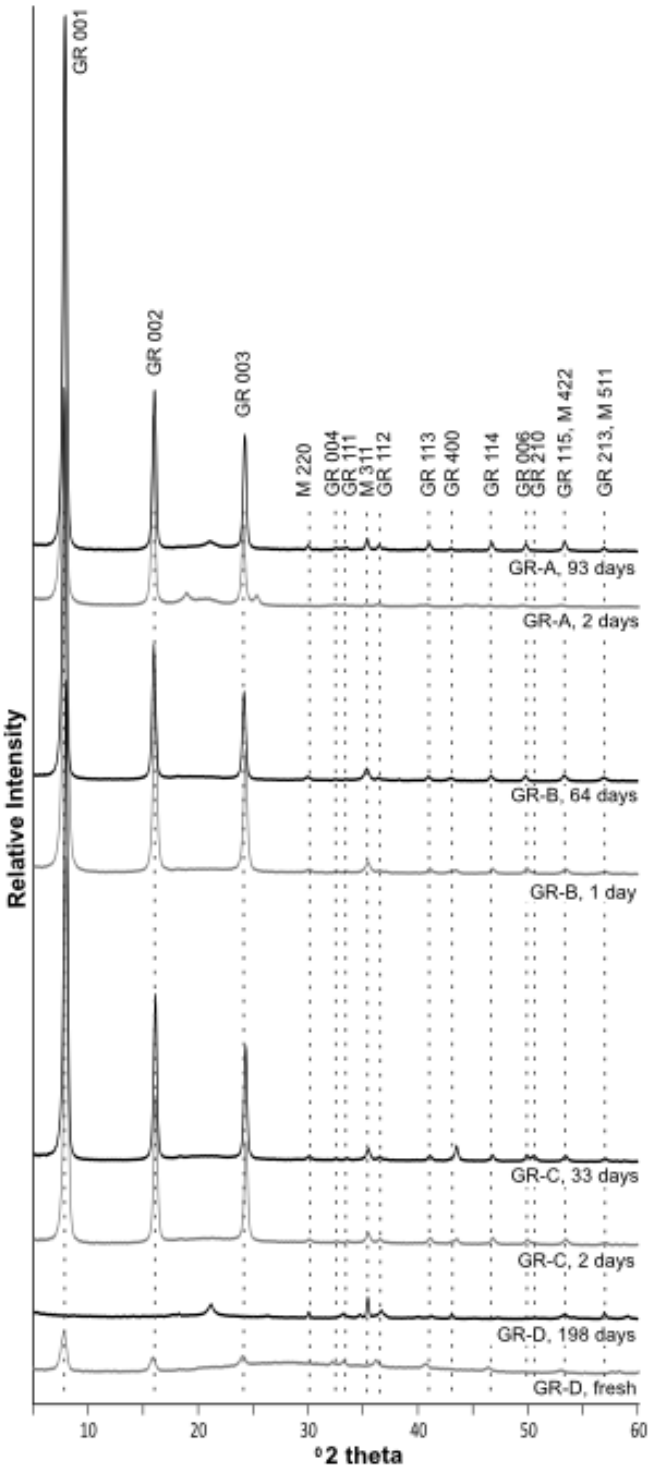

Figure 3.4. XRD spectra of syntheses (GR-A through GR-D, with number of days allowed to age) that produced primarily sulfate green rust II (GR) (Simon et al., 2003) and other minor phases (M = magnetite). Green rust and magnetite peaks are labeled with their crystallographic hkl plane(s).

Table 3.2. D-spacings for pseudo-hexagonal platelets found in outflow water and terrace sediment. Figure numbers are given for reference, but the d-spacing values (in Å) are representative of multiple areas. Grey highlighted cells represent the values that appear in a hexagonal pattern when the crystal is oriented along the [001] zone axis.

Reference Data[A]					Outflow water		Terrace Sediment	
					i.e. Figures 1-2		i.e. Figure 3	
GR-SO_4		GR-Na,SO_4		hematite	SAED	FFT	SAED	FFT
d	hkl	d	hkl	d	d	d	d	d
11.01	001	10.98	001					
		7.37						
5.51	002	5.49	002					
4.78	100	4.78	110					
					4.45			
4.39	101	4.38	111					
		3.91	021					
					3.86			
3.67	003	3.66	003	3.68	3.73			
					3.55			
					3.37-3.41			
2.91	103	3.07	120				2.94	
2.76, 2.75	110,004	2.75	030,004					
2.68	$\bar{1}\bar{1}1$	2.67	031	2.69				
		2.60	014		2.57-2.62			
2.47	$\bar{1}\bar{1}2$	2.46	032	2.51	2.45-2.52	2.54	2.49	2.52-2.61
2.34,2.39	201,200							
2.21	$\bar{1}\bar{1}$3,005	2.20	033,005	2.20			2.22	
2.00	105,203				2.29			
1.95	$\bar{1}\bar{1}$4	1.94	034		1.92			
1.81,1.84	210,006	1.80,1.83	140,006	1.84				
1.72	$\bar{1}\bar{1}$5	1.72	035	1.69				
1.60,1.62	300,213	1.59	330	1.60			1.61	
1.58	301	1.57	331,007					
1.53	302	1.53	332		1.54			1.51
1.49	107	1.49	117	1.49	1.48-1.5		1.48	
1.46	303	1.46	333	1.45	1.43	1.46	1.46	
		1.37	060,334					
		1.36	061	1.35				
		1.33	062		1.28			
		1.29	063,335				1.25	

[A]Reference data sources: GR-SO4 (Simon et al. 2003), GR-Na,SO_4 (Christiansen et al. 2009), hematite (ICDD PDF 00-001-1053, Hanawalt et al. 1938)

Table 3.3. D-spacing data (in Å) for synthetic green rust materials, from XRD, SAED and FFT. D-spacings are divided based on whether they were from sharp spots (nanoparticles) or broad spots (platelets). Grey highlighted cells represent the values that appear in a hexagonal pattern when the crystal is oriented along the [001] zone axis.

Reference Data[A]				GR-A pH8 + 2 days[B]				GR-B + 54 days			
				i.e. Figure 5				i.e. Figure 6			
GR-Na,SO_4		goethite	magnetite	XRD	SAED	SAED	FFT	XRD	SAED	SAED	FFT
d	hkl	d	d	d	d (np's)	d (platelets)		d	d (np's)	d (platelets)	
10.98	001			11.32				11.07			
7.37									7.52		
5.49	002	4.97		5.57				5.50			
4.78	110		4.85						4.78		
				4.68							
4.38	111			4.30							
		4.17									
3.91	021										
3.66	003			3.69				3.66			
				3.51							
							3.32[C]				
3.07	120		2.97					2.96	2.94		3.03
2.75	030,004			2.76				2.75			
2.67	031	2.69		2.69				2.68			
2.60	014		2.53	2.55		2.53	2.54-2.57	2.53	2.50	2.55	2.54-2.57
2.46	032	2.45,2.49		2.47				2.46			
			2.42						2.39		
2.20	033,005	2.19		2.21,2.24	2.21			2.20			
			2.10	2.00,2.04				2.08	2.08		
1.94	034			1.95	1.93			1.94	1.91	1.87	
1.80, 1.83	140, 006			1.83				1.81,1.83			
1.72	035		1.72	1.72	1.71			1.72	1.70		
1.59	330	1.66	1.62					1.61	1.59		
1.57	331,007	1.56		1.58				1.57			
1.53	332				1.53						
1.49	117		1.49			1.47				1.49	
1.46	333				1.44				1.46		
1.37	060,334		1.42								
1.36	061	1.36									
1.33	062								1.31		
1.29	063,335										

[A]Reference data sources: GR-Na,SO_4 (Christiansen et al. 2009), goethite (RRUFF #R050142), magnetite (ICDD PDF card# 00-019-0629, "Monograph 255" 1967).
[B]After sample reached pH 8, XRD data was from 2 days aged, while TEM data was taken from the fresh sample.
[C]Not a spot in the typical hexagonal pattern.

Table 3.3. D-spacings table, continued.

Reference Data[A]				GR-C + 2 days			GR-D		
				i.e. Figure 7			i.e. Figure 8		
GR-Na,SO4		goethite	magnetite	XRD	SAED	SAED	XRD	SAED	FFT
d	hkl	d	d	d	d (np's)	d (plate)	d	d (nanorods)	
10.98	001			11.05			11.16		10.0-10.4
7.37									
					6.02				
5.49	002	4.97		5.50			5.55		
4.78	110		4.85		4.81				4.70, 4.89
									4.53-4.63
4.38	111								
		4.17			4.15				
3.91	021								
								3.87	
3.66	003			3.66			3.69		
					3.54				
3.07	120		2.97	2.98	2.97		3.17		
2.75	030,004						2.77		
2.67	031	2.69		2.67			2.69	2.67	
2.60	014		2.53	2.53	2.53	2.53		2.51	2.54-2.57
2.46	032	2.45,2.49		2.46			2.48		
			2.42		2.41				2.35
2.20	033,005	2.19		2.20			2.21	2.19	2.20,2.25
			2.10	2.08	2.09				
1.94	034			1.95			1.96	1.88	
1.80,1.83	140,006			1.83	1.86				
1.72	035		1.72	1.71	1.71		1.72	1.69	
1.59	330	1.66	1.62	1.62	1.61		1.59		
1.57	331,007	1.56					1.58	1.57	
1.53	332						1.53		
1.49	117		1.49		1.48	1.47		1.48	
1.46	333							1.45	
1.37	060,334		1.42						
1.36	061	1.36							
1.33	062				1.31				
1.29	063,335								

[A]Reference data sources: GR-Na,SO_4 (Christiansen et al. 2009), goethite (RRUFF #R050142), magnetite (PDF card# 00-019-0629, "Monograph 255" 1967).

Table 3.4. Fe/S atomic ratios for different natural and synthetic particles, as determined by TEM-EDS.

Sample	Fe/S	Particle type
Outflow water	14	platelet
Terrace sediment	59	platelet
GR-A	4	platelet
GR-B	7	platelet
	142	nanomagnetite
GR-C	8	platelet & nanomagnetite
GR-D	56	nanorods

Synthesis GR-A primarily produced GR-SO_4 with a minor amorphous silica component, as shown by XRD in Figure 3.4. During the synthesis, the NaOH solution was titrated into the initial Fe^{II}-Fe^{III} solution under the conditions listed in Table 3.1. Samples for XRD were taken at different pHs during the titration, and while green rust was dominant at pH 7, at pH 7.5 and 8 another clay was present (matching the pattern for corrensite; data not shown). However, after aging the pH 8 sample for two days, the XRD pattern once again matched green rust. The explanation for this is not known, but it is mentioned here because the fresh pH 8 sample was used for further analysis and some green rust platelets were found. These pseudo-hexagonal platelets (Figures 3.5a, b), exhibited diffuse reflections in the SAED pattern (Figure 3.5c) that are identical (both in arrangement and d-spacing) to those of the natural green rust platelets. The sharper spots in the SAED pattern belong to the crystalline nanoparticles deposited on the surface of the platelets, as confirmed by DF imaging (Figure 3.5f). These crystalline nanoparticles are referred to as "np's" in Tables 3.2 and 3.3, to distinguish them from nanorods, because goethite nanorods (identified by SAED) were also present on the surface of the platelets. DF imaging revealed that the platelets are polycrystalline, which was confirmed by HR-TEM imaging where patches of crystalline and amorphous areas are visible. The area in Figures 3.5g, h, however, exhibits mostly uniform lattice fringes and the FFT pattern (Figure 3.5i) shows the

typical hexagonal spot pattern that matches the SAED pattern for this particle. The dark particle on the platelet surface does not diffract at this orientation. Compositionally, GR-A matches the theoretical GR-Na,SO_4 well with an Fe/S atomic ratio of 4.4 (4.5 for GR-Na,SO_4), and a Na peak. A significant Si peak is also present, and the reasons for this will be given in the discussion section.

GR-SO_4 was also the dominant product of synthesis GR-B, with minor amounts of magnetite and amorphous silica, and the sample was stable for many months (Figure 3.4). However, GR-B produced platelets that were distinctly different in morphology from GR-A (Figure 3.6). Instead of fairly regular hexagonal platelets, polygons of varying edge lengths and interior angles of 60° and/or 120° were also found, such as parallelograms and triangle-like hexagons (alternating long and short sides) (see Figure 3.6k). These platelets have rims that were thicker than the centers (as confirmed by SEM in Figure 3.6m). The platelet thickness is approximately 3-5 nm because the contrast difference between the particles and the underlying ultrathin (3-4 nm) carbon film is very small, even though the particle is crystalline and composed of heavier elements. Differences in diffraction contrast were also very helpful in order to understand the intriguing polycrystalline nature of these platelets, which have a dendritic pattern starting near the center of the particles and going outward towards the edges (best seen in Figure 3.6d). Diffraction contrast causes the crystalline areas to appear darker, even in the low magnification images. The dendritic features are composed of nanocrystallites that are aligned along short dendritic segments, but are slightly rotated with respect to each other between neighboring dendrite areas (Figure 3.7). DF imaging (Figures 3.6e,f) was used to confirm that the platelets are composed of nanocrystalline areas mixed with amorphous areas, and that areas that appear bright do correspond directly to the crystalline dendritic patterns observed in low

magnification and HR-TEM images. Both DF images were taken from the hkl reflections indicated by circles in the hexagonal SAED pattern in Figure 3.6c. The Fe/S atomic ratio of the thin platelets is 7, and as with GR-A platelets, there is a prominent Si peak.

The sharp diffraction spots in Figure 3.6c belong to the highly crystalline magnetite nanoparticles on the surface of the GR-SO_4 platelets. Aggregates of magnetite nanoparticles (individual particles ranging in size from a few nm to a few tens of nm in diameter) dominated the TEM grids and seemed much more prevalent than green rust platelets in syntheses GR-B and GR-C. These magnetite particles have uniform lattice fringes extending to their edges. Some have a hexagonal morphology, but a cube of magnetite in a [111] orientation can appear hexagonal. Differentiating green rust from individual magnetite particles using HR-TEM and FFT was problematic because their crystallographic planes have d-spacings that are too close to distinguish from each other, including around the characteristic reflection for magnetite at 4.8 Å. The XRD spectra for GR-B, as well as the other synthetic samples (Figure 3.4), consistently included very intense GR-SO_4 peaks and only small magnetite peaks, so sampling for this particular TEM grid preparation may have played a role in the observed dominance of the magnetite nanoparticles over the large platelets. The EDS Fe/S atomic ratio for the magnetite nanoparticles is 142 (there is only a trace amount of S), and there is only a small Si peak for these particles as compared to the platelets.

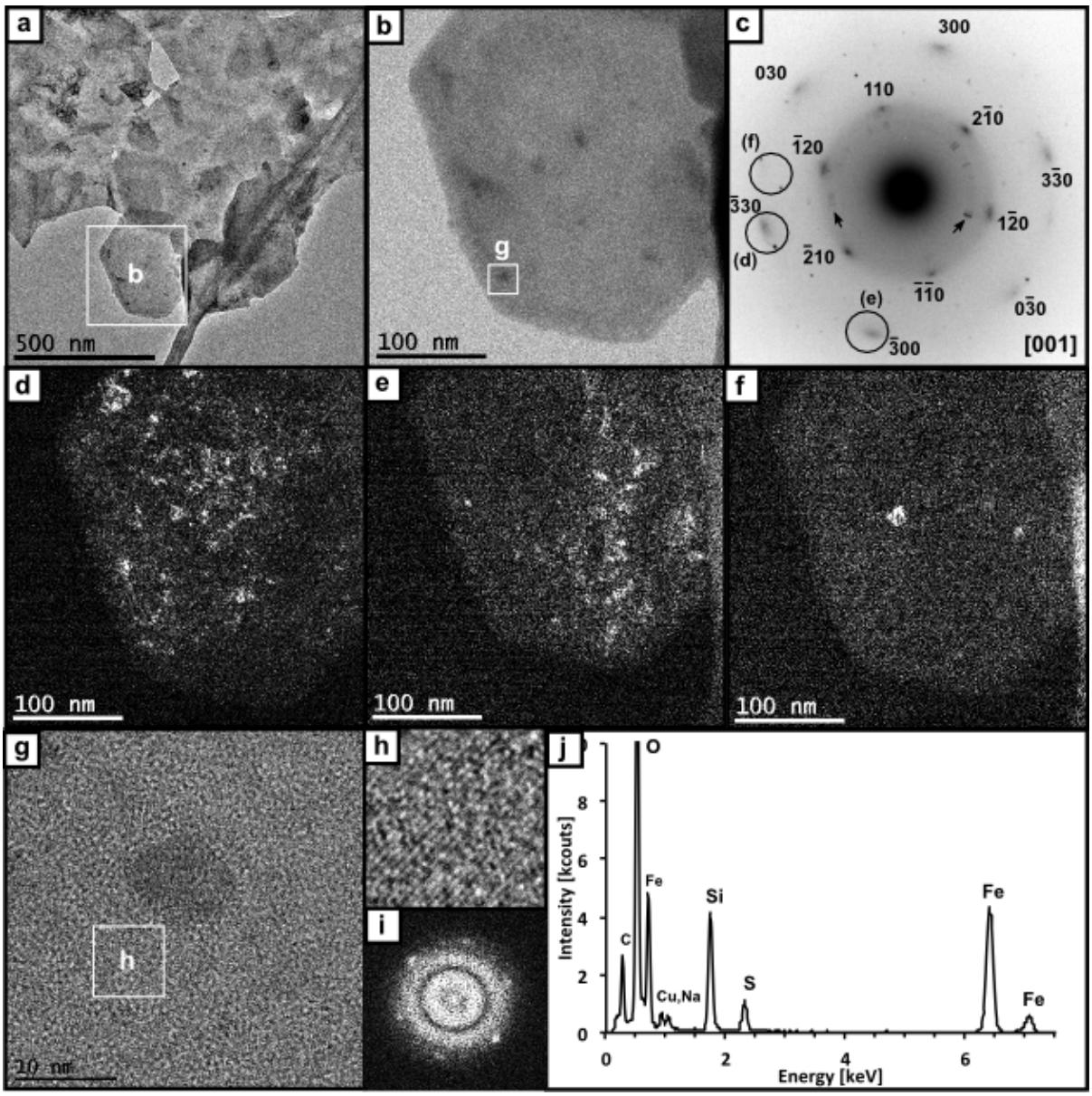

Figure 3.5. Pseudo-hexagonal platelet synthesized in GR-A and sampled immediately upon reaching pH 8. (a) TEM image of a platelet in an aggregate, (b) bright field image of the inset in (a), (c) inverted and indexed SAED pattern of the same approximate area, with the spots used for DF imaging circled and labeled, (d)-(f) DF images of the same area as (b), (g) and (h) HR images showing lattice fringes, (i) FFT of (g) showing a clear hexagonal spot pattern, (j) EDS spectrum. Arrows in (c) indicate an artifact ring (lines, not spots) from contamination on the C2 aperture.

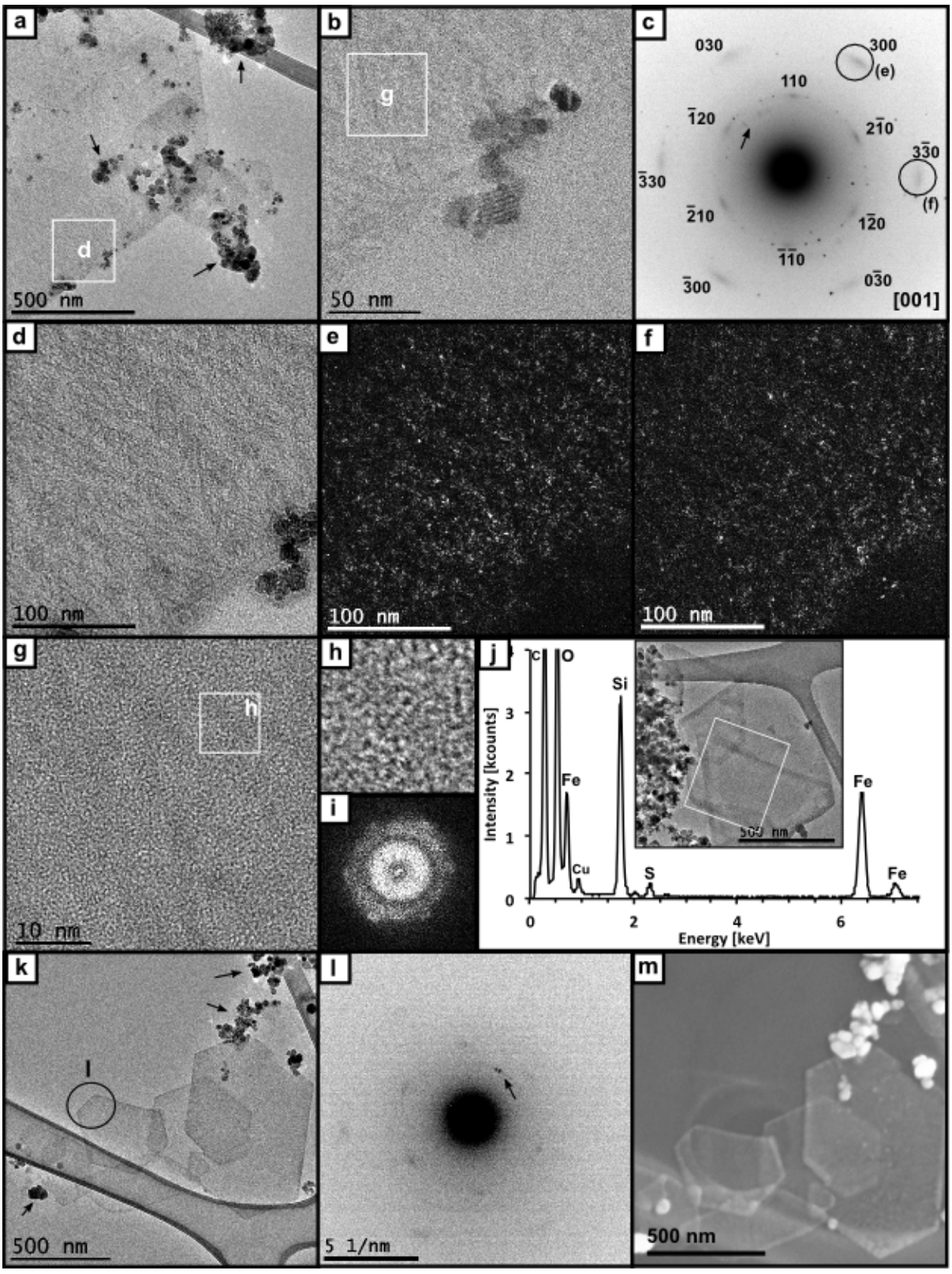

Figure 3.6. Pseudo-hexagonal green rust platelets from synthesis GR-B, aged 54 days. (a) TEM image of part of a platelet with nanoparticle aggregates on the surface; (b) medium magnification showing dendritic areas of

crystallinity more clearly; (c) inverted and indexed SAED pattern of the approximate area imaged in (a), with the spots used for DF imaging circled and labeled; (d) bright field image of the inset area in (a) and the same area used for DF imaging (e and f); (g) HR-TEM of the area in (b); (h) zoomed-in area of (g) to better show faint lattice fringes; (i) FFT of whole HR-TEM image in (g); (j) EDS spectrum of another area, shown in the inset; (k) a third area showing different platelet shapes; (l) inverted SAED pattern of the circled area in (k); (m) SEM image of (k) to show raised rims and interesting particle shape. Arrows in (c) and (i) indicate an artifact ring (lines, not spots) from contamination on the C2 aperture.

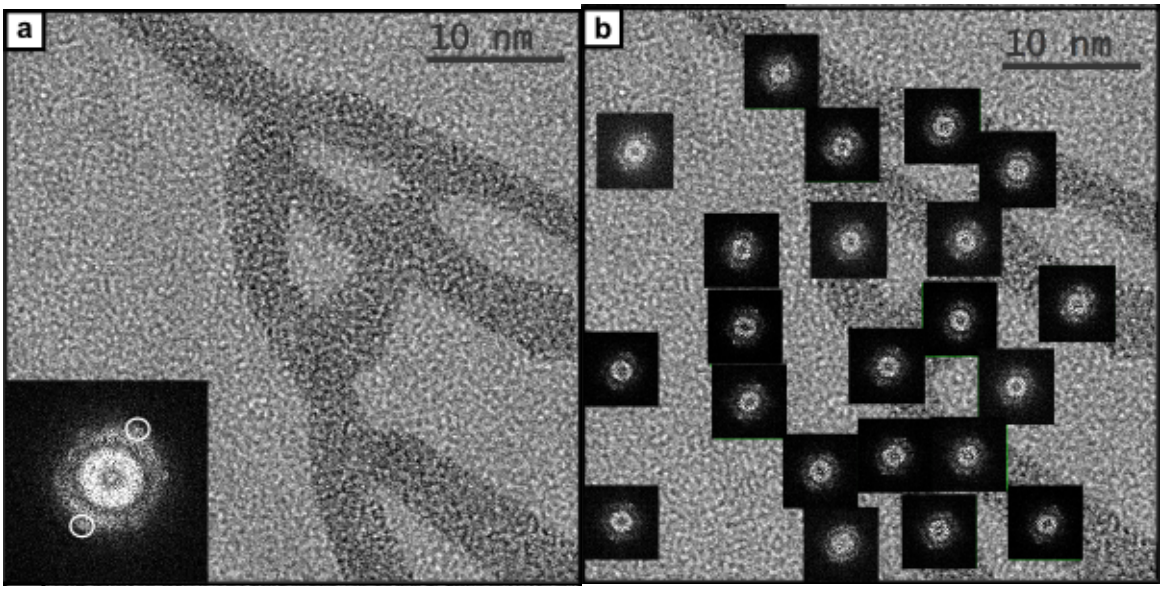

Figure 3.7. GR-B dendrite patterns shown in **Figure 3.6**g, with small-area FFTs along the crystalline dendrites. (a) Image highlighting one dendritic pattern (dark areas). The inset is the FFT of the whole image with the predominant pair of reflections is circled in white. (b) Map of FFT patterns on that same image, where each FFT only displays one or two pairs of the hexagonal pattern, some rotated slightly with respect to each other. FFT patterns along the same dendrite tend to match and align well.

Surprisingly, there was no obvious difference between the GR-B synthesis (performed under oxic conditions) and GR-C, a completely anoxic synthesis. Both syntheses had identical XRD patterns (Figure 3.4), and both had many aggregates of magnetite nanoparticles. In a sample of GR-C aged 80 days, platelets virtually identical to those in GR-B (aged 54 days) were observed with the same characteristics: various types of six-sided polygons, only a few nm in thickness, dendritic contrast patterns, and rims that were thicker than the center. Therefore, we infer that the presence of dissolved oxygen during the addition of NaOH is neither detrimental nor necessary. The products of both of these syntheses, stored anoxically, are very stable long-term.

Unlike the other syntheses described so far in this study and in the published literature, GR-D produced green rust particles of nanorod morphology, approximately 5-10 nm in diameter and a few tens of nm in length (Figure 3.8), with a Fe/S atomic ratio of 56. Nanorods are not currently a known morphology of sulfate green rust, which is typically found as thin pseudo-hexagonal platelets up to a few micrometers in diameter. The XRD spectrum of fresh GR-D clearly shows GR-SO_4, as well as an amorphous (iron oxide?) component, but SAED was not conclusive due to the lack of the GR-SO_4 (001) or (002) reflections. The unusual morphology was reason enough to get direct confirmation by HR-TEM that the nanorods were GR-SO_4 and not goethite, which has been previously reported as a GR-SO_4 precursor (Ahmed et al. 2010). Nanorods viewed from the side did not provide any characteristic d-spacing values to identify the structure, so we focused on the dark, diamond-shaped particles on the assumption that they were the cross-sectional view of the nanorods. Indeed, HR-TEM and corresponding FFT of one of those diamond-shaped particles exhibited the characteristic interlayer d-spacing of the (001) plane as shown in Figure 3.8d. More examples are shown in Figure B.3 in Appendix B. The FFT pattern in Figure 3.8e exactly matches the simulated electron diffraction pattern of sulfate green rust (structure identified by Simon et al. 2003) oriented on the [100] zone axis (Figure 3.8f). Moiré fringes from adjacent parallel planes were also considered, but ruled out by calculating the expected moiré fringe spacing *D* from the d-spacings of adjacent areas (*d*1, *d*2) using the equation $D = \frac{d1*d2}{(d1-d2)}$ (Edington 1975). The calculated *D* is 8.6 Å, while the d-spacings measured directly from the HR-TEM image and from the FFT pattern are 10.0-10.6 Å which are reasonably close (within error) to the diagnostic (001) spacing of green rust (d = 11 Å). D-spacings from the SAED of nanorod aggregates also support the conclusion that these particles

are not other iron (oxyhydr)oxide mineral phases such as goethite or magnetite, because characteristic reflections of those minerals are missing.

.

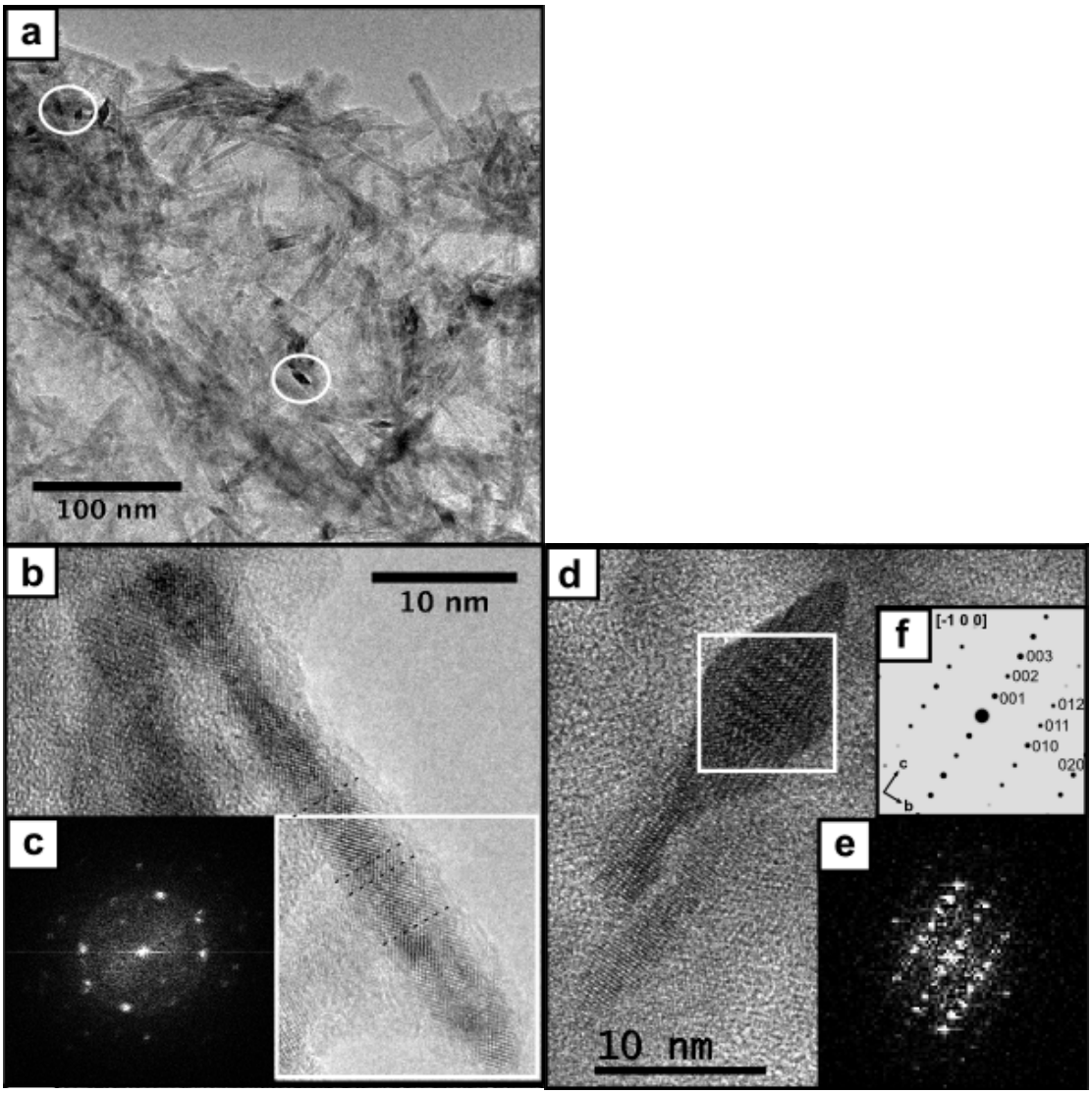

Figure 3.8. Nanorods of green rust produced in synthesis GR-D. (a) TEM image of an aggregate of nanorods with vertically-aligned rods visible as diamond shapes (circled in white); (b) HR-TEM image of a single nanorod, with possible twin interfaces indicated by the black dashed lines; (c) FFT of the area outlined in white in (b); (d) nano-rod on end exhibiting large lattice fringes; (e) FFT of area outlined in white in (d); (f) simulated diffraction pattern of sulfate green rust II (Simon et al. 2003) oriented along the $\bar{1}00$ zone axis exactly matches the FFT pattern.

3.5. Discussion

3.5.1. Morphology

Natural green rust minerals found in the outflow and sediment of Ronneburg mine drainage (Johnson et al. 2014, and this study) are typically pseudo-hexagonal platelets with rounded corners, likely in various stages of dissolution. Pseudo-hexagons are the characteristic morphology of green rust (Géhin et al. 2002; Skovbjerg et al. 2006; Trolard et al. 2007; Christiansen et al. 2009; Usman et al. 2012). An unexpected result of this research was the synthesis of three morphologically different sulfate green rusts: pseudo-hexagonal platelets, four- to six-sided polygonal platelets with interior angles of 60° and/or 120°, and nanorods. The pseudo-hexagons of synthesis GR-A look the most similar to the outflow and sediment green rust particles in the Ronneburg mine drainage. The polygons of GR-B (and GR-C, not shown) are quite variable, and have an even larger aspect ratio with thicknesses of approximately 3-5 nm and diameters of up to a few micrometers. GR-D produced nanorods, which are not a known morphology of green rust though there is no reason to believe that we will never find them in nature. It is quite common for minerals to exhibit a wide variety of morphologies when formed in nature and in the laboratory.

In order to produce these different morphologies, particularly the nanorods in GR-D, different synthesis conditions and reaction kinetics are likely important factors. For GR-D the Fe^{II}/Fe^{III} ratio was less than half of the stoichiometric ratio used for GR-B and GR-C, resulting in an excess of Fe^{III}, and the total Fe concentration was about 50% lower. The molar ratio of OH^-/Fe_{total} for GR-D was half of that for the other three syntheses. These ratios are thought to be the determining factor for which mineral phase forms (e.g. green rust, goethite, or magnetite) (Ruby et al. 2006). Kinetics determined by the rate of addition of base, either by slow titration over

many hours or merely dumped in all at once, may have also played a role in the determination of morphology. A more systematic study is necessary, and recommended, to understand which specific variable(s) are responsible for these morphological differences.

3.5.2. Polycrystallinity and coherency

In a coherent, textured, polycrystalline particle, the individual crystallites will be well aligned, while in an incoherent particle there are a significant amount of crystalline defects and misaligned crystallites. The broad, diffuse spots in the SAED patterns give the first clues that the crystallites may be slightly misaligned, though this broadening could also be due to the inherent strain and incoherency within nano-sized crystallites (Waychunas 2001).

The crystallite sizes calculated from the XRD peak broadening vary depending on the hkl plane. For example, GR-A and GR-B have a calculated crystallite size of 9 and 4 nm (respectively) perpendicular to the (111) plane, but a size of 24 nm perpendicular to the (001) plane. The bright spots on the DF images are only a few nanometers in diameter. If the crystallite shape is an elongated cylinder oriented perpendicular to the (001) plane, it would explain why the size calculated using the (111) plane is smaller and closer to the size of the bright spots in the DF images. However, it is difficult to explain why the crystallite sizes calculated from the (001) plane for GR-B and GR-C were 24 nm, while the particles appeared to only be a few nanometers thick (see Results section above). The crystallite sizes calculated using the Scherrer equation with the (001) plane of sulfate green rust in other studies were similar: 40 nm (Guilbaud et al. 2013), 36-47 nm (Ayala-Luis et al. 2008), and 5-30 nm depending on Fe^{II}/Fe^{III} and different synthesis methods (Mazeina et al. 2008).

The mosaics of brightly-imaged spots observed by DF-TEM provide conclusive evidence of the incoherent nature of the natural and synthetic green rust platelets. The crystallites must be

somewhat, although not exactly aligned, yet dark areas exist that represent other diffraction conditions. However, it is not immediately obvious why this can occur but at the same time have SAED patterns that do not show significant crystallite rotation. One explanation for this could be that some crystallites (i.e. GR-B in Figure 3.7b) are tilted such that only one or two pairs of diffraction spots are visible. Tilting perpendicular to a specific lattice plane by approximately 4-10° causes other diffraction spots to completely disappear from the SAED pattern, without new spots appearing. It is also possible that the low contrast areas are amorphous. It is unlikely that all the crystallites would be aligned if each were completely surrounded by amorphous material. Nevertheless, they could be connected by minute bridges that would be difficult to observe even in thin green rust sheets.

3.5.3. Implications for particle formation

Our understanding of mineral formation mechanisms is incomplete, and green rust is no exception, though there are some theories based on X-ray diffraction data. Guilbaud et al. (2013) proposed that GR-SO_4 growth was driven by Ostwald ripening, because the evolution of the crystallite size (calculated from the (001) plane peak broadening in the XRD spectra) matched the predicted curve for the Ostwald ripening model. Using wide angle X-ray scattering (WAXS) to perform an in situ, time-resolved analysis of GR-SO_4 formation using similar procedures as in this study, Ahmed et al. (2010) proposed that the interaction between aqueous Fe^{2+} and goethite above pH 7 resulted in Fe^{II}/Fe^{III} hydroxide sheets with the brucite structure, equivalent to the hydroxide layers of green rust. As hydrolysis of Fe^{2+} proceeds, the GR-SO_4 sheets will continue to grow along the (001) plane (Ahmed et al. 2010).

The existence of ~2 nm crystalline domains assembled in imperfect ways along the (001) plane, such as we see in the natural green rusts and synthetic GR-A, GR-B and GR-C described

in this study, is evidence that the building blocks for these platelets are nanoparticles. These nanoparticles may have formed from molecular clusters containing Fe^{II}, Fe^{III}, O, and possibly SO_4^{2-} and Si. Known polymers that can be stable in acidic conditions include polyferric sulfate and polyferric silicate sulfate (Zouboulis and Moussas 2008). Regardless of how the nanoparticles formed, and if they were part of other iron oxides such as schwertmannite or goethite prior to forming green rust (Ahmed et al. 2010), they ultimately aggregated in more or less oriented fashion. Different surface energies on each crystallographic face or part of the particle surface will affect how each crystallite orients itself with respect to its neighbors (Waychunas 2001). Presumably the layered double hydroxide structure of green rust does not allow many ways for those different faces to align.

In the case of GR-B (Figures 3.6, 3.7, and similarly GR-C), the dendrite patterns are composed of nanocrystallites that are oriented along single dendrite strands, with amorphous silica in-between the strands. Some areas are tilted with respect to the others (even if one pair of spots aligns well with those in other FFTs) (Figure 3.7). True dendritic crystal growth is not likely because dendrite formation typically involves rapid crystallization (atom-by-atom) and limited solution flow (Waychunas 2001). GR-B suggests a mechanism of aggregation into a dendrite-like pattern, not atom-by-atom growth. Comparing strands, the crystallites are slightly rotated with respect to each other. This could occur if, for example, two crystallites attached side-by-side, but there was a dislocation at the grain boundary due to incomplete hydrolysis of inward-facing –OHs or Si on the surface of the nanoparticle. That dislocation could have propagated and other crystalline strands may have branched off at dislocations and misalignments of crystallites. Nevertheless, it is difficult to explain why such a pattern would end up creating a hexagon shape.

The natural green rusts found in the outflow water and terrace sediment at the Ronneburg mine drainage site, and synthesis product GR-A, are also polycrystalline with crystallites only a few nanometers in size in directions along the width of the platelets. However, it is more difficult to explain the relationship between the crystallites because there is not a clear pattern, like the dendrite patterns in GR-B and GR-C. If we consider the platelet in the outflow water shown in Figure 3.2, there are distinct regions of many bright spots close to each other, and overall darker regions. When the DF images from the three chosen hkl reflections (030, $\bar{3}$30, $\bar{3}$00) are overlain, nearly the entire particle is covered in bright spots although there are still some small dark areas in-between. Because some spots are bright in only one or two DF images, and some in all three, we can infer that this particle is composed of crystallites that are tilted (but not rotated more than a couple of degrees) with respect to each other. There are amorphous areas as well. The green rust platelet from the terrace sediment shown in Figure 3.3 similarly has large regions that appear bright when a particular hkl reflection is chosen. However, these regions are more distinct than for the outflow platelet and few spots appear bright in more than one DF image. This could mean that larger sections of the particle, many tens of nanometers in size, are tilted with respect to each other, and the crystallites within each region are more closely aligned (the platelet is not flat). Again, there are still dark areas between the bright spots that could be amorphous material.

The features we see in both the synthetic and natural green rust platelets cannot be explained by classical crystal growth mechanisms. Instead, non-classical growth mechanisms rely on building blocks of molecules, clusters, and nanoparticles to aggregate in crystallographically-compatible ways to form larger particles that may diffract as single crystals but contain grain boundaries and defects. Oriented aggregation is an example of this, with nanoparticle building blocks such as ferrihydrite forming goethite nanorods (Banfield et al. 2000;

Penn et al. 2006), and hematite nanoparticles stabilized by acetate ligands forming two-dimensional hematite platelets (Cai et al. 2014). In an even more complex variation, often found in biomineralization, building blocks of inorganic material can assemble with organic or inorganic polymers in oriented ways to form mesocrystals, which diffract like single crystals but have complex domains (Cölfen and Mann 2003; Cölfen and Antonietti 2005). Nacre, a calcium carbonate mesocrystal structure produced by bivalves, has been shown by DF imaging to be composed of nano-domains of aragonite that are oriented in the same direction, despite being surrounded by a contiguous organic matrix (Rousseau 2011). Even though oriented aggregation is a possible formation mechanism for the green rusts in this study, particle formation here may be more likely a combination of oriented aggregation and atom-by-atom coarsening (Xue et al. 2014). Also known as Ostwald ripening, atom-by-atom coarsening is particle growth by the addition of individual atoms, when larger particles grow at the expense of smaller ones (Ostwald 1897; Banfield and Zhang 2001).

Although the platelets from the outflow water in Figure 3.1 were not imaged using dark-field microscopy, the HR-TEM images show features that are different than the other natural green rust platelets in Figures 3.2 and 3.3, as well as the synthetic green rusts. FFT patterns calculated from smaller regions of the image are well aligned with each other, and parallel lattice fringes are clearly visible throughout the image, even through the light-colored patches. Therefore, this particle exhibits more coherency than the others.

3.5.4. Silica association with green rust

Silicon commonly associates with iron oxides in natural systems. For example, amorphous silica was found intimately associated with schwertmannite nanoneedles in a mine drainage system (French et al. 2012) and on ferrihydrite precipitates of Fe-bearing spring waters

(Carlson and Schwertmann 1981). The poorly-crystalline iron oxide particles, found in mine drainage water and sediments of the Ronneburg uranium described in our previous study (Johnson et al. 2014) were also associated with Si, and the green rust platelets were no exception. However, the concentration of Si (0.4 mM) in the drainage water (Johnson et al. 2014) was under-saturated with respect to amorphous silica. Although the concentration that we observed is within the normal range of dissolved Si in natural waters (0.1-1.2 mM) (Burton and Johnston 2012), one might estimate this it is unlikely that Si would precipitate or sorb to the iron oxide particles. However, it has been shown numerous times that iron oxides have a high affinity for silicate sorption in natural waters (e.g. Carlson and Schwertmann 1981, 1987; Sun et al. 2012) and soils (e.g. Childs 1992). Silicic acid (H_4SiO_4) in solution can sorb to ferrihydrite and polymerize (Swedlund et al. 2009), resulting in solid-phase Si/Fe ratios comparable to those found by TEM EDS in this study. However, the affinity of silicate for other ferric minerals can vary widely. For example, the solid phase Si/Fe ratios for goethite following the sorption of H_4SiO_4 (Hiemstra et al. 2007) were an order of magnitude lower than for ferrihydrite in the Swedlund et al. (2009) study.

We were unable to remove Si entirely from our synthetic system and noticed a high affinity of the synthetic green rust for Si, similar to the natural green rust particles. Si/Fe ratios of nanorods and magnetite nanoparticles were much less than for synthetic green rust platelets. The synthetic green rusts concentrated the trace amounts of Si that were originally present in the starting materials and solutions. This was determined by comparing the Si/Fe ratios of the original solution (determined by inductively-coupled plasma atomic emission spectroscopy, ICP-AES), and EDS spectra of the lacey carbon film of the TEM grid and green rust platelets (data not shown). The Si/Fe ratios for the green rust platelets were much higher than for the lacey

carbon and in solution. Ultimately, we determined that our anoxic water (boiled and stored in Pyrex glass containers) was the most likely source of silica contamination because that boiled water applied to a TEM grid did give a Si peak using EDS, but no Si was present on a grid prepared with water that had only been stored in plastic. Using Si-free synthesis vessels and tubing did not solve the problem. Another piece of evidence for the presence of significant amounts of Si associated with the platelets are the very broad and weak diffraction peaks (15-25 °2Θ, centered around 20°), which are indicative of amorphous silica. These were seen in all XRD spectra of green rust syntheses, with the exception of GR-D. These peaks are not visible in Figure 3.4, but are clear when the diffraction patterns are enlarged.

Since Si was present in the starting solution (at concentrations of 1-2 μM), it could potentially sorb onto the crystallites during or after the aggregation process. There was no evidence in the synthetic green rusts of the surface "patchiness" seen in the natural green rust platelets in Figure 3.1 and Johnson et al. (2014).

3.5.5. Comparison to other synthetic green rusts

The sulfate green rusts produced in this study show differences to those in the published literature, at least visually, particularly for GR-B which was synthesized with the same method as Ruby et al. (2003). Synthetic green rust products, whether abiotic or biotic, usually have fairly sharp corners and straight edges, though the size and morphology varies widely even within a sample (Ruby et al. 2003; Skovbjerg et al. 2006; Ahmed et al. 2010; Usman et al. 2012). GR-B platelets with rims did look strikingly similar to green rust in the process of reacting with Cr^{VI} (Skovbjerg et al. 2006). In that study, not only were thicker rims visible, but the center of the platelet seemed to dissolve away with the formation of secondary products (goethite). Dissolution of the inner platelet, leaving the rims basically intact, was also observed in the GR-B

sample aged for 90 days (Appendix B Figure B.4). However, in the case of green rust reacting with Cr^{VI}, the starting material was well-faceted, smooth platelets (Skovbjerg et al. 2006), unlike what we observed in GR-B. Structurally, it was difficult to compare d-spacings to published work because that data is not often reported in conjunction with the SAED pattern, though the typical hexagonal spot pattern (oriented down the [001] axis) was consistently present.

3.6. Implications

As we show in this study, both natural and synthetic green rust minerals exhibit an extraordinary complexity in structure and composition on the nanoscale. Detailed TEM analyses reveal the polycrystalline nature of these nanometers-thin platelets, filled with defects that result in many reactive sites and, likely, atomically rough surfaces. These properties, combined with the presence of both Fe^{II} and Fe^{III} in the layered-double-hydroxide structure and nanoscale thinness that results in a platelet having an exceptionally high surface to volume ratio, help explain why this elusive phase has a remarkable potential for participating in the reactions of environmental and industrial systems.

In particular, we found that green rust platelets can contain trace amounts of Zn, Ni and Cu, which were prevalent in the outflowing waters discharging directly from the underground mine workings at the former Ronneburg uranium mine (Johnson et al. 2014 and this study). Carbonate green rust formation from ferrihydrite has indirectly been found to enhance Ni uptake in a ferruginous lake (Zegeye et al. 2012), but we believe this is the only other study to date that has reported trace metal association with green rust from a natural system. In addition to metals, green rust appears to have a strong affinity for Si, which is also commonly present in ground- and surface waters. Si that interacts with the particle during formation or during its lifetime could impact green rust reactivity in ways that are not fully understood. It would be beneficial to seek

out and carefully sample, preserve, and characterize by analytical TEM green rust minerals in a variety of environments.

When performing laboratory experiments using mineral nanoparticles and extrapolating the results to environmental relevance, there are many steps one can take to make experimental systems more representative in their complexity. In addition to using natural matrices (i.e. natural waters, soil or sediments) and environmentally-relevant concentrations of reactants (Vignati et al. 2007), it is helpful to synthesize materials that have a similar morphology, nanoscale structure, and composition as the natural materials of interest. In this particular study, we show that some of our synthetic sulfate green rust products did have a remarkable similarity to the green rusts found in the mine drainage water and sediment of our field site, including polycrystalline, incoherent structures and association with silica. We suggest that these attributes will make a significant difference in their reactivity with pollutants and during biogeochemical iron cycling.

Careful anoxic sample collection, preparation, and storage should someday allow us to finally understand the true extent and importance of green rust phases and their variations in nature. We anticipate that in the future, green rust will be shown to be widespread and highly active in a wide variety of subsurface systems.

3.7. Acknowledgements

Carol A. Johnson was financially supported by the National Science Foundation (NSF) Integrative Graduate Education and Research Traineeship program (grant DGE-0504196), and the NSF and the Environmental Protection Agency (EPA) through the Center for the Environmental Implications of NanoTechnology (CEINT) (NSF Cooperative Agreement EF-0830093). The Institute for Critical Technology and Applied Science (ICTAS) Nanoscale

Characterization and Fabrication Laboratory provided access to and technical support for the electron microscopes. Chris Winkler was particularly helpful in this regard. We also thank Gina Freyer and Maria Fabisch (Friedrich Schiller University Jena, Germany) for collaboration on the fieldwork and broader project, and J. Donald Rimstidt (Virginia Tech) for discussions and feedback on this manuscript.

3.8. References

Ahmed, I.A.M., Benning, L.G., Kakonyi, G., Sumoondur, A.D., Terrill, N.J., and Shaw, S. (2010) Formation of green rust sulfate: A combined in situ time-resolved X-ray scattering and electrochemical study. Langmuir, 26, 6593–6603.

Ayala-Luis, K.B., Koch, C.B., and Hansen, H.C.B. (2008) The standard Gibbs energy of formation of Fe(II)Fe(III) hydroxide sulfate green rust. Clays and Clay Minerals, 56, 633–644.

Ayala-Luis, K.B., Koch, C.B., and Hansen, H.C.B. (2010) Intercalation of linear C9–C16 carboxylates in layered Fe^{II}–Fe^{III}-hydroxides (green rust) via ion exchange. Applied Clay Science, 48, 334–341.

Banfield, J.F., and Zhang, H. (2001) Nanoparticles in the environment. In J.F. Banfield and A. Navrotsky, Eds., Nanoparticles and the Environment Vol. 44, pp. 1–58. Mineralogical Society of America, Chantilly, Virginia.

Banfield, J.F., Welch, S.A., Zhang, H., Ebert, T.T., and Penn, R.L. (2000) Aggregation-based crystal growth and microstructure development in natural iron oxyhydroxide biomineralization products. Science, 289, 751–754.

Bearcock, J.M., Perkins, W.T., Dinelli, E., and Wade, S.C. (2006) Fe(II)/Fe(III) "green rust" developed within ochreous coal mine drainage sediment in South Wales, UK. Mineralogical Magazine, 70, 731–741.

Burton, E.D., and Johnston, S.G. (2012) Impact of silica on the reductive transformation of schwertmannite and the mobilization of arsenic. Geochimica et Cosmochimica Acta, 96, 134–153.

Cai, J., Chen, S., Ji, M., Hu, J., Ma, Y., and Qi, L. (2014) Organic additive-free synthesis of mesocrystalline hematite nanoplates via two-dimensional oriented attachment. CrystEngComm, 16, 1553–1559.

Caraballo, M.A., Michel, F.M., and Hochella Jr., M.F. (n.d.) The rapid expansion of environmental mineralogy in unconventional ways: Beyond the accepted definition of a mineral, the latest technology, and using nature as our guide. American Mineralogist.

Carlson, L., and Schwertmann, U. (1981) Natural ferrihydrites in surface deposits from Finland and their association with silica. Geochimica et Cosmochimica Acta, 45, 421–429.

——— (1987) Iron and manganese oxides in Finnish ground water treatment plants. Water Research, 21, 165–170.

Childs, C.W. (1992) Ferrihydrite: A review of structure, properties and occurrence in relation to soils. Zeitschrift für Pflanzenernährung und Bodenkunde, 155, 441–448.

Christiansen, B.C., Balic-Zunic, T., Petit, P.-O., Frandsen, C., Mørup, S., Geckeis, H., Katerinopoulou, A., and Stipp, S.L.S. (2009) Composition and structure of an iron-bearing, layered double hydroxide (LDH) – Green rust sodium sulphate. Geochimica et Cosmochimica Acta, 73, 3579–3592.

Christiansen, B.C., Balic-Zunic, T., Dideriksen, K., and Stipp, S.L.S. (2009) Identification of green rust in groundwater. Environmental Science & Technology, 43, 3436–3441.

Cölfen, H., and Antonietti, M. (2005) Mesocrystals: Inorganic superstructures made by highly parallel crystallization and controlled alignment. Angewandte Chemie, 44, 5576–91.

Cölfen, H., and Mann, S. (2003) Higher-order organization by mesoscale self-assembly and transformation of hybrid nanostructures. Angewandte Chemie (International ed. in English), 42, 2350–65.

Dong, H., and Lu, A. (2012) Mineral-microbe interactions and implications for remediation. Elements, 8, 95–100.

Edington, J.W. (1975) Practical Electron Microscopy in Materials Science. Monograph 3: Interpretation of Transmission Electron Micrographs. MacMillan Press, Ltd, London.

Erbs, M., Hansen, H.C.B., and Olsen, C.E. (1999) Reductive dechlorination of carbon tetrachloride using iron(II) iron(III) hydroxide sulfate (green rust). Environmental Science & Technology, 33, 307–311.

French, R.A., Caraballo, M.A., Kim, B., Rimstidt, J.D., Murayama, M., and Hochella Jr, M.F. (2012) The enigmatic iron oxyhydroxysulfate nanomineral schwertmannite: Morphology, structure, and composition. American Mineralogist, 97, 1469–1482.

Géhin, A., Ruby, C., Abdelmoula, M., Benali, O., Ghanbaja, J., Refait, P., and Génin, J.-M.R. (2002) Synthesis of Fe(II-III) hydroxysulphate green rust by coprecipitation. Solid State Sciences, 4, 61–66.

Guilbaud, R., White, M.L., and Poulton, S.W. (2013) Surface charge and growth of sulphate and carbonate green rust in aqueous media. Geochimica et Cosmochimica Acta, 108, 141–153.

Han, Y.-S., Hyun, S.P., Jeong, H.Y., and Hayes, K.F. (2012) Kinetic study of cis-dichloroethylene (cis-DCE) and vinyl chloride (VC) dechlorination using green rusts formed under varying conditions. Water Research, 46, 6339–6350.

Hanawalt, J.D., Rinn, H.W., and Frevel, L.K. (1938) Chemical analysis by X-ray diffraction -- Classification and use of X-ray diffraction patterns. Industrial & Engineering Chemistry, Analytical Edition, 10, 457–512.

Hiemstra, T., Barnett, M.O., and van Riemsdijk, W.H. (2007) Interaction of silicic acid with goethite. Journal of Colloid and Interface Science, 310, 8–17.

Hochella Jr, M.F., Aruguete, D., and Kim, B. (2012) Naturally occurring inorganic nanoparticles: General assessment and a global budget for one of Earth's last unexplored major geochemical components. In A.S. Barnard and H. Guo, Eds., Nature's Nanostructures pp. 1–31. Pan Stanford Pte Ltd.

Johnson, C.A., Freyer, G., Fabisch, M., Caraballo, M.A., Küsel, K., and Hochella Jr., M.F. (2014) Observations and assessment of iron oxide and green rust nanoparticles in metal-polluted mine drainage within a steep redox gradient. Environmental Chemistry, 11, 377-391.

Jönsson, J., and Sherman, D.M. (2008) Sorption of As(III) and As(V) to siderite, green rust (fougerite) and magnetite: Implications for arsenic release in anoxic groundwaters. Chemical Geology, 255, 173–181.

Jorand, F.P.A., Sergent, A.-S., Remy, P.-P., Bihannic, I., Ghanbaja, J., Lartiges, B., Hanna, K., and Zegeye, A. (2013) Contribution of anionic vs. neutral polymers to the formation of green rust 1 from γ-FeOOH bioreduction. Geomicrobiology Journal, 30, 600–615.

Klug, H.P., and Alexander, L.E. (1974) X-Ray Diffraction Procedures for Polycrystalline and Amorphous Materials, 2nd ed. pp. 618–708. John Wiley & Sons, New York.

Kukkadapu, R.K., Zachara, J.M., Fredrickson, J.K., and Kennedy, D.W. (2004) Biotransformation of two-line silica-ferrihydrite by a dissimilatory Fe(III)-reducing bacterium: Formation of carbonate green rust in the presence of phosphate. Geochimica et Cosmochimica Acta, 68, 2799–2814.

Lavina, B., Dera, P., and Downs, R.T. (2014) Modern X-ray diffraction methods in mineralogy and geosciences. In G.S. Henderson, D.R. Neuville, and R.T. Downs, Eds., Spectroscopic Methods in Mineralogy and Materials Science Vol. 78, pp. 1–31. Reviews in Mineralogy and Geochemistry, Mineralogical Society of America, Chantilly, Virginia.

Mazeina, L., Navrotsky, A., and Dyar, D. (2008) Enthalpy of formation of sulfate green rusts. Geochimica et Cosmochimica Acta, 72, 1143–1153.

Mills, S.J., Christy, A.G., Génin, J.-M.R., Kameda, T., and Colombo, F. (2012) Nomenclature of the hydrotalcite supergroup: Natural layered double hydroxides. Mineralogical Magazine, 76, 1289–1336.

Monograph 255 (1967). U.S. National Bureau of Standards.

O'Loughlin, E.J., Kelly, S.D., Kemner, K.M., Csencsits, R., and Cook, R.E. (2003) Reduction of Ag(I), Au(III), Cu(II), and Hg(II) by Fe(II)/Fe(III) hydroxysulfate green rust. Chemosphere, 53, 437–446.

O'Loughlin, E.J., Larese-Casanova, P., Scherer, M., and Cook, R. (2007) Green rust formation from the bioreduction of γ –FeOOH (lepidocrocite): Comparison of several Shewanella species. Geomicrobiology Journal, 24, 211–230.

Ona-Nguema, G., Abdelmoula, M., Jorand, F., Benali, O., Géhin, A., Block, J.-C., and Génin, J.-M.R. (2002) Iron(II,III) hydroxycarbonate green rust formation and stabilization from lepidocrocite bioreduction. Environmental Science & Technology, 36, 16–20.

Ostwald, W. (1897) Studien ueber die Bildung und Umwandlung fester Koerper. Zeitschrift fuer Physikalische Chemie, 22, 289–330.

Parmar, N., and Beveridge, T.J. (2001) Formation of green rust and immobilization of nickel in response to bacterial reduction of hydrous ferric oxide. Geomicrobiology Journal, 18, 375–385.

Penn, R.L., Erbs, J., and Gulliver, D. (2006) Controlled growth of alpha-FeOOH nanorods by exploiting- oriented aggregation. Journal of Crystal Growth, 293, 1–4.

Raiswell, R. (2011) Iron transport from the continents to the open ocean: The aging-rejuvenation cycle. Elements, 7, 101–106.

Rennert, T., Eusterhues, K., De Andrade, V., and Totsche, K.U. (2012) Iron species in soils on a mofette site studied by Fe K-edge X-ray absorption near-edge spectroscopy. Chemical Geology, 332-333, 116–123.

Rousseau, M. (2011) Nacre, a natural biomaterial. In R. Pignatello, Ed., Biomaterials Applications for Nanomedicine pp. 281–298. InTech.

Ruby, C., Géhin, A., Abdelmoula, M., Génin, J.-M.R., and Jolivet, J.-P. (2003) Coprecipitation of Fe(II) and Fe(III) cations in sulphated aqueous medium and formation of hydroxysulphate green rust. Solid State Sciences, 5, 1055–1062.

Ruby, C., Aïssa, R., Géhin, A., Cortot, J., Abdelmoula, M., and Génin, J.-M. (2006) Green rusts synthesis by coprecipitation of FeII–FeIII ions and mass-balance diagram. Comptes Rendus Geoscience, 338, 420–432.

Scherrer, P. (1918) Bestimmung der Größe und der inneren Struktur von Kolloidteilchen mittels Röntgenstrahlen. Nachrichten von der Gesellschaft der Wissenschaften zu Göttingen, Mathematisch-Physikalische Klasse, 98–100.

Simon, L., François, M., Refait, P., Renaudin, G., Lelaurain, M., and Génin, J.-M.R. (2003) Structure of the Fe(II-III) layered double hydroxysulphate green rust two from Rietveld analysis. Solid State Sciences, 5, 327–334.

Skovbjerg, L.L., Stipp, S.L.S., Utsunomiya, S., and Ewing, R.C. (2006) The mechanisms of reduction of hexavalent chromium by green rust sodium sulphate: Formation of Cr-goethite. Geochimica et Cosmochimica Acta, 70, 3582–3592.

Stampfl, P.P. (1969) Ein basisches Eisen-II-III-Karbonat in Rost. Corrosion Science, 9, 185–187.

Sun, Z., Zhou, H., Glasby, G.P., Yang, Q., Yin, X., and Li, J. (2012) Mineralogical characterization and formation of Fe-Si oxyhydroxide deposits from modern seafloor hydrothermal vents. American Mineralogist, 98, 85–97.

Swedlund, P.J., Miskelly, G.M., and McQuillan, a. J. (2009) An attenuated total reflectance IR study of silicic acid adsorbed onto a ferric oxyhydroxide surface. Geochimica et Cosmochimica Acta, 73, 4199–4214.

Swietlik, J., Raczyk-Stanisławiak, U., Piszora, P., and Nawrocki, J. (2012) Corrosion in drinking water pipes: The importance of green rusts. Water Research, 46, 1–10.

Taylor, K.G., and Konhauser, K.O. (2011) Iron in Earth surface systems: A major player in chemical and biological Processes. Elements, 7, 83–88.

Trolard, F., and Bourrié, G. (2012) Fougerite a natural layered double hydroxide in gley soil: habitus, structure, and some properties. In M. Valaskova and G.S. Martynkova, Eds., Clay Minerals in Nature - Their Characterization, Modification, and Application pp. 171–188. InTech.

Trolard, F., Genin, J.-M., Abdelmoula, M., Bourrie, G., Humbert, B., and Herbillion, A. (1997) Identification of a green rust mineral in a reductomorphic soil by Moessbauer and Raman spectroscopies. Geochimica et Cosmochimica Acta, 61, 1107–1111.

Trolard, F., Bourrié, G., Abdelmoula, M., Refait, P., and Feder, F. (2007) Fougerite, a new mineral of the pyroaurite-iowaite group: Description and crystal structure. Clays and Clay Minerals, 55, 323–334.

Usman, M., Hanna, K., Abdelmoula, M., Zegeye, a., Faure, P., and Ruby, C. (2012) Formation of green rust via mineralogical transformation of ferric oxides (ferrihydrite, goethite and hematite). Applied Clay Science, 64, 38–43.

Vargas, R., Louer, D., and Langford, J.I. (1983) Diffraction line profiles and scherrer constants for materials with hexagonal crystallites. Journal of Applied Crystallography, 16, 512–518.

Vignati, D.A.L., Ferrari, B.J.D., and Dominik, J. (2007) Laboratory-to-field extrapolation in aquatic sciences. Environmental Science & Technology, 41, 1067–1073.

Waychunas, G.A. (2001) Structure, aggregation and characterization of nanoparticles. In J.F. Banfield and A. Navrotsky, Eds., Reviews in Mineralogy and Geochemistry Vol. 44, pp. 105–166. Mineralogical Society of America and the Geochemical Society, Chantilly, Virginia.

Waychunas, G.A., Kim, C.S., and Banfield, J.F. (2005) Nanoparticulate iron oxide minerals in soils and sediments: unique properties and contaminant scavenging mechanisms. Journal of Nanoparticle Research, 7, 409–433.

Williams, A.G.B., and Scherer, M.M. (2001) Kinetics of Cr(VI) reduction by carbonate green rust. Environmental Science & Technology, 35, 3488–3494.

Xue, X., Penn, R.L., Leite, E.R., Huang, F., and Lin, Z. (2014) Crystal growth by oriented attachment: Kinetic models and control factors. CrystEngComm, 16, 1419–1429.

Zegeye, A., Bonneville, S., Benning, L.G., Sturm, A., Fowle, D.A., Jones, C., Canfield, D.E., Ruby, C., MacLean, L.C., Nomosatryo, S., and others (2012) Green rust formation controls nutrient availability in a ferruginous water column. Geology, 40, 599–602.

Zouboulis, A.I., and Moussas, P.A. (2008) Polyferric silicate sulphate (PFSiS): Preparation, characterisation and coagulation behaviour. Desalination, 224, 307–316.

APPENDIX A. SUPPLEMENTAL MATERIAL FOR CHAPTER 2

Observations and Assessment of Iron Oxide and Green Rust Nanoparticles in Metal-Polluted Mine Drainage Within a Steep Redox Gradient

Carol A. Johnson,[A,B,F] Gina Freyer,[B] Maria Fabisch,[B] Manuel A. Caraballo,[A,C,D] Kirsten Kusel,[B,E] and Michael F. Hochella Jr[A]

[A]Department of Geosciences, Virginia Tech, 4044 Derring Hall, 1405 Perry Street, Blacksburg, VA 24061, USA.

[B]Institute of Ecology, Friedrich Schiller University Jena, Dornburger Strasse 159, D-07743 Jena, Germany.

[C]Geology Department, University of Huelva, Campus 'El Carmen', Avenida 3 de Marzo s/n, E-21071 Huelva, Spain.

[D]Mining Engineering Department, University of Chile, Avenida Tupper 2069, 8370451 Santiago, Chile.

[E]German Centre for Integrative Biodiversity Research (iDiv) Halle-Jena-Leipzig, Deutscher Platz 5e, D-04103 Leipzig, Germany.

Environmental Chemistry. **2014**, *11*, 377–391.
http://www.publish.csiro.au/nid/188/paper/EN13184.htm

When taking water samples in the field, whether they are groundwater or surface water, it is well known that those water samples start to transform soon after removal from their native environment. In this study, because we were observing nanoscale features, it was especially critical that we understand the nature of the stability of our samples. Transmission electron microscopy (TEM) grids of water samples from the creek site (18 July 2011) were prepared in the field (~2 h old, with no air exposure until grid preparation which took less than 5 min), in the laboratory a few hours later, and the next day (with fixation with glutaraldehyde to preserve bacteria). Fig. S1 shows scanning electron microscopy images of these three grid types, and it is clear that the samples prepared on the same day look very similar (note the difference in magnifications when comparing particle sizes). However, the sample prepared one day later is

different – characterised by larger primary particles and small needles growing out of the surface of those particles. Therefore, we only analysed water samples by TEM that were less than a day old. Sediment samples were prepared for TEM as soon as possible on the following day, and there was no obvious difference between fixed and unfixed samples.

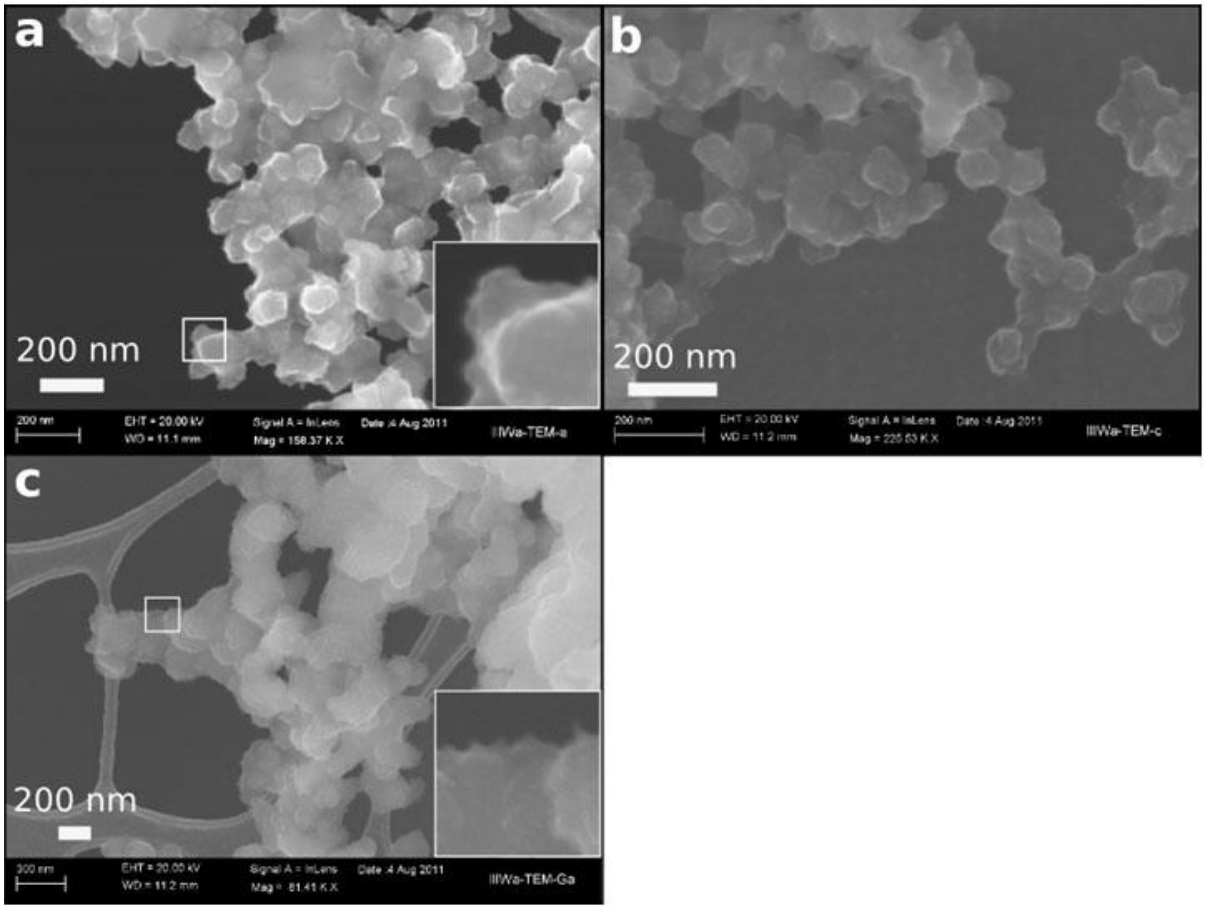

Figure A.1. Representative scanning electron microscopy images of grids showing the evolution of the water samples taken from the creek (18 July 2011) during storage. (a) Prepared grid in the field, (b) prepared grid in the laboratory on the same day as sampling, (c) fixed with glutaraldehyde and prepared the grid one day after sampling.

Table A.1. Water chemistry

Averages (standard deviations) of field triplicates. EC, electrical conductivity; DO, dissolved oxygen; Eh_{corr}, redox potential, corrected to the standard hydrogen electrode

	18 July 2011			25 October 2011		
	Outflow	Terraces	Creek	Outflow	Terraces	Creek
pH	n.d.	5.77	5.83	5.75	6.34	6.10
EC (mS cm^{-1})	n.d.	5.39	4.80	5.54	5.23	4.81
DO (mg L^{-1})	n.d.	n.d.	n.d.	0.6	8.5	5.0
Eh_{corr} (mV)	n.d.	n.d.	n.d.	260	280	307
pe	n.d.	n.d.	n.d.	4.39	4.74	5.20
Total Fe[C] (mM)	6.1 (1.1)[A]	7.2 (1.6)	4.8 (0.4)	5.9 (0.1)	4.9 (0.0)	4.4 (0.1)
<0.1 µm Fe(tot)[D] (mM)	5.9 (0.8)[A,B]	5.1 (0.1)	3.4 (0.2)	5.6 (0.1)	4.3 (0.3)	3.8 (0.0)
<0.2 µm Fe^{II} [E] (mM)	6.1 (0.1)[A]	5.8 (0.2)	3.8 (0.4)	5.64 (0.03)	4.6 (0.1)	3.9 (0.1)
<0.2 µm SO_4^{2-} (mM)	42 (1)[A]	45 (1)	39 (2)	40 (9)	33 (2)	33 (3)

[A]Sample triplicates.

[B]Filtered through a 0.2-µm filter.

[C]Determined by ICP-OES

[D]Determined by ICP-OES

[E]Determined spectrophotometrically

Table A.1. Element concentrations in filtered and unfiltered water

Averages (Avg) and standard deviations (s.d.) of field triplicates in concentrations of micromoles per litre. Maximum contaminant levels (MCL) are from the World Health Organization drinking water quality standards (WHO 2011). n.d., not determined; standard deviations with no replicates are marked by an en-dash.

			18 July 2011						25 October 2011					
			Outflow		Terraces		Creek		Outflow		Terraces		Creek	
		MCL	Total	<0.1 µm	Total	<0.1 µm	Total	<0.1 µm	Total	<0.1 µm	Total	<0.1 µm	Total	<0.1 µm
Al (µM)	Avg		72.4	3.3	77.7	4.1	113.0	11.2	80.5	6.5	4.2	1.1	71.6	16.3
	s.d.		n.d.	n.d.	32.9	0.4	34.2	0.3	0.3	0.1	0.8	0.5	15.7	0.8
As (µM)	Avg	0.133	n.d.	n.d.	n.d.	n.d.	n.d.	n.d.	0.98	0.48	0.25	0.06	0.78	0.13
	s.d.		–	–	–	–	–	–	0.22	0.02	0.05	0.04	0.19	0.01
Ca (µM)	Avg		11371	10867	11970	10766	12503	11494	12374	11791	12072	11599	12793	12808
	s.d.		–	–	1099	374	1030	464	159	675	288	1664	172	377
Cd (µM)	Avg	0.0267	0.0396	0.0336	0.0260	0.0157	0.0842	0.0721	0.0416	0.0294	0.0031	0.0022	0.1039	0.0967
	s.d.		–	–	0.0037	0.0012	0.0051	0.0039	0.0080	0.0000	0.0004	0.0004	0.0012	0.0034
Co (µM)	Avg		13.9	13.5	11.4	10.3	12.1	11.0	12.8	12.7	9.8	9.3	13.4	13.3
	s.d.		–	–	0.2	0.2	0.2	0.2	0.1	0.2	0.2	0.8	0.2	0.1
Cr (µM)	Avg	0.962	0.082	0.005	0.087	0.008	0.037	0.007	0.118	<0.01	<0.01	<0.01	0.028	<0.01
	s.d.		–	–	0.030	0.003	0.013	0.001	0.1	<0.01	<0.01	<0.01	0.0	<0.01
Cs (µM)	Avg		n.d.	n.d.	n.d.	n.d.	n.d.	n.d.	0.055	0.046	0.074	0.069	0.046	0.043
	s.d.		–	–	–	–	–	–	0.004	0.002	0.008	0.010	0.001	0.001
Cu (µM)	Avg	31.5	0.216	0.057	0.328	0.133	2.277	0.475	0.203	0.023	0.023	0.016	1.587	0.662
	s.d.		–	–	0.10	0.06	0.58	0.02	0.11	0.00	0.01	0.00	0.16	0.24
Fe (µM)	Avg	5.37	6131	5900	7239	5050	4783	3385	5903	5626	4880	4309	4405	3809
	s.d.		–	–	1565	78	377	155	130	112	10	329	122	31
Mn (µM)	Avg	7.28	201	200	194	179	249	227	241	240	213	203	258	258
	s.d.		–	–	1	3	4	7	2	2	4	2	3	2
Na (µM)	Avg		2839	2769	3143	2843	2818	2639	3000	2927	3072	3017	2763	2808
	s.d.		–	–	324	119	209	136	87	169	78	430	45	122
Ni (µM)	Avg	1.19	50.0	48.5	48.5	43.1	37.7	33.6	40.3	40.3	34.7	32.7	32.9	33.1
	s.d.		–	–	1.2	1.1	0.5	1.1	0.5	0.3	1.0	3.1	0.2	0.1
Pb (µM)	Avg	0.0483	0.0123	<0.0005	0.0121	0.0012	0.0073	0.0022	0.0201	0.0011	<0.0005	<0.0005	0.0038	<0.0005
	s.d.		–	–	0.0039	0.0011	0.0028	0.0024	0.0127	0.0004	<0.0005	<0.0005	0.0017	<0.0005
Si (µM)	Avg		0.541	0.391	0.537	0.358	0.454	0.360	n.d.	n.d.	n.d.	n.d.	n.d.	n.d.
	s.d.		–	–	0.097	0.004	0.022	0.014	–	–	–	–	–	–
U (µM)	Avg	0.126	0.51	0.47	1.74	0.54	0.44	0.14	0.51	0.45	0.51	0.38	0.41	0.20
	s.d.		–	–	1.40	0.03	0.10	0.01	0.03	0.01	0.12	0.07	0.05	0.01
Zn (µM)	Avg	76.4[A]	23.7	22.9	19.0	16.2	17.9	14.8	20.5	20.1	7.3	6.9	14.2	14.2
	s.d.		–	–	0.8	0.3	2.1	0.3	8.0	7.6	0.5	0.5	0.4	0.0

[A]Suggested maximum level for aesthetic drinking water quality (WHO 2011)

Figure A.2. Gessen Creek field site photos. (a) Gessen Creek just a few metres upstream from the 'creek' site (October 2011), (b) 'terraces' site (June 2011, note the more yellow colour where water is flowing, and reddish-brown where it is not), (c) close-up of terrace sediments (October 2011), (d) 'creek' site (June 2011), (e) creek site sediments (October 2011).

Table A.3. Sediment and sediment pore-water characteristics

Averages (standard deviations) of field triplicates. EC, electrical conductivity

	18 July 2011		25 October 2011	
	Terraces	Creek	Terraces	Creek
pH	5.56	5.51	4.75	5.62
EC (mS cm^{-1})	5.33	4.62	4.18	4.1
Density (g WW cm^{-3})	1.32	1.11	1.40 (0.03)	1.14 (0.10)
Dry weight fraction (g g^{-1} WW)	0.29 (0.05)	0.12 (0.02)	0.38	0.22
Total Fe (mmol g^{-1} DW)	8.41 (0.57)	8.37 (0.02)	9.63 (0.05)	9.12 (0.06)
Pore-water < 0.2 µm Fe^{II} (mM)	5.4 (2.7)	1.5 (0.3)	1.5 (0.6)	1.8 (0.2)

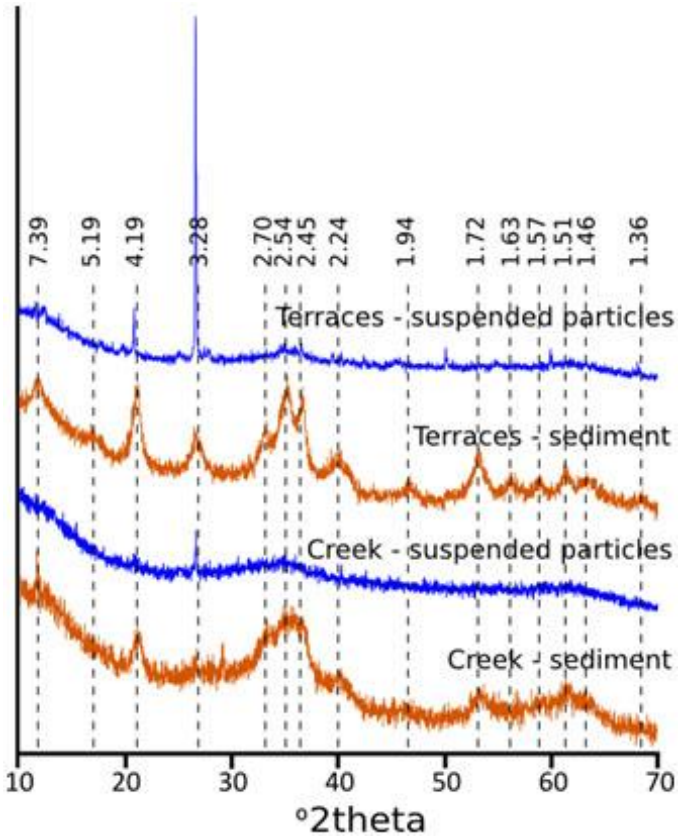

Figure A.3. X-Ray diffraction patterns of suspended particles and sediments in the terrace and creek sites (October 2011). Numbered lines are d-spacings in Angstroms. The y-axis represents the relative intensity.

Table A.1. ICP-MS data from the sequential extraction of sediments

All concentrations in micromoles per gram (dry weight sediment), sampled 18 July 2011 in triplicate. F6 averages are based on less than three replicates, so the standard deviation cannot be calculated

		Terraces							Creek						
		Whole	F1	F2	F3	F4	F5	F6	Whole	F1	F2	F3	F4	F5	F6
Al	Avg	109.13	1.51	0.40	7.13	17.70	0.64	37.47	145.99	1.48	5.68	79.21	17.62	0.48	13.17
	s.d.	3.30	0.03	0.04	0.21	0.56	0.11		3.59	0.35	0.07	0.14	1.77	0.05	
As	Avg	4.850	0.028	0.056	3.258	2.863	0.002	0.024	7.415	0.044	0.118	7.947	1.273	0.000	0.000
	s.d.	0.172	0.005	0.011	0.269	0.084	0.003		0.093	0.014	0.006	0.105	0.066	0.000	0.000
Ca	Avg	52.5	33.9	0.6	1.2	1.1	1.0	0.8	138.6	82.2	3.0	2.8	0.4	0.4	0.4
	s.d.	2.5	1.7	0.1	0.0	0.1	0.1		1.9	5.2	0.2	0.1	0.1	0.1	
Cu	Avg	0.166	0.010	0.008	0.018	0.047	0.000	0.032	4.546	0.036	0.584	2.044	0.748	0.022	0.036
	s.d.	0.011	0.007	0.010	0.006	0.004	0.000		0.165	0.010	0.006	0.009	0.044	0.003	
Fe	Avg	7076	68	71	2908	2645	0	43	5447	66	97	3636	697	0	10
	s.d.	87	7	8	9	79	0		20	20	4	33	67	0	
Mg	Avg	72.26	37.99	0.64	0.93	5.41	1.00	10.53	80.89	59.26	0.42	1.06	1.50	0.41	3.20
	s.d.	3.60	1.13	0.10	0.03	0.14	0.08		1.63	1.95	0.01	0.04	0.06	0.03	
Mn	Avg	1.55	0.37	0.00	0.08	0.53	0.00	0.15	2.40	0.67	0.05	0.49	0.36	0.00	0.04
	s.d.	0.06	0.01	0.00	0.00	0.01	0.00		0.05	0.07	0.00	0.01	0.02	0.00	
Na	Avg	7.81	4.15	0.29	0.00	0.00	0.73	1.12	9.66	5.90	0.00	0.00	0.14	0.19	0.63
	s.d.	0.69	0.17	0.50	0.00	0.00	0.85		2.71	0.34	0.00	0.00	0.24	0.05	
Ni	Avg	1.66	0.46	0.02	0.27	0.51	0.00	0.03	3.53	0.38	0.25	1.20	0.13	0.09	0.02
	s.d.	0.08	0.02	0.00	0.01	0.03	0.00		1.32	0.04	0.00	0.02	0.02	0.04	
P	Avg	32.3	0.3	0.0	9.6	16.2	1.4	1.1	48.1	0.3	0.0	22.8	7.7	2.2	0.4
	s.d.	1.7	0.0	0.0	0.3	0.8	0.4		1.0	0.1	0.0	0.1	0.5	0.1	
S	Avg	2660	633	5	137	904	8	258	4117	1140	89	845	611	2	74
	s.d.	95	9	8	4	23	1	0	85	113	3	15	30	2	
Si	Avg	7.4	8.4	17.9	48.6	68.8	1.2	2.4	11.1	9.2	32.3	133.6	27.9	0.3	1.2
	s.d.	2.7	0.1	3.4	0.9	2.4	0.3		4.6	0.9	0.6	2.4	1.4	0.1	
U	Avg	0.532	0.184	0.100	0.093	0.096	0.001	0.001	1.402	0.015	0.440	0.695	0.024	0.000	0.000
	s.d.	0.012	0.002	0.006	0.001	0.002	0.000		0.005	0.003	0.002	0.020	0.003	0.000	
Zn	Avg	3.75	0.28	0.00	0.56	2.00	0.00	0.09	3.74	0.15	0.13	1.39	0.83	0.00	0.03
	s.d.	0.17	0.02	0.00	0.02	0.05	0.00		0.66	0.02	0.01	0.09	0.03	0.00	

References

World Health Organization, Chemical aspects, in Guidelines for Drinking-Water Quality 2011, pp. 155–201 (WHO Press: Geneva, Switzerland).

APPENDIX B. SUPPLEMENTAL MATERIAL FOR CHAPTER 3

Polycrystallinity of Green Rust Minerals and their Synthetic Analogs: Implications for Particle Formation and Reactivity in Complex Systems

Carol A. Johnson,[A] Mitsuhiro Murayama,[B] Kirsten Küsel,[C,D] and Michael F. Hochella, Jr.[A]

[A]Department of Geosciences, Virginia Polytechnic and State University, 1405 Perry St, Blacksburg, VA 24061, USA

[B]Department of Materials Science and Engineering, Virginia Polytechnic and State University, 445 Old Turner St, Blacksburg, VA 24061, USA

[C]Institute of Ecology, Friedrich Schiller University Jena, Dornburgerstrasse 159, D-07743 Jena, Germany

[D]German Centre for Integrative Biodiversity Research (iDiv) Halle-Jena-Leipzig, Deutscher Platz 5e, D-04103 Leipzig, Germany

To be submitted to American Mineralogist

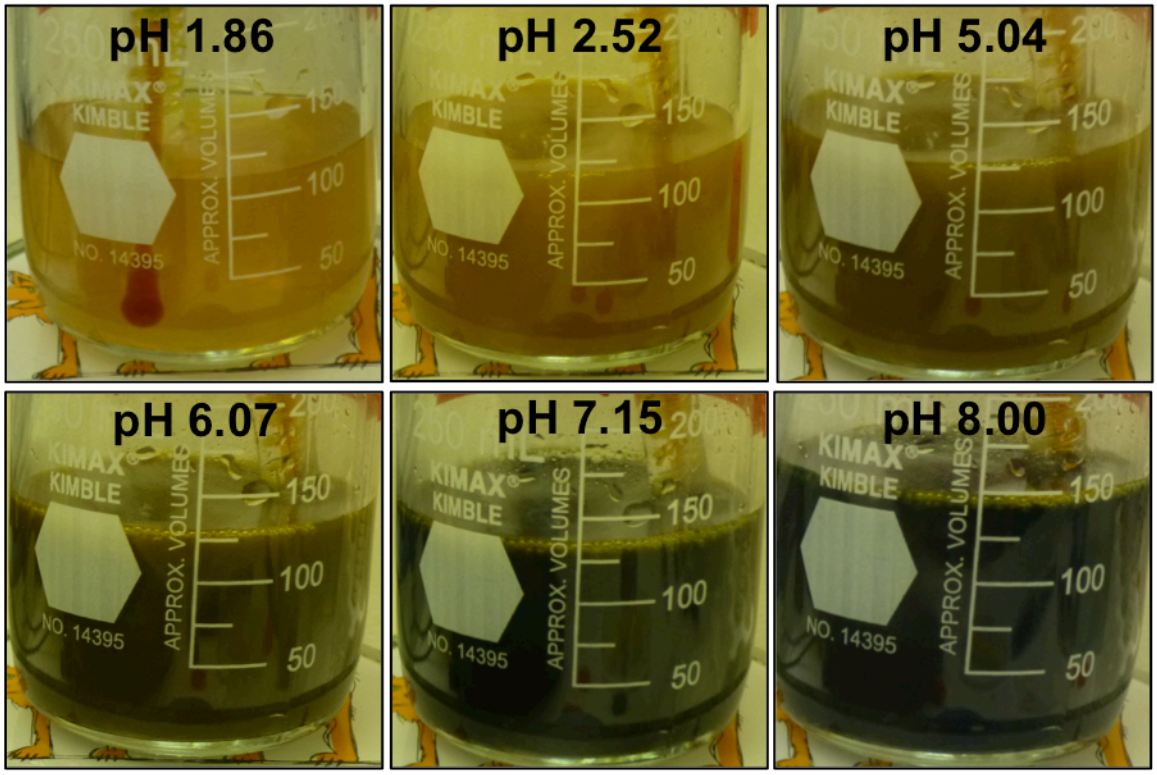

Figure B.1. Color changes during the slow titration of NaOH into Fe(II)-Fe(III) solution during synthesis GR-A.

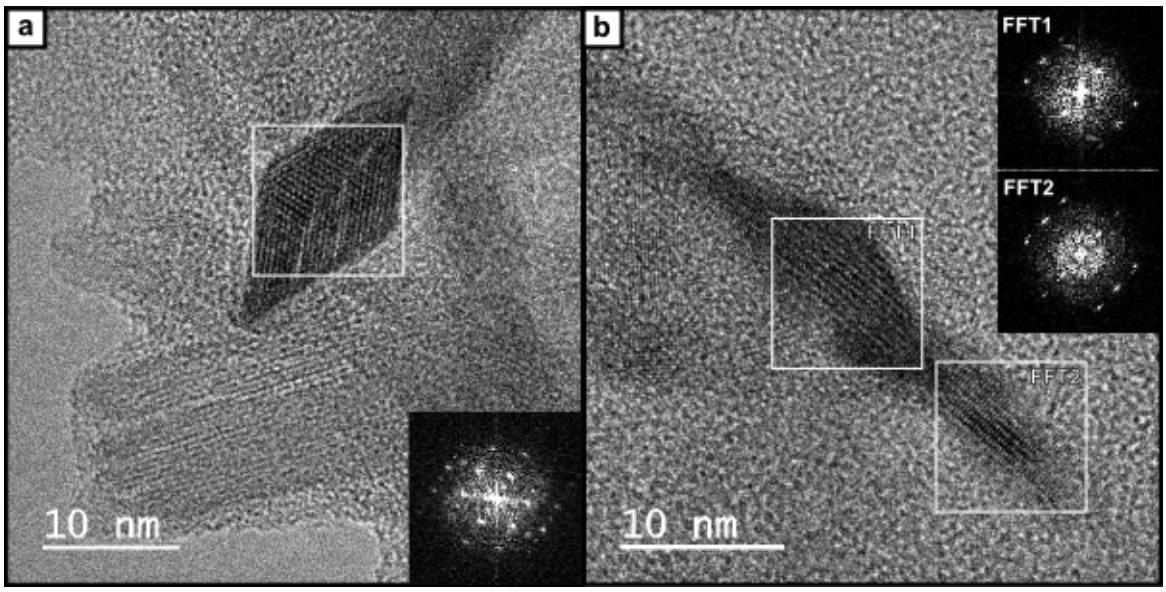

Figure B.2. Additional examples of putative green rust nanorod cross-sections from GR2. (a) Cross-section that is very similar to the one in **Figure 3.8**, with an FFT pattern (inset) that matches exactly with the simulated pattern of sulfate green rust (Simon et al. 2003) oriented along the [100] zone axis. (b) Cross-section with FFT patterns of two regions, which are missing half of the reflections including the (001) reflection.

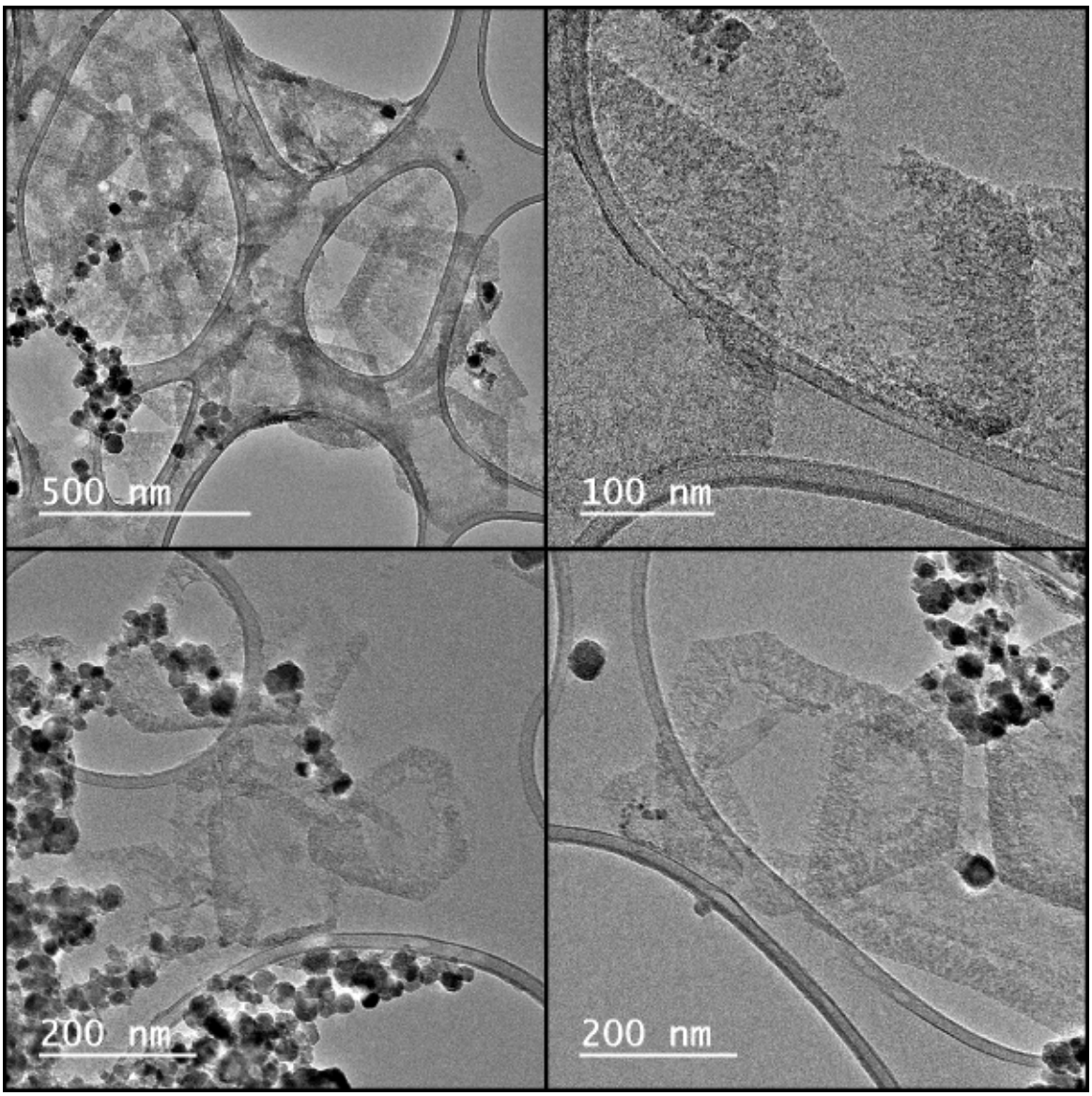

Figure B.3. Low-magnification images of green rust platelets synthesized in GR-B and aged for 90 days, that are undergoing disintegration. Notice that for the most part, the rims remain intact while the center is removed first.

References

Simon, L., François, M., Refait, P., Renaudin, G., Lelaurain, M., and Génin, J.-M.R. (2003) Structure of the Fe(II-III) layered double hydroxysulphate green rust two from Rietveld analysis. Solid State Sciences, 5, 327–334.

APPENDIX C. TRANSFORMATION OF IRON OXIDES IN MINE DRAINAGE SEDIMENT, AND ASSOCIATION WITH SILICA

In this appendix are additional, unpublished data from TEM analysis of the iron oxides sampled from the former Ronneburg uranium mine that were not included in the main chapters of this dissertation.

C.1. Introduction

Previous results presented in Ch. 2 of this dissertation (Johnson et al. 2014) showed that the iron oxide aggregates in the sediments were composed of spheroidal particles that were larger and had rougher surfaces than iron oxide particles in the sediments. In addition, the terrace sediments appeared to have aged more than the creek sediments. The spheroidal particles were approximately the same size, but the terrace sediments had ferrihydrite and goethite nanoneedles protruding from the surface (Johnson et al. 2014). There were also amorphous silica films coating the suspended iron oxide aggregates, but there seemed to be less on the surfaces of the sediment aggregates (Johnson et al. 2014). In order to assess the relationship between the suspended and sedimented iron oxide particles, it would be necessary to look for clues in the core of the particles. This led to the following questions:

1. What is the crystallographic structure of sediment particle cores? Are the cores of the sediments composed of amorphous or poorly crystalline oxides, similar to the composition of the suspended particles?
2. What is the distribution of silica in the sediment particle cores? Does this reflect a core-shell growth or a more homogenous distribution throughout the particles?

3. Are there any clues in the crystalline nanoneedle structure that would help explain the aging mechanism in the sediments?

Analytical transmission electron microscopy (TEM) was used to pursue the answers to these questions, which have implications for understanding the mechanisms for iron oxide growth in Fe^{II}- and silica-rich environments.

C.2. Materials and Methods

Sediment samples from terrace and creek sites were scooped into plastic 50-mL centrifuge tubes on July 18, 2011 as reported in Johnson et al. (2014). The water was decanted in an anoxic chamber under N_2, and then the sediments were frozen and freeze-dried without heat. These freeze-dried sediments were subsequently stored in air at room temperature. The dried powders were mounted in Epofix two-part epoxy and cured at room temperature. The epoxy blocks were then trimmed with a razor to expose some particles, and the resulting block face was cut using an ultramicrotome (RMC PT-PC). Thin sections approximately 70 nm thick were cut using a diamond knife (PELCO) and mounted on copper mesh TEM grids.

In addition, fresh sediment samples were diluted with anoxic (N_2-flushed) ultrapure water in the anoxic chamber and applied to TEM grids (lacey carbon on gold mesh), as detailed in Johnson et al. (2014).

Samples were analyzed by TEM on a JEOL 2100 (LaB_6 thermionic source) operated at 200 kV, and a spherical aberration (Cs)-corrected FEI Titan operated at 300 kV. Cs-corrected TEMs accurately image columns of atoms and allow for structural reconstruction (not performed in this study). Energy dispersive spectroscopy (EDS) elemental composition maps were acquired and semi-quantitively analyzed (using the thin-film approximation) with the software *Analysis Station* (JEOL), and images were analyzed with *Digital Micrograph* (Gatan, Inc).

C.3. Results

TEM imaging of thinly-sliced sections of creek sediments revealed two basic types of aggregates. The aggregates composed of smaller spheroids (Figure C.1a) were solid, and composed of even smaller poorly-crystalline nanoparticles. The SAED pattern exhibited four diffuse rings that match ferrihydrite (Figure C.1c). The EDS spectrum revealed that there was only a trace amount of Si, and the Si/Fe atomic ratio was 0.07 (Figure C.1d). Also present in the creek sediments were aggregates of larger particles with nanoneedles protruding from the surface, similar to terrace sediments in Johnson et al. (2014). However, these particular aggregates with goethite nanoneedles were almost always hollow on the inside (Figure C.1e). Just inside the goethite needles were ferrihydrite nanoparticles (Figure C.1f), which was confirmed by the SAED pattern which exhibited both the four diffuse rings of ferrihydrite and the sharper rings of spots which perfectly matched goethite (Figure C.1g). The EDS spectrum was similar to that of the less crystalline particles, with only a trace amount of Si and an Si/Fe atomic ratio of 0.11 (Figure C.1h).

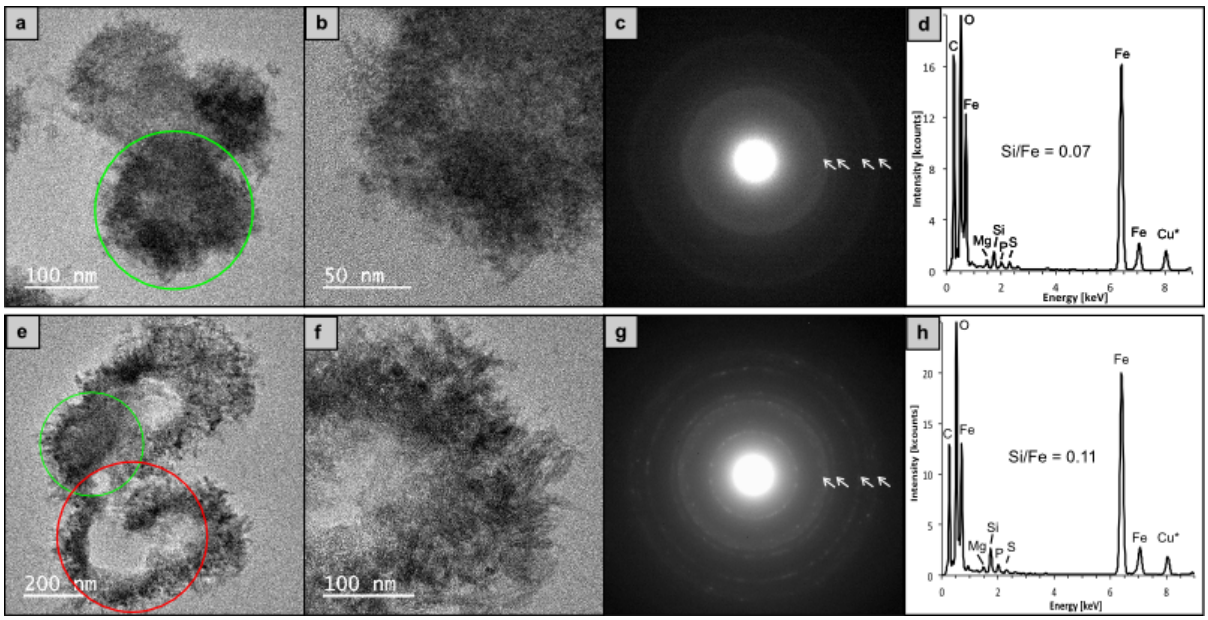

Figure C.1. TEM of typical aggregates in resin-embedded and ultra-microtomed creek sediments. (a) Solid aggregate of aggregated nanoparticles with green circle showing SAED and EDS areas, (b) higher magnification of (a), (c) SAED pattern showing multiple diffuse rings matching ferrihydrite, (d) EDS spectrum with Cu from the TEM grid mesh. (e) Aggregate of nanoparticles and nanoneedles similar to the terrace sediments in Figure C.2, with the red circle showing the SAED area and the green circle showing the EDS area, (f) higher magnification of (e), (g) SAED showing rings of spots matching goethite and diffuse rings matching ferrihydrite, (h) EDS spectrum.

Thin sections of terrace sediments were primarily composed of hollow aggregates (Figure C.2a,b) similar to Figure C.1e,f. On the outer portions of the aggregates were sub-aggregates of goethite nanoneedles, not always oriented outward from the center. Nanoparticles of ferrihydrite were also present, as seen by the same four diffuse rings in the SAED pattern (Figure C.2d). EDS maps and spectrum show that there is only a trace silica peak (Si/Fe = 0.04), and that it is associated with the iron oxide particles and not the embedding resin (Figure C.2e,f).

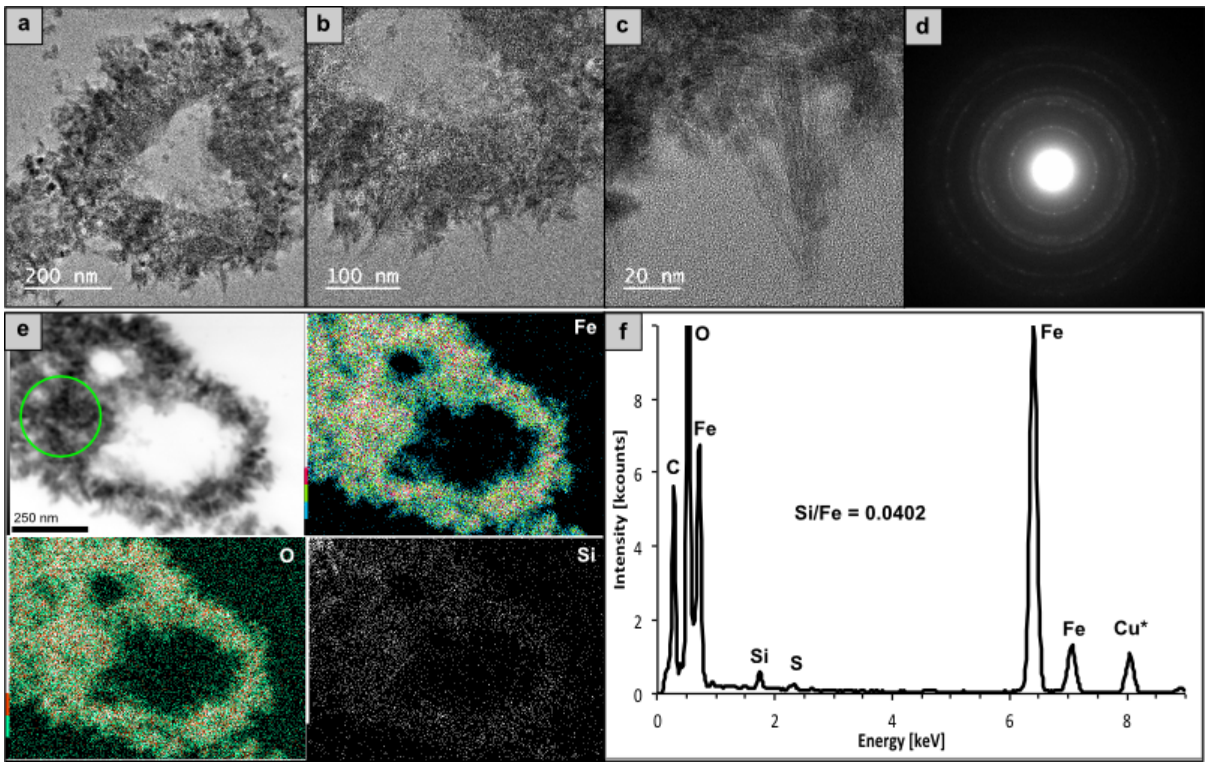

Figure C.2. TEM analysis of resin-embedded, ultra-microtomed terrace sediments. (a) image of a typical aggregate of nanoneedles and nanoparticles with a hollow center, (b) higher magnification showing that the nanoneedles are on the outside and the nanoparticles are towards the inside, (c) close up of some nanoneedles, (d) SAED of a similar area confirms that the presence of goethite (likely the nanoneedles), (e) STEM EDS maps of a similar aggregate showing elements Fe, O, and Si, (f) EDS spectrum of the green circled area in (e), Cu is from the TEM grid mesh.

Figure C.3 shows high-resolution TEM (HR-TEM) images of nanoneedles found growing from spheroidal iron oxide particles in the terrace sediment. These needles are interesting because they are sometimes amorphous, and sometimes amorphous with what appears to be a crystalline core (Figure C.3a,b). The crystalline area in Figure 3c has the structure of goethite along the [010] zone axis, but the d-spacings are much larger than goethite. Currently we do not have an explanation for this.

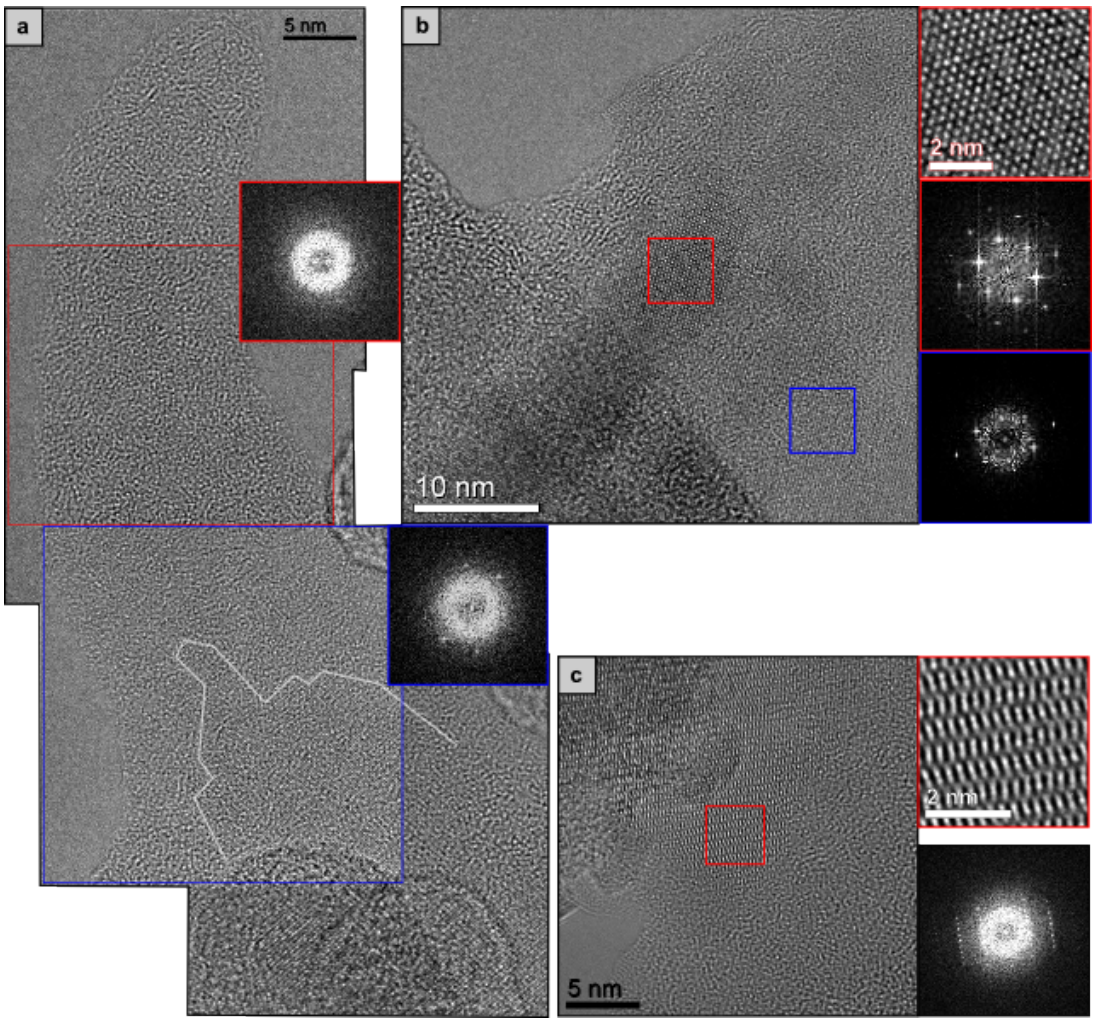

Figure C.3. HR-TEM (using a spherical aberration (Cs)-corrected TEM) images of crystalline and amorphous nanoneedles in the terrace sediments sampled in October 2011 and prepared on a TEM grid by the drop & wick method. (a) Needle that is amorphous except for a region at its base which is crystalline goethite (outlined in white), with FFT areas indicated in red and blue. (b) Crystalline goethite nanoneedle that is either by itself or composes the core of the amorphous needle around it, with FFT areas indicated in red and blue. (c) Area of crystalline iron oxide that matches the structure of goethite but has much larger d-spacings than goethite.

C.4. Discussion

It appears as if there is an additional layer of aggregation in these sediments than was recognized by Johnson et al. (2014). The hierarchy appears to be as follows: nanoparticles of ferrihydrite and goethite aggregate to form spheroidal secondary aggregates up to a few hundred nanometers in diameter, then these spheroids aggregate more loosely into larger tertiary aggregates many micrometers in diameter. The presence of hollow aggregates in the more

crystalline sediments suggests that the ferrihydrite cores could be recrystallizing to form goethite nanorods on the surfaces of the secondary aggregates. This is not quite a satisfying explanation for the hollow character, but the best one at this time. Previously, we inferred that Fe^{II} in the sediment porewater was crystallizing with slower kinetics than the initial formation, and resulted in goethite nanorods in addition to overall spheroidal growth. In addition, we were unable to determine how amorphous silica might be distributed inside the secondary aggregates, because there actually was not much silica present. This leads us to re-think our previous ideas about the transformation of iron oxides in this mine drainage system, and the relationship with amorphous silica.

C.5. Acknowledgements

I gratefully acknowledge Steve McCartney at the ICTAS Nanoscale Characterization and Fabrication Laboratory at Virginia Tech for preparing the ultramicrotomed samples. Andras Kovacs at the Ernst Ruska Centre for Microscopy and Spectroscopy with Electrons (Jülich, Germany) collected the Cs-corrected Titan TEM images.

C.6. References

Johnson, C.A., Freyer, G., Fabisch, M., Caraballo, M.A., Küsel, K., and Hochella Jr., M.F. (2014) Observations and assessment of iron oxide and green rust nanoparticles in metal-polluted mine drainage within a steep redox gradient. Environmental Chemistry, 11, 377-391.

APPENDIX D: DOMINANCE OF '*GALLIONELLA CAPSIFERRIFORMANS*' AND HEAVY METAL RETENTION BY STALK-FORMING IRON OXIDIZERS IN METAL-RICH MINE WATER DISCHARGE

Maria Fabisch[1], Gina Freyer[1], Carol A. Johnson[2], Georg Büchel[3], Denise M. Akob[1,4], Kirsten Küsel[1,5]

[1] Institute of Ecology, Friedrich Schiller University Jena, Dornburger Strasse 159, 07743 Jena, Germany

[2] Department of Geosciences, Virginia Tech, 1405 Perry St, Blacksburg, VA 24061, USA

[3] Institute of Geosciences, Friedrich Schiller University Jena, Burgweg 11, 07749 Jena, Germany

[4] U.S. Geological Survey, 12201 Sunrise Valley Dr., MS 430, Reston, VA 20192, USA

[5] German Centre for Integrative Biodiversity Research (iDiv) Halle-Jena-Leipzig, Deutscher Platz 5e, 04103 Leipzig, Germany

Submitted to *Geobiology* in July 2014

Approval to publish this manuscript here has been given by the U.S. Geological Survey.

D.1. Abstract

Heavy metal-contaminated, pH 6 mine water discharge created new streams and iron-rich terraces at a creek bank in a former uranium-mining area near Ronneburg, Germany. We identified a rapid transition from microoxic, Fe(II)-rich groundwater to oxic surface water providing a suitable habitat for microaerobic iron-oxidizing bacteria (FeOB). In this study, we aimed to i) identify and quantify abundant FeOB in water and iron precipitates along the flow path, ii) study the composition of *Gallionella*-like stalks with scanning and transmission electron microscopy (SEM, TEM) including scanning TEM (STEM), and iii) examine heavy metal retention in terrace and creek sediments. Quantitative PCR demonstrated very high abundance of FeOB with a clear dominance of *Gallionella* spp., accounting for up to 88% of *Bacteria*, along

the water flow path over a 6-month study period, with a minor contribution of other FeOB such as *Sideroxydans* spp. and '*Ferrovum myxofaciens*'. A classical 16S rRNA gene cloning approach demonstrated that most of the *Gallionella*-related clone sequences were ≥97% related to the potentially metal-tolerant '*Gallionella capsiferriformans* ES-2', in addition to known stalk-forming *Gallionellaceae* such as *Gallionella ferruginea* and *Gallionellaceae* strain R-1. *Gallionella*-like twisted stalks were found on glass slides incubated in water and sediment and contained the Fe(III) oxyhydroxide ferrihydrite, as shown with analytical TEM. SEM-EDS and STEM-EDS revealed that the stalks contained Cu, suggesting metal uptake and retention from the contaminated water by the stalks. Sequential extraction of terrace and creek sediments suggested that Cu (52-61%) and other heavy metals were primarily bound to the amorphous and crystalline iron oxide fractions. Overall, the results indicate that putatively metal-tolerant '*G. capsiferriformans*' and other stalk-forming *Gallionellaceae* are key organisms within the microbial communities. The latter might use their stalks also as mechanism for heavy metal resistance in this slightly acidic, mine drainage-impacted freshwater environment.

D.2. Introduction

Microbial iron cycling in iron-rich freshwater was studied extensively in habitats with oxic/anoxic interfaces such as sediment-water interfaces or groundwater seeps (e.g., Lin et al., 2012; Peine et al., 2000; Roden et al., 2012). Circumneutral and slightly acidic groundwater iron seeps usually have ferrous iron [Fe(II)] concentrations in the μM range and often contain mat-like structures and sedimentary iron oxide deposits, where iron-oxidizing bacteria (FeOB) are abundant (Bruun et al., 2010; Duckworth et al., 2009; Kato et al., 2014). Neutrophilic and slightly acidophilic freshwater FeOB often thrive in microoxic habitats due to competition with rapid abiotic iron oxidation in the presence of oxygen (Emerson and Moyer, 1997), e.g.,

microaerobic *Gallionella* spp., *Sideroxydans* spp., or *Leptothrix* spp. (Bruun et al., 2010; Duckworth et al., 2009; Lüdecke et al., 2010). *Gallionella* spp. are obligate, chemolithotrophic, microaerobic, and neutrophilic FeOB (Emerson and Moyer, 1997; Hallbeck et al., 1993) with two recognized species, *Gallionella ferruginea* (Ehrenberg, 1836; Hallbeck et al., 1993) and '*Gallionella capsiferriformans* ES-2' (Emerson et al., 2013). *G. ferruginea* and some other FeOB, but not '*G. capsiferriformans*', develop extracellular, helically-twisted, stalk-like filaments under certain environmental conditions (Hallbeck and Pedersen, 1990). These *Gallionella*-like stalk structures consist of several fibres with a core of exopolysaccharides produced by the cell and encrusted with ferric iron [Fe(III)] oxyhydroxides (Chan et al., 2009; Suzuki et al., 2011). The stalks are thought to prevent cell encrustation by providing surfaces for the precipitation of Fe(III) oxyhydroxides, which form immediately after the enzymatic oxidation of Fe(II) to Fe(III) at circumneutral pH (Chan et al., 2011). As Fe(III) oxyhydroxides are strong sorbents for metal(loid)s in aquatic systems the stalk-associated iron oxyhydroxides could adsorb or coprecipitate heavy metals and metalloids.

Most neutrophilic FeOB have low or unknown metal tolerances, whereas acidophilic FeOB exhibit high metal tolerances (Dopson et al., 2003; Johnson et al., 2014b), since at low pH there are often high heavy metal concentrations due to high solubility. At extremely acidic pH (below 4) abiotic iron oxidation rates are negligible, favouring the growth of aerobic FeOB such as *Acidithiobacillus* spp., *Leptospirillum ferrooxidans*, and '*Ferrovum myxofaciens*' (Hallberg, 2010). Therefore, usually distinct FeOB communities form in circumneutral vs. extremely acidic freshwater habitats that differ in species composition and diversity (Baker and Banfield, 2003; Lear et al., 2009). Seeps of extremely acidic iron-rich waters typically occur as acid mine drainage (AMD) in areas impacted by metal sulfide-mining and contain high concentrations of

soluble metals such as Fe(II) (in the mM range), Cu, Zn, and Mn (Johnson, 2009). At such sites, resident microbial communities were studied extensively in macroscopic growth forms such as acid streamers, mats, or slimes (e.g., Bond et al., 2000; Hallberg et al., 2006; Kay et al., 2013), but less often in AMD-underlying sediments (Bruneel et al., 2011; Church et al., 2007; Garcia-Moyano et al., 2012) or terrace deposits (Brown et al., 2011).

In the former uranium-mining district near Ronneburg, Germany, massive amounts of highly heavy metal-contaminated, pH 6 mine water were seeping out of a grassy hill south of the main drainage area, the Gessenbach creek, since the beginning of 2011. A parallel study showed that this microoxic groundwater discharge contains Zn-bearing green rust, a mixed Fe(II)/Fe(III) layered double hydroxide mineral rarely found in natural waters due to its oxygen sensitivity (Johnson et al., 2014a). These new mining-impacted groundwater seeps created short streams towards the creek and broad terraces of fresh precipitates, primarily composed of the iron oxyhydroxides goethite and ferrihydrite at the creek bank (Johnson et al., 2014a), forming a mining-impacted but only slightly acidic seep environment. Since a high abundance of *Gallionella* spp. was detected in the adjacent drainage creek Gessenbach (Fabisch et al., 2013), we assessed if these FeOB are already present in the contaminated groundwater discharge and if they contributed to the formation of the large iron-rich terraces by quantitative PCR (qPCR) and cloning. We found indications for FeOB contribution to heavy metal retention by studying the presence and composition of *Gallionella*-like twisted stalks and examining the heavy metal distribution in the sediments.

D.3. Materials and Methods

D.3.1. Field sites and sampling

The area under investigation belonged to a mining operation in the former uranium-mining district Ronneburg (Thuringia, Germany), where pyrite oxidation had been caused by the mining processes and sulfuric acid leaching had been conducted. The area is located at the southern flank of the Gessental valley, where the main discharge of mine water arose in 2011 (Figure D.1). Both groundwater and surface waters in this area are still contaminated with heavy metals (Merten et al., 2004; Carlsson et al, 2005; Fabisch et al, 2013). Physical remediation was conducted in the 1990s, which included passive flooding of abandoned underground mine shafts starting in 1998 (Wismut GmbH, 2006). The Gessental valley, as the anticipated main drainage area, was provided with a basic water catchment system designed to collect emerging flood water spilling over a level of 240 m above sea level and to channel it to the Ronneburg water treatment plant (Wismut GmbH, 2006). The flood water reached the level of the valley floor and the Gessenbach creek in August 2006 at about 240 m above sea level. This caused a hydraulic shortcut to form between the flooded mine shafts and the Quaternary aquifer and valley sediments. A bypass was built to allow uncontaminated water of the Gessenbach creek to flow around the contaminated zone; accordingly only contaminated water flows within the bypassed area (Figure D.1). Small local seeps in the grassland area existed back in 2006, emerging from earlier, hydraulically active boreholes. However, in the spring of 2011, the flooding level attained its peak at approximately 20 m above the valley floor and the Gessenbach creek (Wismut GmbH, 2011), which created numerous discharges of underground mine water out from the grassland uphill of the creek over an area of approximately 100 m x 50 m. Large amounts of Fe(III) oxyhydroxides precipitated from the outflowing microoxic, Fe(II)-rich, slightly acidic

water and formed wide iron-rich terraces at the creek bank. The flood water level was then continuously lowered by a defensive well and the discharge of flood water decreased. Today the water table is equal to the level of the valley floor and the Gessenbach creek, and emerging flood water is collected and channeled to the water treatment plant.

Three sites along the flow path of the heavy metal-contaminated discharged water were studied (Figure D.1) and are the same as sampled by Johnson et al. (2014a): site I (outflow) was close to the water discharge, where only limited water samples could be taken due to access difficulties; site II (terrace) represents the iron oxide terraces formed at the creek bank; and site III (creek) is the adjacent mixing site within this bypassed area of the Gessenbach creek. Sampling was conducted on 27th June, 18th July, 25th October, and 14th December in 2011, as well as 23rd April and 10th May in 2012. Triplicate water samples were collected in 50 mL tubes, transported on ice, filtered (0.2 µm or 0.45 µm), acidified, and stored at 4°C for analyses of dissolved organic carbon (DOC), dissolved sulfate, and dissolved metals. Sediment samples for chemical analyses were taken in triplicate from the upper 5 cm into 50 mL tubes, transported on ice, and stored at -20°C. For molecular analyses (clone libraries, qPCR), 1-2 L of water was collected aseptically in 1 L glass bottles, transported on ice, and filtered (0.2 µm, PES, Supor 200, Pall Corporation, USA) immediately upon return to the laboratory. The filters were stored at -80°C until DNA extraction. Sediment samples for molecular analyses were taken aseptically in triplicate, transported on dry ice and stored at -80°C.

D.3.2. Physico-chemical characterization of water and sediment

The pH, redox potential (E_h), and electrical conductivity, as well as dissolved oxygen (DO) in water, were measured *in situ* with the respective electrodes and meters (Mettler Toledo; WTW). The measured E_h was corrected to the standard hydrogen electrode as described in

Johnson et al. (2014a). DOC, dissolved sulfate, dissolved HCl-extractable Fe(II), and dissolved heavy metals in water were determined as described elsewhere (Fabisch et al., 2013). Total Fe in dried and milled sediments was determined in triplicate by inductively coupled plasma optical emission spectrometry (ICP-OES; Spectroflame ICP-OES, Spectro Analytical Instruments Inc., Germany) after total acid digestion (Grawunder et al., 2009). Fresh triplicate sediment samples were dried at 105°C to determine dry weight (dw) and subsequently at 500°C for 5 h to determine ash-free dw for calculation of sediment organic matter.

D.3.3. Sediment total element analysis and sequential extractions

To determine the total concentration and binding affinities of heavy metals to different sediment fractions, sediments from sites II and III were prepared as follows: triplicate sediment samples from July 2011 were centrifuged (10,000 x *g*, 4°C, 1 h) to remove pore water, then freeze dried (no heat) and sieved to a size < 2 mm. For total metal analyses, half of the dried sample was milled, then analyzed after total acid digestion (Grawunder et al., 2009). The other half of the triplicate freeze-dried samples were pooled, then sequentially extracted after Zeien and Brümmer (as discribed in Grawunder et al., 2009; 1989) and analyzed for their metal content. Metal measurements were conducted by inductively coupled plasma mass spectrometry (ICP-MS; X-Series II, Quadrupol, Thermo Electron, Germany) and ICP-OES (Spectroflame ICP-OES, Spectro Analytical Instruments Inc., Germany).

D.3.4. Clone library construction and statistical analysis

Clone libraries were constructed from waters (material on filters after filtration of ca. 1 L of water) and sediments (pooled material from triplicate field samples) of sites I to III obtained in July 2011. DNA extraction with the Power Soil DNA Isolation Kit (MO BIO Laboratories, Inc., CA, USA), 16S rRNA gene amplification, cloning, and sequencing were performed according to

Fabisch et al. (2013). Sequences were trimmed using Geneious Pro v. 4.6.1 (Drummond et al., 2009) and imported into the software MOTHUR v. 1.22.2 (Schloss et al., 2009) for the following steps: alignment to the Greengenes database (DeSantis et al., 2006), chimera identification, grouping into operational taxonomic units (OTUs) based on a 97% sequence cut-off, rarefaction analysis, and similarity analysis. An additional chimera check was conducted using DECIPHER (Wright et al., 2012) and nearest relatives were identified using BLAST against the NCBI GenBank database (Johnson et al., 2008). Coverage was calculated with a standard equation as described by Singleton et al. (2001). The representative 16S rRNA gene sequences for each OTU were deposited in the GenBank database under the accession numbers KF424837 to KF424995 and KF442631.

D.3.5. Quantitative PCR (qPCR)

Copy numbers of 16S rRNA genes of *Archaea*, *Bacteria*, and known FeOB and iron-reducing bacteria (FeRB) groups in water and sediment were determined by qPCR with group-specific primers as given in Fabisch et al. (2013). This included the FeOB *Gallionella* spp., *Sideroxydans* spp., and '*Ferrovum myxofaciens*', as well as the FeRB *Albidiferax ferrireducens* and *Geobacter* spp. 16S rRNA gene copy numbers were then used to calculate the relative abundance of single FeOB/FeRB groups in bacterial communities (estimated percentages) as described in Fabisch et al. (2013). DNA for qPCR was extracted from water filters (ca. 1 L of water filtered) and sediment (pooled triplicate field samples) of sites I to III from June, July, October, and December 2011 using the PowerSoil DNA Isolation Kit according to the manufacturer's instructions (MO BIO Laboratories, Inc., CA, USA). Sediment samples from site II in June and December, as well as from site III in December, were extracted using a modified

DNA extraction procedure after Zhou et al. (1996) to achieve sufficient yield. DNA extraction from site III water in December was not successful.

D.3.6. Light and electron microscopy of *Gallionella*-like twisted stalks

Glass slides (duplicates) protected by perforated 50 mL plastic tubes were placed into the water or sediment (ca. 0 to 10 cm depth) at sites I-III in April 2012. This method (modified from Hanert, 2006) was used to collect indigenous *Gallionella*-like FeOB and their twisted stalks. Slides exposed for 18 d were transported and stored at 4°C in stream water and examined by light microscopy (Axioplan universal microscope, Zeiss, Germany). Slides exposed for 35 d in water of sites I and III were transported at 4°C in 50 mM MES buffer, and material scraped off the slides with a sterile scalpel, each into 2 ml MES buffer (0.05 M), was used for scanning electron microscopy (SEM) and transmission electron microscopy (TEM). Subsamples of slide material were examined by SEM (FEI Quanta 600, with a field emission gun and operated at 20kV), and analyzed for elemental composition with energy dispersive spectroscopy (EDS). TEM grids (lacey carbon on 400 mesh gold, Electron Microscopy Sciences) were prepared by applying multiple 10 µl drops of material suspension to the grids and wicking away gently with a lint-free wipe. As the coatings on these grids were too thick, new grids had to be prepared. For this, the material on the original grids was extracted by placing them into 150 µl of 100% ethanol (ACS grade, Sigma Aldrich) followed by 5 min of sonication. The new grids were prepared using the drop-and-wick method with three 10-µl drops and were examined using a FEI Titan TEM operated at 300 kV. Fast Fourier Transform (FFT) patterns were calculated from high-resolution TEM images and analyzed with the programs ImageJ (National Institutes of Health) and Digital Micrograph (Gatan) to obtain *d*-spacings used for mineral identification. Additionally, these grids were examined with a JEOL 2100 TEM operated in scanning mode

(STEM) to obtain chemical maps by EDS, which were analyzed with the program Analysis Station (JEOL Engineering). To mitigate stray Cu signals, TEM grid holders with beryllium windows were used in both TEMs.

D.4. Results

D.4.1. Physico-chemical characterization of discharged water and precipitates

The outflow water (Iw) was consistently slightly acidic (pH 6.0 ±0.2), microoxic (DO 1.7 ±1.6 mg L^{-1}), and cold (13.0°C ±0.9°C) (Table D.1). It flowed downhill for approximately 20 m with a flow velocity of ca. 0.4 m s^{-1} resulting in a flow time of about 50 s from the outflow to the terraces. Water pH did not change along the flow path, but DO increased rapidly to values near saturation at site II (IIw), where temperatures reached nearly 20°C depending on the season (Table 1). Similarly, water redox potential increased from 244 (±17) to 310 (±45) mV along the water flow path. In contrast, the very high average electrical conductivity appeared to decrease along the water flow path from 5.3 (±0.3) to 4.9 (±0.2) mS cm^{-1}. Average concentrations of dissolved iron, which was almost exclusively Fe(II) at all sites, decreased from 5.1 (±1.2) to 3.9 (±0.6) mmol L^{-1} along the flow path. Total dissolved Fe exceeded the usual concentration of 0.09 to 0.9 mmol L^{-1} in natural freshwaters (WHO, 2011). The water also had high concentrations of other heavy metals in the µM (Mn, Zn, Ni, Co) and nM (U, Cu, Pb, Cd) range (Supplemental Table S1). Some metals exceeded drinking water safety levels (WHO, 2011) and German surface water quality standards (OGewV, 2011), namely Mn (ca. 30-fold), Ni (30- to 120-fold), U (ca. 3-fold), and Cd (up to 115-fold). Dissolved metal concentrations decreased along the flow path from site I to II for Fe, Cd, Cu, Mn, Zn, Ni, and Co. Cu and Cd had a significantly higher dissolved concentration in creek water of site III (IIIw), most likely originating from the upstream creek water (Johnson et al., 2014a). Water always showed very high sulfate

concentrations (33 to 45 mM of dissolved sulfate; Table D.1), likely due to the former pyrite oxidation and sulfuric acid leaching activity.

The pH in the underlying precipitates and sediments was lower compared to the water pH with average values of 4.5 (terrace, IIs) and 5.7 (adjacent creek, IIIs; Table D.1). In the sediments, Fe(III) was the dominant iron species with HCl-extractable Fe(II) accounting for only ca. 1.6% to 6% of total sediment iron. Total iron averaged 4151 mmol L^{-1} (IIs) and 1630 mmol L^{-1} (IIIs) of wet sediment, and represented ca. 50% and 49% of the dw at sites II and III, respectively. The sediments also had high U, Zn, Ni, and Cu contents (Figure D.2), which exceeded the German soil precautionary values (BBodSchV, 1999) and the U background soil level (IAEA, 2014). U, Zn, and Ni had their highest concentrations in the terrace sediment (site II). The standard deviations of the field triplicate sediment total metal measurements were in all cases within 2% of the mean value. Sequential extraction of sediment revealed that the metals Zn (69-78%), Cu (52-61%), and Pb (33-58%) were mainly bound to the amorphous and crystalline iron oxide fractions (Figure D.2). Site II sediment had the highest portions of the metals Mn, Zn, Ni, and Co in the iron fractions, mainly in the crystalline iron fraction.

D.4.2. Identification and quantification of FeOB

We used a clone library approach instead of pyrosequencing to obtain longer partial 16S rRNA gene sequences, as these allow us to determine the affiliation of environmental sequences closer to the species level. A total of 429 clone sequences (between 73 and 91 clones per library) with a median length of 847 bp were screened from five 16S rRNA gene clone libraries constructed from all sites, yielding 21 (Iw), 38 (IIw), 53 (IIIw), 21 (IIs), and 5 (IIIs) OTUs (97% cut-off; Appendix Table E.2). Coverage was between 63% (IIIw) and 98% (IIIs) (Appendix Table E.2). Most of the clone sequences were affiliated with the *Betaproteobacteria* and

Deltaproteobacteria (Appendix Figure E.1). A similarity analysis revealed that water and sediment bacterial communities at site II were most closely related (Appendix Figure E.2).

Very high fractions of clone sequences were most closely related (≥97% 16S rRNA gene sequence identity, SI) to reported FeOB, especially from outflow water (Iw, 57%) and creek sediment (IIIs, 75%; Table D.2). All detected FeOB with ≥97% SI were microaerobic FeOB belonging to the family *Gallionellaceae*. This included '*Gallionella capsiferriformans*' (Emerson et al., 2013), which accounted for most of all clone sequences (38%) and for 96% of *Gallionella*-related clone sequences, the stalk-forming *Gallionella ferruginea* (Hallbeck et al., 1993), *Sideroxydans* sp. CL21 (Lüdecke et al., 2010), and *Gallionellaceae* bacterium R-1 (Krepski et al., 2012). At the 99% SI level, 13% and 10% of sequences in libraries IIs and IIIs, respectively, were most closely related to '*G. capsiferriformans*' (Table D.2). Other well-known FeOB such as '*Sideroxydans lithotrophicus* ES-1' (Emerson et al., 2013), '*Ferritrophicum radicicola*' (Weiss et al., 2007), or the acidophilic aerobic '*Ferrovum myxofaciens*' (Johnson et al., 2014b) were also detected, but with lower sequence identities (93-96%, Appendix Table E.3). In addition, sequences related to known FeRB were identified, with most of these related to *Geobacter psychrophilus* (Nevin et al., 2005) (Table D.2). Five out of the six most frequently detected organisms in all the libraries were most closely related to FeOB or FeRB (SI 93-99%), representing 73% of all clone sequences (Appendix Table D.3). Other clone sequence-related (SI ≥97%) microorganisms included the fermenting *Paludibacter propionicigenes* (Ueki et al., 2006) and *Pelobacter propionicus* (Schink, 1984), the sulfate-reducer *Desulfosporosinus* sp. LauIII (Küsel et al., 2001), as well as the metal-tolerant isolate *Thiomonas* sp. DM-Zn2 (GenBank accession DQ419967; Table D.2).

Gallionella spp. had the highest absolute 16S rRNA gene copy numbers in all samples and at all time points for the five bacterial groups tested (*Gallionella* spp., *Sideroxydans* spp., '*Ferrovum myxofaciens*', *Albidiferax ferrireducens*, *Geobacter* spp.; Table D.3). In addition, *Gallionella* spp. had rather stable absolute gene copy numbers along the flow path, both in water and sediments, with 10^5 to 10^6 copy numbers per mL in water and 10^8 to 10^9 copy numbers per gram wet weight (gww) in sediment. Since copy numbers of *Bacteria* approximated 10^6 per mL water and 10^9 per gww sediment, *Gallionella* spp. accounted for 36-88% (means over time) of the total estimated bacterial cell numbers (Figure D.3), clearly dominating the bacterial communities in water and sediment over the entire study period (Figure D.3). '*Ferrovum myxofaciens*' had its highest abundance in IIw and IIIw and its lowest in the outflow water (Iw), and appeared to be more abundant in June than at other time points. *Archaea* had approximately 10^2 to 10^5 gene copy numbers per mL in water and 10^4 to 10^7 gene copy numbers per gww sediment, thus accounting for only 0.02-2.8% of the total 16S rRNA gene copy numbers (0.05-6.7% of the total estimated prokaryotic cell numbers; Table D.3). The abundance of *Prokarya* was approx. 100 to 1000 times higher in sediments than in the respective overlying water, representing an enrichment of bacteria in the sediments (Table D.3). The patterns of FeOB/FeRB abundance in water and sediment at each site were remarkably similar at the distinct time points and especially as means over time for site I and II.

D.4.3. Light and electron microscopy of *Gallionella*-like stalks

Light microscopy of glass slides exposed along the flow path revealed the occurrence of distinctive helical structures, so-called twisted stalks, at all sites (Appendix Figure E.3). More of these *Gallionella*-like stalks were observed on slides from IIIw. Apical bean-shaped cells were

attached to some stalks from outflow water (Iw; Appendix Figure E.3 A), which is rarely found in environmental samples.

Elemental analysis by SEM-EDS of stalks, which deposited on glass slides from outflow water (Iw) and creek water (IIIw), revealed Fe, O, and Si as the major elements and S and P as the minor elements of the stalks (Figure D.4). Stalk material from IIIw also contained the trace metal Cu as minor element (Figure D.4 D).

Further examination of the mineral structure and elemental composition of one twisted stalk found in outflow water (Iw) by analytical TEM showed that the stalk (Figure D.5 A) was composed of tiny fibrils (ca. 10-20 nm in diameter) with a 2-4 nm crystalline core surrounded by amorphous material (Figure D.5 B-C). FFT patterns (Figure D.5 D and others not shown) calculated from HR-TEM images gave structural *d*-spacings of primarily 2.63, 2.54, 2.1, and 1.5 Å, which match the iron oxyhydroxide mineral ferrihydrite. Similar *d*-spacings exist for akaganéite (β-FeO(OH,Cl)) as well, but the characteristically large spacings at 7.47 and 3.33 Å were not detected. Combined with the structural information from HR-TEM, STEM-EDS mapping was used to provide more insights into the complex internal structure of the twisted stalk. The bright field image of the mapped area along with heat maps of selected elements of interest are presented in Figure D.5 E, where the colour scales for each element are not equivalent and cannot be directly compared. The mapping as well as the EDS spectrum integrated over the whole area (Figure D.5 E-F) showed that the stalks were primarily composed of Fe, O and Si, and that the trace heavy metals Cu and Sn were minor elements. Cu and Sn were homogenously distributed throughout the stalk material and likely correlated with Fe. The dark areas in the bright field image primarily indicated thicker areas, which matched well with areas of highest Fe concentration and also with the thin fibrils. Si is a major element but did not

correlate with Fe; when overlaid, the Si appeared to act as a matrix in-between and around the Fe areas. There was a crescent-shaped hotspot of C, which corresponded well with O and not with Fe, but no obvious parallel filaments of C as shown by Chan et al. (2009). Minor elements also included P, S, Na, and Cl (maps not shown).

D.5. Discussion

D.5.1. Community composition and chemistry of the mine water discharge

The emerging heavy metal-contaminated water had high bacterial 16S rRNA gene copy numbers, representing total cell numbers of approximately 10^5 to 10^6 cells per mL of water, which is in the range of total microbial numbers reported from pristine, shallow groundwater (103 to 108 cells per mL; Akob and Küsel, 2011; Hutchins et al., 2014; Opitz et al., 2014; Pitkanen et al., 2011), and in the upper range of other metal-contaminated groundwaters (103 to 106 cells per mL; Brown et al., 2011; Fields et al., 2005; Hallberg and Johnson, 2005; Wallis and Ladd, 1983; Wang et al., 2014). These numbers were one to two orders of magnitude higher than obtained from iron-rich aquifers in lignite mining areas in Germany (Wang et al., 2014). Chemolithotrophic, iron-oxidizing *Gallionella* spp. were highly abundant and dominant in the outflow water, accounting for 29% to 58% (47% mean over time) of the total estimated bacterial cell numbers. This is similar to the observed dominance of *Gallionella* spp. in groundwater of the lignite-mining area in Germany (Wang et al., 2014). The outflow water represents a typical habitat for *Gallionella* at the interface between anoxic, iron-rich and oxic, circumneutral waters (Emerson and Moyer, 1997; Hanert, 2006). However, the *Gallionella* spp. abundance did not change along the flow path, whereas the absolute abundances of the low-abundance FeOB groups *Sideroxydans* spp. and '*Ferrovum* sp.' increased ca. 10-fold in water between outflow and terraces. The FeRB groups *Geobacter* spp. and *Albidiferax* spp. were also important in the

microoxic water outflow accounting for ca. 30% (mean over time) of the bacterial community. Taken together, organisms related to microbial groups involved in iron cycling made up 62% to 106% of the total mine water discharge community.

The predominant metal in the discharged water is iron, specifically Fe(II) in the dissolved fraction (<0.1 μm) and Fe(III) in suspended particles (Johnson et al., 2014a). In the parallel study by Johnson et al. (2014a), the detailed composition and mineralogy of water and suspended/precipitated particles along the flow path was examined to investigate the transport of contaminants. The microoxic water discharge contains suspended particles of the mineral "green rust", known to be formed by reduction of Fe(III) oxyhydroxides by *Shewanella putrefaciens* in the presence of high sulfate concentrations (Ona-Nguema et al., 2004), as available in the outflow water. The presence of such a mixed-Fe(II)/Fe(III)-mineral reflects environmental conditions suitable for iron cycling in the groundwater. Johnson et al. (2014a) also found that Fe and other heavy metals such as Mn, Ni, Zn, and U were mainly (>90%) in the dissolved fraction in the water discharge, while large portions of Si, Al, Cu, and As were also associated with suspended particles. Water sampled at the terraces contained higher portions of Fe, Ni, Zn, and U associated with suspended particles, e.g., up to 69% of U, and lower dissolved metal concentrations. Thus, rapid transformation reactions occurred when the microoxic water became oxidized after emerging from underground.

D.5.2. Formation of iron-rich terraces

The decrease in dissolved Fe(II) along the water flow path is caused by oxidation to Fe(III) followed by rapid precipitation and settling of Fe(III) mineral phases forming the terraces as suggested by Johnson et al. (2014a). The freshly formed terrace sediment had the highest total concentration of Fe, U, Zn, and Ni and also the highest portion of the metals Zn, Ni, and Co in

the sediment iron fractions (mostly crystalline iron fraction). Thus, high amounts of these metals were already incorporated in the sediments of the terraces despite the high flow velocity and short flow time, pointing to a fast precipitation of Fe(III)-rich particles. Additionally, the bacterial community composition of the terrace sediment was very similar to the one in the overlying water phase, indicating a direct impact of the water community on the sediment community and a fast formation of the iron-rich precipitates at the terrace site. The higher acidity of the terrace sediment (pH 4.5) compared to the slightly acidic pH 6.0 in the flowing water may have resulted from the generation of H^+ ions by Fe(II) oxidation. An enhanced iron oxidation was suggested by the ca. 1000 times higher abundances of *Gallionella* spp., *Sideroxydans* spp., and '*Ferrovum myxofaciens*' in the sediment compared to the overlying water. Similar enrichment was also shown for Tinto river sediment (Garcia-Moyano et al., 2012). The existence of free *Gallionella*-like stalks and of bean-shaped cells attached to stalks in outflow water is evidence for obligate iron-oxidizing metabolic activity of stalk-forming FeOB in this metal-contaminated environment.

The water at the terraces had high oxygen concentrations ranging from 5.5 to 9.7 mg L^{-1}, which would promote abiotic iron oxidation. However, high microbial iron oxidation rates at high oxygen concentrations are possible, as demonstrated by high numbers of *Gallionella* spp. in groundwater with high oxygen concentration (3.7 mg L^{-1}; (Wang et al., 2014) and high oxygen tolerance of *Gallionella* spp. (up to 6.7 mg L-1 by Gallionella ferruginea, Emerson and Weiss, 2004; Sogaard et al., 2001). The main factors that decrease abiotic iron oxidation rates and enable FeOB to compete are microoxic conditions (Druschel et al., 2008; Emerson and Moyer, 1997; Williamson et al., 2006, and references therein), low pH (100-fold lower with a decrease in 1 pH unit; Stumm and Lee, 1961) and low temperature (10-fold lower at a 15°C-decrease;

Stumm and Lee, 1961; Sung and Morgan, 1980). Interestingly, the most important detected FeOB, '*Gallionella capsiferriformans*', *G. ferruginea*, and '*Ferrovum myxofaciens*', as well as FeRB, *Geobacter psychrophilus* and *Albidiferax ferrireducens*, are psychrotolerant or psychrophilic bacteria (Emerson and Moyer, 1997; Finneran et al., 2003; Hallbeck and Pedersen, 1990; Johnson et al., 2014b; Nevin et al., 2005). These organisms are able to thrive at temperatures below 15°C and thus, are competitive especially at temperatures common in groundwater. Retardation of abiotic iron oxidation due to low temperatures (13°C) resulted in uninhibited growth of *G. ferruginea* and a dominance of microbial iron oxidation in drinking water at circumneutral pH (de Vet et al., 2011). Furthermore, high ionic strength due to the presence of anions such as sulfate or chloride also significantly decreases abiotic iron oxidation rates in slightly acidic to neutral aqueous solutions (Sung and Morgan, 1980), likely relevant to the Ronneburg waters with high sulfate concentration and conductivity. Taken together, a pH of 6.0 or lower, high ionic strength, low temperatures, and low oxygen in outflow water appears to be enhancing the competitiveness of FeOB and causing the high abundance of *Gallionella* spp.

D.5.3. Identification of potential key species

Gallionella spp. accounted for 36-88% of *Bacteria* and were dominant at all sites and at almost all time points, even reaching more than the theoretical percentage of 100% in sediments of sites II and III. A possible explanation for the higher than 100% abundance might be an underestimated number of 16S rRNA genes in the genomes of *Gallionella* spp., since only two published full genomes are available (Emerson et al., 2013; Genbank accession ARAT00000000.1). Very high abundances of *Gallionella* spp. were detected at a pH down to 4.5 (mean over time in IIs, even pH 3.7 in June 2011), lower than compared to the growth conditions of the two isolated species *G. ferruginea* (pH range 5.0-6.5; Hallbeck and Pedersen, 1990) and

'*G. capsiferriformans*' (pH range 5.5-7.0; Emerson et al., 2013). The dominance of *Gallionella* spp. is consistent with their preference for lower DOC contents (around 5 mg L^{-1}) and temperature (around 12°C) compared to *Leptothrix* sp.-dominated habitats (Fleming et al., 2014), and supports the observation that sufficient soluble Fe(II) is very important for its growth (de Vet et al., 2011; Hanert, 2006), even at high oxygen or heavy metal concentrations. The study by Fleming et al. (2014) also indicated that *Gallionellales* thrive at higher metal (e.g., Ni, Cu, Zn, Al, K) concentrations than *Leptothrix* sp. Microaerobic FeOB enriched from pH 6.3 Gessenbach creek sediment were shown to grow in the presence of heavy metals in the mM range (Fabisch et al., 2013). Heavy metal tolerance genes could be obtained by uptake of plasmids, or they might already be present in the genome as was recently demonstrated for '*G. capsiferriformans*' (Emerson et al., 2013). *Gallionella* spp. were previously detected in AMD (see references in Table 2), but were rarely reported to be the main community component and putative key organisms in a heavy metal-contaminated environment. Our results suggest an important role for these neutrophilic, microaerobic FeOB in heavy metal-contaminated, slightly acidic freshwater environments.

The vast majority of the *Gallionella* spp.-related clone sequences (96%) and 38% of all cloned sequences were most closely related to '*G. capsiferriformans* ES-2' (97-99% 16S rRNA gene SI). Particularly in creek sediment (IIIs), 75% of the clone sequences were most related to '*G. capsiferriformans*'. This suggests that most of the highly abundant *Gallionella* spp., detected by qPCR, might be related to this species. As the '*G. capsiferriformans*' genome contains genes for heavy metal efflux pumps as well as genes for mercury and arsenic resistance (Emerson et al., 2013), it may have an advantage over *G. ferruginea* and other microaerobic FeOB in this high metal environment. Nonetheless, *G. ferruginea* was present (demonstrated by cloning and

indicated by the finding of *G. ferruginea*-like stalks and cells), although it was mostly present in water, whereas '*G. capsiferriformans*' was detected in water and sediments II and III (99% SI).

All detected FeOB and FeRB (with ≥97% SI of clone sequences) were previously reported from freshwater habitats and from contaminated environments (except bacterium R-1; Table D.2). Most of these organisms are typical neutrophiles and all detected FeOB were described as microaerobic or aerobic (Table D.2, Appendix Table E.3), with a clear dominance of *Gallionellaceae* and especially '*G. capsiferriformans*'. *G. ferruginea*-, *Sideroxydans* sp. CL21-, and *Geothrix fermentans*-related clone sequences were also detected in Gessenbach creek sediment with a pH of 6.3 (Fabisch et al., 2013). The acidophilic AMD-inhabiting FeOB '*Ferrovum myxofaciens*' was only related to one clone in IIIw with only 94% SI, but is abundant at the Ronneburg site at pHs of up to 6.5 as shown by qPCR. So we assume that some "*F. myxofaciens*" strains can occur at even higher pH than the growth range shown for the type strain P3G (ca. 2-5; Johnson et al., 2014b). *Leptothrix* spp., typical FeOB in pristine iron-containing freshwater, were not detected in the Ronneburg area, maybe due to a lack of metal tolerance.

D.5.4. Mineralogy and heavy metal retention of *Gallionella*-like twisted stalks

Elemental analysis of *Gallionella*-like stalks from pH 6 outflow and creek water by SEM- and TEM-EDS revealed Fe, O, Si, and C as main elements of the stalk material, similar to what was reported by Suzuki et al. (2011). These *Gallionella*-like stalks contained the Si-coprecipitated Fe(III) oxyhydroxide ferrihydrite. Iron oxyhydroxides coprecipitated with amorphous silica were also detected in particles of water and sediment at the terraces and in the creek (Johnson et al., 2014a). Ferrihydrite was previously shown to be part of *Gallionella*-like stalks (Banfield et al., 2000; Chan et al., 2009) and was found as component of the suspended particles and precipitates at sites II and III (Johnson et al., 2014a). The current model of such

stalks, consisting of organic polymers mineralized by or encrusted with inorganic Fe(III) oxyhydroxides (Chan et al., 2009; Suzuki et al., 2011), could not be confirmed because obvious C-rich fibrils were not apparent with STEM-EDS mapping. Such helically-twisted stalks are characteristic of microaerobic FeOB such as the freshwater-inhabiting *Gallionellaceae G. ferruginea* (Hallbeck et al., 1993), *Ferriphaselus amnicola* (Kato et al., 2014), and *Gallionellacea* bacterium R-1 (Krepski et al., 2012), or the marine '*Zetaproteobacterium*' *Mariprofundus ferrooxydans* (Emerson et al., 2007). Formation of the stalks detected in the Ronneburg area by the marine *M. ferrooxydans* is unlikely, but *G. ferruginea* (in Iw, IIIw, IVw) and *Gallionellaceae* R-1 (in IIIw) were detected by cloning and presumably formed the stalks.

Remarkably, Cu was associated with material of *Gallionella*-like twisted stalks from outflow water (site I) and creek water (site III), although the detection of metals on individual particles by SEM and TEM can be difficult when concentrations are lower than ca. 0.1 atom percent. Only a few studies have shown metal(loid) association with biogenic *Gallionella*-like stalks, such as Cu and Zn in a drinking-water distribution system (Ridgway et al., 1981) or As in contaminated mine water at pH 4.7 (Ohnuki et al., 2004). Cu is commonly associated with iron oxides in slightly acidic pH environments and especially AMD (Genovese and Mellini, 2007; Hochella et al., 1999). Cu was mainly associated with the particulate fraction in Ronneburg water (Johnson et al., 2014a) and was found by sequential extractions in this study to be mainly (52-61%) and in large amounts (up to 135 µg per g dw in IIIs) bound to amorphous and crystalline iron oxides in the sediments. When these sediment samples were extracted with a method more specific for iron-rich samples in triplicate, a high percentage of 39-61% of Cu bound to the iron oxide fractions was confirmed (Johnson et al., 2014a). Cu-bearing *Gallionella*-like stalks present in water could settle out and accumulate in the sediments, thereby contributing

to Cu retention in the former Ronneburg mining area. An important role of intermixed iron oxides and bacterial organic matter in the transport and fate of metals was suggested (Ferris et al., 2000). Our results demonstrated a more specific role of microbes to contaminant removal processes: contributing to iron oxidation, inducing stalk formation, and providing nucleation sites for iron oxides, which can then take up metal contaminants.

D.6. Conclusions

Due to the favourable environmental conditions (slightly acidic pH, low temperature, and high ionic strength), the high abundance of FeOB, and their indicated metabolic activity, a contribution of microbial iron oxidation to the formation of the terraces in the former Ronneburg mining area is very likely. Our results demonstrate the dominance of the obligate microaerobic FeOB *Gallionella* spp. within the microbial communities, likely to a great extent '*Gallionella capsiferriformans*', whose putative heavy metal tolerance could be an advantage over other FeOB in this high metal environment. Material of *Gallionella*-like twisted stalks contributed to the retention of heavy metals such as Cu and Sn in the former Ronneburg mining area. Therefore, the formation of twisted stalks by a FeOB may be useful not only against the encrustation of the cell surface by iron oxyhydroxides, but also for the immobilization and detoxification of dissolved heavy metals. Overall, the importance of *Gallionella* spp. and the contribution of *Gallionella*-like twisted stalks to metal retention in slightly acidic mine drainage environments is indicated.

D.7. Acknowledgements

The authors thank the graduate research training group "Alteration and element mobility at the microbe-mineral interface" (GRK 1257), which is part of the Jena School for Microbial Communication (JSMC) and funded by the Deutsche Forschungsgemeinschaft (DFG) for

financial support of Maria Fabisch. Carol Johnson was financially supported by the National Science Foundation (NSF) Integrative Graduate Education and Research Traineeship program and through the Center for the Environmental Implications of NanoTechnology (CEINT) by the NSF and Environmental Protection Agency (EPA). The authors would also like to thank Maren Sickinger for excellent technical assistance; Shipeng Lu, Juanjuan Wang, and Martina Herrmann for help with qPCR and discussions; and Michael F. Hochella Jr. for electron microscopy advice and support. We thank Dirk Merten and Daniela Sporleder for sequential extraction and ICP measurements, Katy Pfeiffer and Kai-Uwe Totsche for freeze drying of sediment samples, as well as Beate Michalzik and Susanne Richter for water DOC analyses. The Institute for Critical Technology and Applied Science (ICTAS) Nanoscale Characterization and Fabrication Laboratory at Virginia Tech provided access to and assistance with SEM and TEM instrumentation.

The authors hereby declare that none of the authors have any potential sources of conflict of interest. Any use of trade, product, or firm names is for descriptive purposes only and does not imply endorsement by the U.S. Government.

D.8. References

Akob, D.M., and Küsel, K. (2011) Where microorganisms meet rocks in the Earth's Critical Zone. Biogeosciences, 8(12), 3531-3543.

Baker, B.J., and Banfield, J.F. (2003) Microbial communities in acid mine drainage. FEMS Microbiology Ecology, 44(2), 139-152.

Banfield, J.F., Welch, S.A., Zhang, H.Z., Ebert, T.T., and Penn, R.L. (2000) Aggregation-based crystal growth and microstructure development in natural iron oxyhydroxide biomineralization products. Science, 289(5480), 751-754.

BBodSchV. (1999) Bundes-Bodenschutz- und Altlastenverordnung (Federal Soil Protection and Contaminated Sites Ordinance). German Federal Ministry of Justice, available online at: http://www.gesetze-im-internet.de/bbodschv/index.html.

Bollmann, A., Lewis, K., and Epstein, S.S. (2007) Incubation of environmental samples in a diffusion chamber increases the diversity of recovered isolates. Applied and Environmental Microbiology, 73(20), 6386-6390.

Bond, P.L., Smriga, S.P., and Banfield, J.F. (2000) Phylogeny of microorganisms populating a thick, subaerial, predominantly lithotrophic biofilm at an extreme acid mine drainage site. Applied and Environmental Microbiology, 66(9), 3842-3849.

Brodie, E.L., DeSantis, T.Z., Joyner, D.C., Baek, S.M., Larsen, J.T., Andersen, G.L., Hazen, T.C., Richardson, P.M., Herman, D.J., Tokunaga, T.K., Wan, J.M., and Firestone, M.K. (2006) Application of a high-density oligonucleotide microarray approach to study bacterial population dynamics during uranium reduction and reoxidation. Applied and Environmental Microbiology, 72(9), 6288-6298.

Brown, J.F., Jones, D.S., Mills, D.B., Macalady, J.L., and Burgos, W.D. (2011) Application of a depositional facies model to an acid mine drainage site. Applied and Environmental Microbiology, 77(2), 545-554.

Bruneel, O., Duran, R., Casiot, C., Elbaz-Poulichet, F., and Personne, J.-C. (2006) Diversity of microorganisms in Fe-As-rich acid mine drainage waters of Carnoulès, France. Applied and Environmental Microbiology, 72(1), 551-556.

Bruneel, O., Volant, A., Gallien, S., Chaumande, B., Casiot, C., Carapito, C., Bardil, A., Morin, G., Brown Jr., G.E., Personne, C.J., Le Paslier, D., Schaeffer, C., Van Dorsselaer, A., Bertin, P.N., Elbaz-Poulichet, F., and Arsene-Ploetze, F. (2011) Characterization of the active bacterial community involved in natural attenuation processes in arsenic-rich creek sediments. Microbial Ecology, 61(4), 793-810.

Bruun, A.-M., Finster, K., Gunnlaugsson, H.P., Nornberg, P., and Friedrich, M.W. (2010) A comprehensive investigation on iron cycling in a freshwater seep including microscopy, cultivation and molecular community analysis. Geomicrobiology Journal, 27(1), 15-34.

Burkhardt, E.-M., Akob, D.M., Bischoff, S., Sitte, J., Kostka, J.E., Banerjee, D., Scheinost, A.C., and Küsel, K. (2010) Impact of biostimulated redox processes on metal dynamics in an iron-rich creek soil of a former uranium mining area. Environmental Science & Technology, 44(1), 177-183.

Burkhardt, E.-M., Bischoff, S., Akob, D.M., Büchel, G., and Küsel, K. (2011) Heavy metal tolerance of Fe(III)-reducing microbial communities in contaminated creek bank soils. Applied and Environmental Microbiology, 77(9), 3132-3136.

Ceja-Navarro, J.A., Nguyen, N.H., Karaoz, U., Gross, S.R., Herman, D.J., Andersen, G.L., Bruns, T.D., Pett-Ridge, J., Blackwell, M., and Brodie, E.L. (2014) Compartmentalized microbial composition, oxygen gradients and nitrogen fixation in the gut of *Odontotaenius disjunctus*. ISME Journal, 8(1), 6-18.

Chan, C.S., Fakra, S.C., Edwards, D.C., Emerson, D., and Banfield, J.F. (2009) Iron oxyhydroxide mineralization on microbial extracellular polysaccharides. Geochimica et Cosmochimica Acta, 73(13), 3807-3818.

Chan, C.S., Fakra, S.C., Emerson, D., Fleming, E.J., and Edwards, K.J. (2011) Lithotrophic iron-oxidizing bacteria produce organic stalks to control mineral growth: implications for biosignature formation. ISME Journal, 5(4), 717-727.

Church, C.D., Wilkin, R.T., Alpers, C.N., Rye, R.O., and McCleskey, R.B. (2007) Microbial sulfate reduction and metal attenuation in pH 4 acid mine water. Geochemical Transactions, 8, 10.

Coates, J.D., Ellis, D.J., Gaw, C.V., and Lovley, D.R. (1999) *Geothrix fermentans* gen. nov., sp nov., a novel Fe(III)-reducing bacterium from a hydrocarbon-contaminated aquifer. International Journal of Systematic Bacteriology, 49, 1615-1622.

de Vet, W.W.J.M., Dinkla, I.J.T., Rietveld, L.C., and van Loosdrecht, M.C.M. (2011) Biological iron oxidation by *Gallionella* spp. in drinking water production under fully aerated conditions. Water Research, 45(17), 5389-5398.

DeSantis, T.Z., Hugenholtz, P., Larsen, N., Rojas, M., Brodie, E.L., Keller, K., Huber, T., Dalevi, D., Hu, P., and Andersen, G.L. (2006) Greengenes, a chimera-checked 16S rRNA gene database and workbench compatible with ARB. Applied and Environmental Microbiology, 72(7), 5069-5072.

Dopson, M., Baker-Austin, C., Koppineedi, P.R., and Bond, P.L. (2003) Growth in sulfidic mineral environments: metal resistance mechanisms in acidophilic micro-organisms. Microbiology, 149, 1959-1970.

Drummond, A.J., Ashton, B., Cheung, M., Heled, J., Kearse, M., Moir, R., Stones-Havas, S., Thierer, T., and Wilson, A. (2009) Geneious v4.7., p. available online at: http://www.geneious.com/.

Druschel, G.K., Emerson, D., Sutka, R., Suchecki, P., and Luther, G.W. (2008) Low-oxygen and chemical kinetic constraints on the geochemical niche of neutrophilic iron(II) oxidizing microorganisms. Geochimica et Cosmochimica Acta, 72(14), 3358-3370.

Duckworth, O.W., Holmstrom, S.J.M., Pena, J., and Sposito, G. (2009) Biogeochemistry of iron oxidation in a circumneutral freshwater habitat. Chemical Geology, 260(3-4), 149-158.

Ehrenberg, C.G. (1836) Vorläufige Mittheilungen über das wirkliche Vorkommen fossiler Infusorien und ihre grosse Verbreitung. Annalen der Physik, 38, 213–227.

Emerson, D., Field, E.K., Chertkov, O., Davenport, K.W., Goodwin, L., Munk, C., Nolan, M., and Woyke, T. (2013) Comparative genomics of freshwater Fe-oxidizing bacteria: implications for physiology, ecology, and systematics. Frontiers in Microbiology, 4, 254.

Emerson, D., and Moyer, C. (1997) Isolation and characterization of novel iron-oxidizing bacteria that grow at circumneutral pH. Applied and Environmental Microbiology, 63(12), 4784-4792.

Emerson, D., Rentz, J.A., Lilburn, T.G., Davis, R.E., Aldrich, H., Chan, C., and Moyer, C.L. (2007) A novel lineage of proteobacteria involved in formation of marine Fe-oxidizing microbial mat communities. PLoS ONE, 2(8), e667.

Emerson, D., and Weiss, J.V. (2004) Bacterial iron oxidation in circumneutral freshwater habitats: Findings from the field and the laboratory. Geomicrobiology Journal, 21(6), 405-414.

Fabisch, M., Beulig, F., Akob, D.M., and Küsel, K. (2013) Surprising abundance of *Gallionella*-related iron oxidizers in creek sediments at pH 4.4 or at high heavy metal concentrations. Frontiers in Microbiology, 4, 390.

Ferris, F.G., Hallberg, R.O., Lyven, B., and Pedersen, K. (2000) Retention of strontium, cesium, lead and uranium by bacterial iron oxides from a subterranean environment. Applied Geochemistry, 15(7), 1035-1042.

Fields, M.W., Yan, T.F., Rhee, S.-K., Carroll, S.L., Jardine, P.M., Watson, D.B., Criddle, C.S., and Zhou, J.Z. (2005) Impacts on microbial communities and cultivable isolates from groundwater contaminated with high levels of nitric acid-uranium waste. FEMS Microbiology Ecology, 53(3), 417-428.

Finneran, K.T., Johnsen, C.V., and Lovley, D.R. (2003) *Rhodoferax ferrireducens* sp nov., a psychrotolerant, facultatively anaerobic bacterium that oxidizes acetate with the reduction of Fe(III). International Journal of Systematic and Evolutionary Microbiology, 53, 669-673.

Fleming, E.J., Cetinic, I., Chan, C.S., King, D.W., and Emerson, D. (2014) Ecological succession among iron-oxidizing bacteria. ISME Journal, 8(4), 804-815.

Garcia-Moyano, A., Gonzalez-Toril, E., Aguilera, A., and Amils, R. (2012) Comparative microbial ecology study of the sediments and the water column of the Rio Tinto, an extreme acidic environment. FEMS Microbiology Ecology, 81(2), 303-314.

Genovese, A., and Mellini, M. (2007) Ferrihydrite flocs, native copper nanocrystals and spontaneous remediation in the Fosso dei Noni stream, Tuscany, Italy. Applied Geochemistry, 22(7), 1439-1450.

Grawunder, A., Lonschinski, M., Merten, D., and Büchel, G. (2009) Distribution and bonding of residual contamination in glacial sediments at the former uranium mining leaching heap of Gessen/Thuringia, Germany. Chemie Der Erde - Geochemistry, 69(S2), 5-19.

Hallbeck, L., and Pedersen, K. (1990) Culture parameters regulating stalk formation and growth rate of *Gallionella ferruginea*. Journal of General Microbiology, 136, 1675-1680.

Hallbeck, L., Stahl, F., and Pedersen, K. (1993) Phylogeny and phenotypic characterization of the stalk-forming and iron-oxidizing bacterium *Gallionella ferruginea*. Journal of General Microbiology, 139, 1531-1535.

Hallberg, K.B. (2010) New perspectives in acid mine drainage microbiology. Hydrometallurgy, 104(3-4), 448-453.

Hallberg, K.B., Coupland, K., Kimura, S., and Johnson, D.B. (2006) Macroscopic streamer growths in acidic, metal-rich mine waters in North Wales consist of novel and remarkably simple bacterial communities. Applied and Environmental Microbiology, 72(3), 2022-2030.

Hallberg, K.B., and Johnson, D.B. (2005) Microbiology of a wetland ecosystem constructed to remediate mine drainage from a heavy metal mine. Science of the Total Environment, 338(1-2), 53-66.

Haller, L., Tonolla, M., Zopfi, J., Peduzzi, R., Wildi, W., and Pote, J. (2011) Composition of bacterial and archaeal communities in freshwater sediments with different contamination levels (Lake Geneva, Switzerland). Water Research, 45(3), 1213-1228.

Hanert, H.H. (2006) The Genus *Gallionella*. In A. Balows, H.G. Trüper, M. Dworkin, W. Harder, and K.H. Schleifer, Eds. The Prokaryotes, p. 990-995. Springer-Verlag, New York, USA.

He, Z.G., Xiao, S.M., Xie, X.H., Zhong, H., Hu, Y.H., Li, Q.H., Gao, F.L., Li, G.Y., Liu, J.S., and Qiu, G.Z. (2007) Molecular diversity of microbial community in acid mine drainages of Yunfu sulfide mine. Extremophiles, 11(2), 305-314.

Hochella Jr., M.F., Moore, J.N., Golla, U., and Putnis, A. (1999) A TEM study of samples from acid mine drainage systems: Metal-mineral association with implications for transport. Geochimica et Cosmochimica Acta, 63(19-20), 3395-3406.

Holmes, D.E., O'Neil, R.A., Vrionis, H.A., N'Guessan, L.A., Ortiz-Bernad, I., Larrahondo, M.J., Adams, L.A., Ward, J.A., Nicoll, J.S., Nevin, K.P., Chavan, M.A., Johnson, J.P., Long, P.E., and Lovley, D.R. (2007) Subsurface clade of *Geobacteraceae* that predominates in a diversity of Fe(III)-reducing subsurface environments. ISME Journal, 1(8), 663-677.

Hutchins, P.R., Smith, E.M., Koepfler, E.T., Viso, R.F., and Peterson, R.N. (2014) Metabolic responses of estuarine microbial communities to discharge of surface runoff and groundwater from contrasting landscapes. Estuaries and Coasts, 37, 736-750.

IAEA. (2014), available online at: http://www.iaea.org/NewsCenter/Features/DU/du_qaa.shtml. International Atomic Energy Agency.

Jiang, H.C., Dong, H.L., Yu, B.S., Liu, X.Q., Li, Y.L., Ji, S.S., and Zhang, C.L.L. (2007) Microbial response to salinity change in Lake Chaka, a hypersaline lake on Tibetan plateau. Environmental Microbiology, 9(10), 2603-2621.

Johnson, C.A., Freyer, G., Fabisch, M., Caraballo, M.A., Küsel, K., and Hochella, J., M. F. (2014a) Observations and assessment of iron oxide and green rust nanoparticles in metal-polluted mine drainage within a steep redox gradient. Environmental Chemistry, 11, 377-391.

Johnson, D.B. (2009) Extremophiles (overview): acid environments. In M. Schaechter, Ed. Encyclopedia of Microbiology, 3, p. 107-126. Elsevier Inc., Oxford, UK.

Johnson, D.B., Hallberg, K.B., and Hedrich, S. (2014b) Uncovering a microbial enigma: Isolation and characterization of the streamer-generating, iron-oxidizing, acidophilic bacterium "*Ferrovum myxofaciens*". Applied and Environmental Microbiology, 80(2), 672-680.

Johnson, M., Zaretskaya, I., Raytselis, Y., Merezhuk, Y., McGinnis, S., and Madden, T.L. (2008) NCBI BLAST: a better web interface. Nucleic Acids Research, 36(Web Server issue), W5-W9.

Kato, S.G., Krepski, S., Chan, C., Itoh, T., and Ohkuma, M. (2014) *Ferriphaselus amnicola* gen. nov., sp. nov., a neutrophilic, stalk-forming, iron-oxidizing bacterium isolated from an iron-rich groundwater seep. International Journal of Systematic and Evolutionary Microbiology, 64, 921-925.

Kay, C.M., Rowe, O.F., Rocchetti, L., Coupland, K., Hallberg, K.B., and Johnson, D.B. (2013) Evolution of microbial "streamer" growths in an acidic, metal-contaminated stream draining an abandoned underground copper mine. Life, 3, 189-210.

Kouzuma, A., Kasai, T., Nakagawa, G., Yamamuro, A., Abe, T., and Watanabe, K. (2013) Comparative metagenomics of anode-associated microbiomes developed in rice paddy-field microbial fuel cells. PLoS ONE, 8(11), e77443.

Krepski, S.T., Hanson, T.E., and Chan, C.S. (2012) Isolation and characterization of a novel biomineral stalk-forming iron-oxidizing bacterium from a circumneutral groundwater seep. Environmental Microbiology, 14(7), 1671-1680.

Küsel, K., Roth, U., Trinkwalter, T., and Pfeiffer, S. (2001) Effect of pH on the anaerobic microbial cycling of sulfur in mining-impacted freshwater lake sediments. Environmental and Experimental Botany, 46(3), 213-223.

Lear, G., Niyogi, D., Harding, J., Dong, Y.M., and Lewis, G. (2009) Biofilm bacterial community structure in streams affected by acid mine drainage. Applied and Environmental Microbiology, 75(11), 3455-3460.

Liang, F.Y., Xiao, Y., and Zhao, F. (2013) Effect of pH on sulfate removal from wastewater using a bioelectrochemical system. Chemical Engineering Journal, 218, 147-153.

Lin, C.F., Larsen, E.I., Larsen, G.R., Cox, M.E., and Smith, J.J. (2012) Bacterially mediated iron cycling and associated biogeochemical processes in a subtropical shallow coastal aquifer: implications for groundwater quality. Hydrobiologia, 696(1), 63-76.

Lüdecke, C., Reiche, M., Eusterhues, K., Nietzsche, S., and Küsel, K. (2010) Acid-tolerant microaerophilic Fe(II)-oxidizing bacteria promote Fe(III)-accumulation in a fen. Environmental Microbiology, 12(10), 2814-2825.

Nevin, K.P., Holmes, D.E., Woodard, T.L., Hinlein, E.S., Ostendorf, D.W., and Lovley, D.R. (2005) *Geobacter bemidjiensis* sp. nov. and *Geobacter psychrophilus* sp. nov., two novel Fe(III)-reducing subsurface isolates. International Journal of Systematic and Evolutionary Microbiology, 55, 1667-1674.

OGewV. (2011) Oberflächengewässerverordnung (Surface Water Protection Ordinance). German Federal Ministry of Justice, available online at: http://www.gesetze-im-internet.de/ogewv/BJNR142900011.html.

Ohnuki, T., Sakamoto, F., Kozai, N., Ozaki, T., Yoshida, T., Narumi, I., Wakai, E., Sakai, T., and Francis, A.J. (2004) Mechanisms of arsenic immobilization in a biomat from mine discharge water. Chemical Geology, 212(3-4), 279-290.

Ona-Nguema, G., Carteret, C., Benali, O., Abdelmoula, M., Genin, J., and Jorand, F. (2004) Competitive formation of hydroxycarbonate green rust 1 versus hydroxysulphate green rust 2 in *Shewanella putrefaciens* cultures. Geomicrobiology Journal, 21(2), 79-90.

Opitz, S., Küsel, K., Spott, O., Totsche, K.U., and Herrmann, M. (2014) Oxygen availability and distance to surface environments determine community composition and abundance of ammonia-oxidizing prokaroytes in two superimposed pristine limestone aquifers in the Hainich region, Germany. FEMS Microbiology Ecology, in press.

Peine, A., Tritschler, A., Küsel, K., and Peiffer, S. (2000) Electron flow in an iron-rich acidic sediment - evidence for an acidity-driven iron cycle. Limnology and Oceanography, 45(5), 1077-1087.

Pitkanen, T., Karinen, P., Miettinen, I.T., Lettojarvi, H., Heikkila, A., Maunula, R., Aula, V., Kuronen, H., Vepsalainen, A., Nousiainen, L.-L., Pelkonen, S., and Heinonen-Tanski, H. (2011) Microbial contamination of groundwater at small community water supplies in Finland. AMBIO, 40(4), 377-390.

Ridgway, H.F., Means, E.G., and Olson, B.H. (1981) Iron bacteria in drinking-water distribution-systems - Elemental analysis of *Gallionella* stalks, using X-ray energy-dispersive microanalysis. Applied and Environmental Microbiology, 41(1), 288-297.

Roden, E.E., McBeth, J.M., Blothe, M., Percak-Dennett, E.M., Fleming, E.J., Holyoke, R.R., Luther, G.W., 3rd, Emerson, D., and Schieber, J. (2012) The microbial ferrous wheel in a neutral pH groundwater seep. Frontiers in Microbiology, 3, 172.

Rotaru, C., Woodard, T.L., Choi, S., and Nevin, K.P. (2012) Spatial heterogeneity of bacterial communities in sediments from an infiltration basin receiving highway runoff. Microbial Ecology, 64(2), 461-473.

Schink, B. (1984) Fermentation of 2,3-butanediol by *Pelobacter carbinolicus* sp. nov. and *Pelobacter propionicus* sp. nov., and evidence for propionate formation from C_2 compounds. Archives of Microbiology, 137(1), 33-41.

Schloss, P.D., Westcott, S.L., Ryabin, T., Hall, J.R., Hartmann, M., Hollister, E.B., Lesniewski, R.A., Oakley, B.B., Parks, D.H., Robinson, C.J., Sahl, J.W., Stres, B., Thallinger, G.G., Van Horn, D.J., and Weber, C.F. (2009) Introducing mothur: Open-source, platform-independent, community-supported software for describing and comparing microbial communities. Applied and Environmental Microbiology, 75(23), 7537-7541.

Singleton, D.R., Furlong, M.A., Rathbun, S.L., and Whitman, W.B. (2001) Quantitative comparisons of 16S rRNA gene sequence libraries from environmental samples. Applied and Environmental Microbiology, 67(9), 4374-4376.

Sogaard, E.G., Aruna, R., Abraham-Peskir, J., and Koch, C.B. (2001) Conditions for biological precipitation of iron by *Gallionella ferruginea* in a slightly polluted ground water. Applied Geochemistry, 16(9-10), 1129-1137.

Stumm, W., and Lee, G.F. (1961) Oxygenation of ferrous iron. Industrial and Engineering Chemistry, 53(2), 143-146.

Sung, W., and Morgan, J.J. (1980) Kinetics and product of ferrous iron oxygenation in aqueous systems. Environmental Science & Technology, 14(5), 561-568.

Suzuki, T., Hashimoto, H., Matsumoto, N., Furutani, M., Kunoh, H., and Takada, J. (2011) Nanometer-scale visualization and structural analysis of the inorganic/organic hybrid structure of *Gallionella ferruginea* twisted stalks. Applied and Environmental Microbiology, 77(9), 2877-2881.

Ueki, A., Akasaka, H., Suzuki, D., and Ueki, K. (2006) *Paludibacter propionicigenes* gen. nov., sp nov., a novel strictly anaerobic, Gram-negative, propionate-producing bacterium isolated from plant residue in irrigated rice-field soil in Japan. International Journal of Systematic and Evolutionary Microbiology, 56, 39-44.

Wallis, P.M., and Ladd, T.I. (1983) Organic biogeochemistry of groundwater at a mountain coal-mine. Geomicrobiology Journal, 3(1), 49-78.

Wang, J.J., Sickinger, M., Ciobota, V., Herrmann, M., Rasch, H., Rosch, P., Popp, J., and Küsel, K. (2014) Revealing the microbial community structure of clogging materials in dewatering wells differing in physico-chemical parameters in an open-cast mining area. Water Research, 63, 222-233.

Weiss, J.V., Rentz, J.A., Plaia, T., Neubauer, S.C., Merrill-Floyd, M., Lilburn, T., Bradburne, C., Megonigal, J.P., and Emerson, D. (2007) Characterization of neutrophilic Fe(II)-oxidizing bacteria isolated from the rhizosphere of wetland plants and description of *Ferritrophicum radicicola* gen. nov sp nov., and *Sideroxydans paludicola* sp nov. Geomicrobiology Journal, 24(7-8), 559-570.

WHO. (2011) Guidelines for drinking-water quality. World Health Organization Press, Geneva, Switzerland.

Williamson, M.A., Kirby, C.S., and Rimstidt, J.D. (2006) Iron dynamics in acid mine drainage. In R.I. Barnhisel, Ed. 7th International Conference on Acid Rock Drainage (ICARD). American Society of Mining and Reclamation (ASMR), St. Louis, MO, USA.

Wismut GmbH. (2006) Umweltbericht 2006 der Wismut GmbH, Chemnitz.

---------. (2011) Umweltbericht 2011 der Wismut GmbH, Chemnitz.

Wright, E.S., Yilmaz, L.S., and Noguera, D.R. (2012) DECIPHER, a search-based approach to chimera identification for 16S rRNA sequences. Applied and Environmental Microbiology, 78(3), 717-725.

Yu, R., Gan, P., MacKay, A.A., Zhang, S.L., and Smets, B.F. (2010) Presence, distribution, and diversity of iron-oxidizing bacteria at a landfill leachate-impacted groundwater surface water interface. FEMS Microbiology Ecology, 71(2), 260-271.

Zeien, H., and Brümmer, G.W. (1989) Chemische Extraktion zur Bestimmung von Schwermetallbindungsformen in Böden. Mitteling. Deutsche Bondenkundliche Gesellschaft, 59(1), 505-515.

Zhou, J.Z., Bruns, M.A., and Tiedje, J.M. (1996) DNA recovery from soils of diverse composition. Applied and Environmental Microbiology, 62(2), 316-322.

D.9. Tables

Table D.1. Geochemical data for water (w) and sediment (s) of sites I to III in the former uranium-mining district near Ronneburg at several time points in the years 2011 and 2012 with means over time and standard deviations in parentheses. Standard deviations given at individual time points were derived from measurements of field triplicate samples.

Sample	Time	Tempe-rature (°C)	pH	E_h (mV)	DO (mg L^{-1})	Electrical conductivity (mS cm^{-1})	Total Fe[a] (mmol L^{-1})	Fe(II)[b] (mmol L^{-1})	Dissolved sulfate (mmol L^{-1})	DOC (mg L^{-1})	Organic matter (% of gww)
Iw	June '11	ND	5.9	230	0.8	5.65	ND	ND	ND	ND	NA
	July '11	ND	ND[c]	ND[c]	ND[c]	ND[c]	5.90 (ND)	6.10 (0.06)[c]	41.8 (0.9)[c]	ND	NA
	Oct '11	12.0	5.8[c]	260[c]	0.6[c]	5.54[c]	5.69 (0.05)	5.64 (0.03)[c]	40.0 (8.6)[c]	4.8	NA
	Dec '11	13.8	6.2	257	4.1	5.2	3.74 (1.16)	4.22 (0.07)	42.2 (1.3)	ND	NA
	April '12	13.1	5.9	229	1.1	4.9	ND	ND	ND	ND	NA
	Mean	**13.0 (1.0)**	**6.0 (0.2)**	**244 (17)**	**1.7 (1.6)**	**5.32 (0.34)**	**5.11 (1.19)**	**5.32 (0.98)**	**41.3 (1.2)**	**4.8**	**NA**
IIw	June '11	19.2	6.2	325	7.7	5.34	3.77 (0.31)	4.15 (0.03)	38.9 (10.9)	5.6	NA
	July '11	16.0	5.8[c]	ND[c]	ND[c]	5.39[c]	5.36 (0.19)	5.85 (0.16)[c]	44.8 (1.2)[c]	4.8	NA
	Oct '11	13.2	6.3[c]	280[c]	8.5[c]	5.23[c]	4.35 (0.32)	4.64 (0.08)[c]	33.4 (1.8)[c]	5.9	NA
	Dec '11	13.2	6.2	248	5.5	5.17	3.40 (0.62)	4.14 (0.04)	39.5 (1.8)	ND	NA
	April '12	12.2	6.1	231	9.7	5.1	ND	ND	ND	ND	NA
	Mean	**14.8 (2.9)**	**6.1 (0.2)**	**271 (41)**	**7.9 (1.8)**	**5.25 (0.12)**	**4.22 (0.86)**	**4.70 (0.80)**	**39.2 (4.7)**	**5.4 (0.5)**	**NA**
IIIw	June '11	16.3	6.0	369	5.0	5.11	4.66 (0.53)	4.10 (0.25)	44.4 (0.6)	5.2	NA
	July '11	15.7	5.8[c]	ND[c]	ND[c]	4.80[c]	3.62 (0.16)	3.83 (0.43)[c]	39.1 (2.0)[c]	5.4	NA
	Oct '11	11.4	6.1[c]	307[c]	5.0[c]	4.81[c]	3.82 (0.03)	3.88 (0.13)[c]	33.4 (2.6)[c]	5.5	NA
	Dec '11	12.1	6.0	305	4.9	4.9	3.31 (0.78)	3.85 (0.07)	36.8 (2.6)	ND	NA
	April '12	13.6	6.2	260	4.4	4.7	ND	ND	ND	ND	NA
	Mean	**13.8 (2.2)**	**6.0 (0.1)**	**310 (45)**	**4.8 (0.3)**	**4.86 (0.15)**	**3.85 (0.58)**	**3.92 (0.12)**	**38.4 (4.6)**	**5.4 (0.2)**	**NA**
IIs	June '11	19.9	3.7	475	NA	ND	ND	ND	ND	NA	4.1 (0.5)
	July '11	ND	5.6[c]	ND	NA	5.33[c]	3111 (212)	49 (20)	31.9 (5.3)	NA	3.2 (0.7)
	Oct '11	13.8	4.8[c]	417	NA	4.18[c]	5191 (26)	187 (11)	40.4 (ND)	NA	4.0 (0.2)
	Dec '11	ND	4.5	464	NA	ND	ND	58 (5)	55.4 (1.0)	NA	5.8 (3.1)
	April '12	10.1	3.8	452	NA	4.2	ND	ND	ND	NA	ND
	Mean	**14.6 (5.0)**	**4.5 (0.8)**	**452 (25)**	**NA**	**4.57 (0.66)**	**4151**	**98 (77)**	**42.6 (11.9)**	**NA**	**4.3 (1.1)**
IIIs	June '11	16.9	5.4	257	NA	ND	ND	ND	ND	NA	2.69 (0.04)
	July '11	ND	5.5[c]	ND	NA	4.62[c]	996 (2)	39 (11)	30.7 (4.6)	NA	1.22 (0.01)
	Oct '11	12.8	5.6[c]	306	NA	4.1[c]	2264 (15)	137 (28)	40.4 (2.6)	NA	1.9 (0.1)
	Dec '11	ND	5.9	253	NA	ND	ND	71 (14)	49.3 (4.2)	NA	4.4 (0.5)
	April '12	12.6	6.0	290	NA	4.7	ND	ND	ND	NA	ND
	Mean	**14.1 (2.4)**	**5.7 (0.3)**	**276 (26)**	**NA**	**4.47 (0.33)**	**1630**	**83 (50)**	**40.1 (9.3)**	**NA**	**2.5 (1.4)**

[a] Total Fe was measured by ICP-MS. In water it represents total dissolved iron (0.45 μm filtered in June, July, and Oct; 0.2 μm in Dec).

[b] Fe(II) was measured by the phenanthroline method after HCl extraction. In water it represents dissolved Fe(II) (0.2 μm filtered).
[c] Previously published in the parallel study by Johnson et al. (2014a).
E_h, redox potential. DO, dissolved oxygen. DOC, dissolved organic carbon. gww, gram wet weight. ND, not determined. NA, not applicable.

Table D.2. Fractions of clone sequences (%) with ≥97% sequence identity to their nearest isolated FeOB or other relative in bacterial 16S rRNA gene clone libraries constructed from water (w) and sediment (s) of sites I-III in the former Ronneburg uranium-mining district, as well as pH tolerance and environmental occurrence of the known microorganisms. For the FeOB '*Gallionella capsiferriformans*' and *Gallionella ferruginea*, the fractions of clone sequences with ≥99% SI are additionally shown in parentheses. Sums of FeOB are not always equal to the sum of the individual percentages due to rounding of values.

Organism, SI (Genbank accession; affiliation)	**Iw**	**IIw**	**IIIw**	**IIs**	**IIIs**	**pH tolerance[$]**	**Environmental occurrence[§]**
FeOB	**57**	**21**	**24**	**22**	**75**		
'*Gallionella capsiferriformans* ES-2', 97–99% (≥99% SI) (DQ386262; β-*Proteobacteria*)	55 (1)	21 (1)	17 (-)	22 (13)	75 (10)	Neutrophilic (5.5–7.5)[a]	Freshwater (e.g., groundwater, iron seep)[a,b]; organically contaminated soil, AMD[c]
Gallionella ferruginea, 97–99% (≥99% SI) (L07897; β-*Proteobacteria*)	2 (-)	-[#] (-)	5 (2)	- (-)	- (-)	Neutrophilic (5.0–7.6)[d]	Freshwater (springs, wells, drainages, groundwater seep, river sediment)[e]; AMD[f]
Sideroxydans sp. strain CL21, 99% (GU134935; β-*Proteobacteria*)	-	-	1	-	-	Moderately acidophilic (4.0–6.0)[g]	Minerotrophic fen[g], acidic lakes[h]; metal-contaminated soil and creek sediment[i]
Gallionellaceae bacterium R-1, 98% (JN377592; β-*Proteobacteria*)	-	-	1	-	-	Neutrophilic (5.6–7.0)[j]	Groundwater iron seep[j]
Others*							
Geobacter psychrophilus[T], 97–99% (AY653549; δ-*Proteobacteria*, FeRB)	7	10	7	-	-	Neutrophilic (6.0–9.0)[k]	Pristine and contaminated freshwater habitats[k,m]
Geobacter bemidjiensis[T], 97% (AY187307; δ-*Proteobacteria*, FeRB)	-	1	-	-	-	Neutrophilic (7.0)[k]	Contaminated groundwater and soil (petroleum, heavy metals)[k,n]
Geothrix fermentans[T], 97–99% (U41563; *Acidobacteria*, FeRB)	-	1	-	-	-	Not determined[o]	Contaminated aquifers and soils (hydrocarbons, U)[o,p]
Paludibacter propionicigenes[T], 97% (NR_074577; *Bacteroidetes*, fermentation[q])	-	3	-	-	-	Neutrophilic (5.0–7.6)[q]	Rice field soil[q]; wastewater[r]; animal gut[s]
Bacterium TP701, 99% (EF636141; β-*Proteobacteria*)	2	-	-	1	-	Not determined	Freshwater pond sediment[t]
Thiomonas sp. DM-Zn2, 98% (DQ419967; β-*Proteobacteria*)	-	1	-	1	-	Not determined	AMD[u]
Pelobacter propionicus[T], 97% (NR_074975; δ-*Proteobacteria*, fermentation[v])	-	-	2	-	-	Neutrophilic (6.5–8.4)[v]	Anoxic freshwater mud, anaerobic sewage sludge digesters[v], rice field soil[w]
Desulfosporosinus sp. LauIII, 97% (AJ302078; *Firmicutes*, sulfate-reducer[x])	-	-	2	-	-	Moderately acidophilic (4.9–6.1)[x]	Mining-impacted lake sediment[x], AMD sediment[y]; hypersaline lake sediment[z]

[$] pH tolerance represents reported pH tolerance, or assumed pH tolerance based on the reported pH range for iron oxidation or reduction. The pH growth range is given in parentheses.
[§] Environmental occurrence refers to the source of isolation and/or detection with molecular methods.
[#] - indicates that no clone sequence was detected with the respective organism as the nearest cultured relative.
* Other relatives include FeRB, and other organisms with at least 2 detected clones from all five libraries.

References for metabolism, pH, and occurrence: [a] (Emerson et al., 2013; Emerson and Moyer, 1997); [b] (Roden et al., 2012); [c] (Bruneel et al., 2011; Rotaru et al., 2012); [d] (Hallbeck et al., 1993; Hanert, 2006); [e] (Bruun et al., 2010; Hanert, 2006; Yu et al., 2010); [f] (Bruneel et al., 2006; Fabisch et al., 2013; He et al., 2007; Lear et al., 2009); [g] (Lüdecke et al., 2010); [h] (GenBank accessions EF520447, FR667790); [i] (GenBank accession AJ582038; Fabisch et al., 2013); [j] (Krepski et al., 2012); [k] (Nevin et al., 2005); [m] (Bruun et al., 2010; Burkhardt et al., 2011; Haller et al., 2011); [n] (Burkhardt et al., 2010; Holmes et al., 2007); [o] (Coates et al., 1999); [p] (Brodie et al., 2006); [q] (Ueki et al., 2006); [r] (Liang et al., 2013); [s] (Ceja-Navarro et al., 2014); [t] (Bollmann et al., 2007); [u] (GenBank accession DQ419967); [v] (Schink, 1984); [w] (Kouzuma et al., 2013); [x] (Küsel et al., 2001); [y] (Garcia-Moyano et al., 2012); [z] (Jiang et al., 2007).
SI, sequence identity. FeOB, iron-oxidizing bacteria. FeRB, iron-reducing bacteria. AMD, acid mine drainage.

Table D.3. Copy numbers of the 16S rRNA gene of different organism groups in water (w) or sediment (s) of sites I to III as determined by qPCR with group-specific primer sets. Given are means (with standard deviations in parentheses) of triplicate measurements in copy numbers per mL of water or in copy numbers per gww sediment.

Sample	Time	*Archaea*	*Bacteria*	*Gallionella* spp.	*Sideroxydans* spp.	'*Ferrovum myxofaciens*'	*Geobacter* spp.	*Albidoferax ferrireducens*
Iw	June	$9.0x10^3$ ($0.6x10^3$)	$3.1x10^5$ ($0.1x10^5$)	$6.5x10^4$ ($0.3x10^4$)	$5.9x10^3$ ($0.7x10^3$)	$7.3x10^2$ ($1.2x10^2$)	$1.6x10^3$ ($0.2x10^3$)	$4.1x10^4$ ($0.1x10^4$)
	July	$6.5x10^4$ ($0.5x10^4$)	$5.4x10^6$ ($0.3x10^6$)	$2.04x10^6$ ($0.04x10^6$)	$9.6x10^3$ ($0.7x10^3$)	$9.7x10^3$ ($0.2x10^3$)	$9.97x10^6$ ($0.03x10^6$)	$5.1x10^5$ ($0.3x10^5$)
	Oct	$7.3x10^3$ ($0.2x10^3$)	$3.7x10^5$ ($0.5x10^5$)	$1.3x10^5$ ($0.1x10^5$)	$3.2x10^2$ ($0.8x10^2$)	$3.4x10^2$ ($0.2x10^2$)	$1.7x10^4$ ($0.2x10^4$)	$2.3x10^4$ ($0.1x10^4$)
	Dec	$1.9x10^4$ ($0.1x10^4$)	$1.0x10^6$ ($0.2x10^6$)	$4.2x10^5$ ($0.2x10^5$)	$3.8x10^3$ ($0.1x10^3$)	$1.9x10^3$ ($0.1x10^3$)	$3.4x10^4$ ($0.2x10^4$)	$6.6x10^4$ ($0.3x10^4$)
	Mean	**$2.5x10^4$ ($2.7x10^4$)**	**$1.8x10^6$ ($2.5x10^6$)**	**$6.6x10^5$ ($9.3x10^5$)**	**$4.9x10^3$ ($3.9x10^3$)**	**$3.2x10^3$ ($4.4x10^3$)**	**$2.6x10^5$ ($4.9x10^5$)**	**$1.6x10^5$ ($2.4x10^5$)**
IIw	June	$9.0x10^3$ ($1.2x10^3$)	$2.7x10^6$ ($0.3x10^6$)	$1.45x10^6$ ($0.02x10^6$)	$2.5x10^4$ ($0.1x10^4$)	$1.1x10^5$ ($0.1x10^5$)	$3.7x10^4$ ($0.4x10^4$)	$7.8x10^4$ ($0.8x10^4$)
	July	$6.7x10^4$ ($0.3x10^4$)	$1.4x10^7$ ($0.1x10^7$)	$2.5x10^6$ ($0.1x10^6$)	$1.4x10^5$ ($0.1x10^5$)	$8.3x10^4$ ($0.3x10^4$)	$1.8x10^6$ ($0.1x10^6$)	$9.4x10^5$ ($0.4x10^5$)
	Oct	$8.7x10^3$ ($0.1x10^3$)	$1.7x10^6$ ($0.1x10^6$)	$5.2x10^5$ ($0.1x10^5$)	$4.3x10^3$ ($0.2x10^3$)	$4.2x10^3$ ($0.3x10^3$)	$2.8x10^5$ ($0.2x10^5$)	$1.3x10^5$ ($0.1x10^5$)
	Dec	$1.6x10^4$ ($0.2x10^4$)	$1.3x10^6$ ($0.2x10^6$)	$3.3x10^5$ ($0.8x10^5$)	$2.5x10^3$ ($0.1x10^3$)	$1.5x10^3$ ($0.1x10^3$)	$6.3x10^4$ ($0.7x10^4$)	$8.0x10^4$ ($0.2x10^4$)
	Mean	**$2.5x10^4$ ($2.8x10^4$)**	**$4.9x10^6$ ($6.0x10^6$)**	**$1.2x10^6$ ($1.0x10^6$)**	**$4.4x10^4$ ($6.7x10^4$)**	**$4.9x10^4$ ($5.4x10^4$)**	**$5.4x10^5$ ($8.3x10^5$)**	**$3.1x10^5$ ($4.2x10^5$)**
IIIw	June	$5.3x10^2$ ($0.3x10^2$)	$8.5x10^4$ ($0.5x10^4$)	$2.08x10^4$ ($0.04x10^4$)	$1.4x10^3$ ($0.1x10^3$)	$5.0x10^3$ ($0.3x10^3$)	$1.95x10^3$ ($0.04x10^3$)	$3.9x10^3$ ($0.4x10^3$)
	July	$2.2x10^4$ ($0.2x10^4$)	$2.2x10^6$ ($0.2x10^6$)	$4.2x10^5$ ($0.2x10^5$)	$1.71x10^4$ ($0.04x10^4$)	$7.5x10^4$ ($0.9x10^4$)	$1.4x10^5$ ($0.1x10^5$)	$9.7x10^4$ ($0.3x10^4$)
	Oct	$2.7x10^4$ ($0.8x10^4$)	$2.6x10^6$ ($0.3x10^6$)	$8.3x10^5$ ($0.6x10^5$)	$1.6x10^4$ ($0.1x10^4$)	$3.8x10^4$ ($0.1x10^4$)	$1.5x10^5$ ($0.1x10^5$)	$1.27x10^5$ ($0.03x10^5$)
	Mean	**$1.7x10^4$ ($1.4x10^4$)**	**$1.6x10^6$ ($1.3x10^6$)**	**$4.3x10^5$ ($4.1x10^5$)**	**$1.1x10^4$ ($0.9x10^4$)**	**$3.9x10^4$ ($3.5x10^4$)**	**$9.7x10^4$ ($8.2x10^4$)**	**$7.6x10^4$ ($6.4x10^4$)**
Is	Dec	$3.4x10^6$ ($0.1x10^6$)	$1.1x10^9$ ($0.1x10^9$)	$3.1x10^8$ ($0.2x10^8$)	$8.8x10^5$ ($0.5x10^5$)	$9.8x10^5$ ($1.7x10^5$)	$7.4x10^7$ ($0.4x10^7$)	$7.6x10^7$ ($0.2x10^7$)
IIs	June	$1.4x10^5$ ($0.2x10^5$)	$1.2x10^8$ ($0.1x10^8$)	$4.1x10^7$ ($0.1x10^7$)	$3.7x10^6$ ($0.6x10^6$)	$5.1x10^6$ ($0.2x10^6$)	$3.2x10^6$ ($0.3x10^6$)	$3.0x10^6$ ($0.2x10^6$)
	July	$9.8x10^6$ ($0.4x10^6$)	$8.3x10^9$ ($1.3x10^9$)	$3.2x10^9$ ($0.2x10^9$)	$2.4x10^7$ ($0.2x10^7$)	$8.7x10^6$ ($1.1x10^6$)	$5.93x10^8$ ($0.02x10^8$)	$1.5x10^9$ ($0.1x10^9$)
	Oct	$3.5x10^6$ ($0.1x10^6$)	$2.2x10^9$ ($0.1x10^9$)	$2.9x10^8$ ($0.1x10^8$)	$7.9x10^7$ ($0.7x10^7$)	$2.2x10^7$ ($0.2x10^7$)	$2.3x10^8$ ($0.1x10^8$)	$9.6x10^7$ ($0.2x10^7$)
	Dec	$3.3x10^4$ ($0.2x10^4$)	$5.6x10^7$ ($0.2x10^7$)	$4.2x10^7$ ($0.5x10^7$)	$3.4x10^5$ ($0.1x10^5$)	$9.8x10^4$ ($0.2x10^4$)	$1.2x10^6$ ($0.1x10^6$)	$1.3x10^6$ ($0.1x10^6$)
	Mean	**$3.4x10^6$ ($4.6x10^6$)**	**$2.7x10^9$ ($3.9x10^9$)**	**$8.9x10^8$ ($15.3x10^8$)**	**$2.6x10^7$ ($3.6x10^7$)**	**$9.0x10^6$ ($9.5x10^6$)**	**$2.1x10^8$ ($2.8x10^8$)**	**$3.9x10^8$ ($7.1x10^8$)**
IIIs	June	$4.4x10^6$ ($0.2x10^6$)	$2.1x10^9$ ($0.1x10^9$)	$6.6x10^8$ ($0.5x10^8$)	$8.7x10^7$ ($0.8x10^7$)	$1.3x10^7$ ($0.1x10^7$)	$9.3x10^7$ ($0.7x10^7$)	$2.4x10^8$ ($0.1x10^8$)
	July	$2.4x10^6$ ($0.3x10^6$)	$7.6x10^9$ ($0.7x10^9$)	$6.1x10^9$ ($0.2x10^9$)	$4.5x10^6$ ($0.2x10^6$)	$1.2x10^7$ ($0.1x10^7$)	$6.6x10^7$ ($0.6x10^7$)	$9.0x10^8$ ($0.9x10^8$)
	Oct	$1.5x10^6$	$6.6x10^9$	$5.9x10^9$	$1.1x10^6$	$4.2x10^6$	$7.8x10^7$	$8.2x10^7$

	($0.1x10^6$)	($0.4x10^9$)	($0.3x10^9$)	($0.1x10^6$)	($0.2x10^6$)	($0.8x10^7$)	($0.3x10^7$)
Dec	$7.6x10^4$ ($0.5x10^4$)	$6.2x10^7$ ($0.5x10^7$)	$3.2x10^7$ ($0.1x10^7$)	$3.7x10^4$ ($0.7x10^4$)	$1.1x10^5$ ($0.1x10^5$)	$8.0x10^5$ ($0.4x10^5$)	$3.6x10^6$ ($0.2x10^6$)
Mean	**$2.1x10^6$ ($1.8x10^6$)**	**$4.1x10^9$ ($3.6x10^9$)**	**$3.2x10^9$ ($3.3x10^9$)**	**$2.3x10^7$ ($4.3x10^7$)**	**$7.2x10^6$ ($6.1x10^6$)**	**$5.9x10^7$ ($4.1x10^7$)**	**$3.1x10^8$ ($4.1x10^8$)**

D.10. Figures

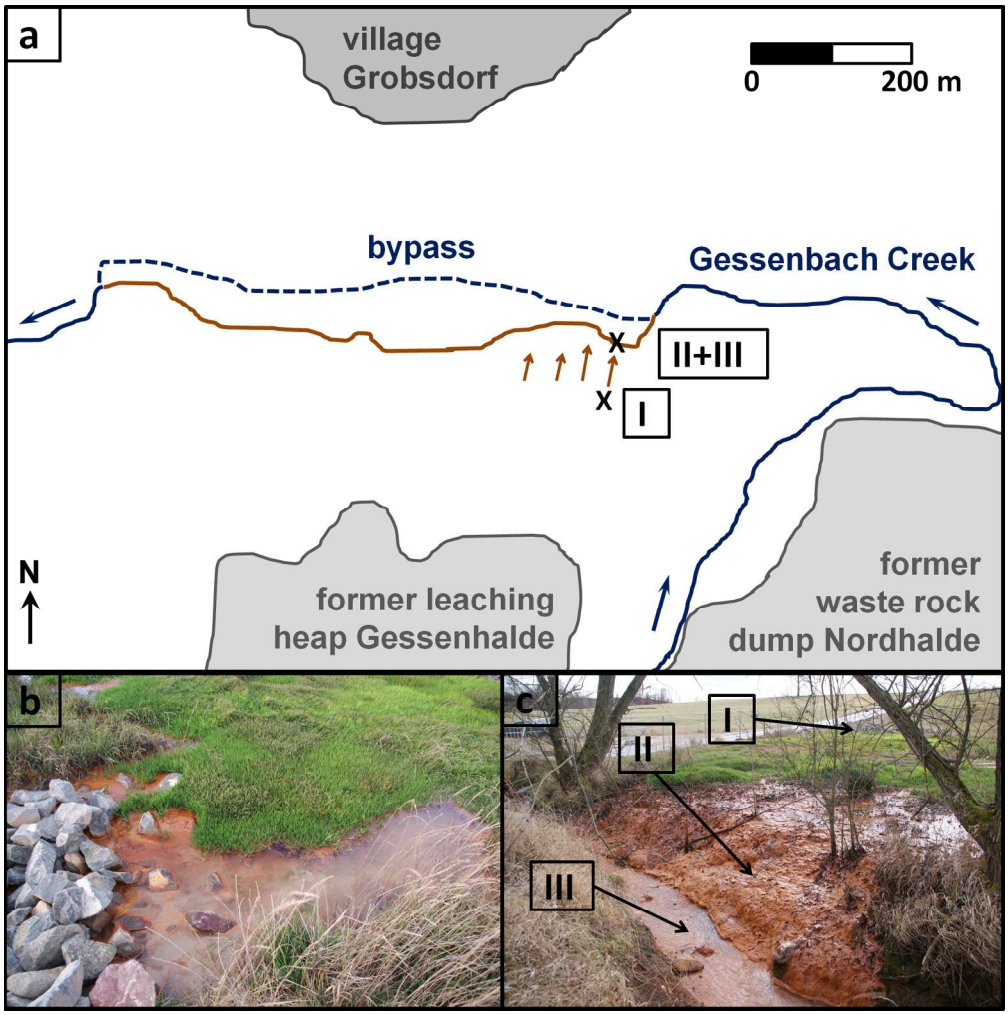

Figure D.1. Schematic map (a) and photographs (b-c) of the field sites I to III located in the former Ronneburg uranium-mining district (Thuringia, Germany). (a) Map showing the positions of sites I to III in the contaminated part of the creek (brown). Blue arrows give the flow direction of the creek, while brown arrows give the flow direction of the discharged water from the seeps. Map was modified from Fabisch et al. (2013). (b) Photograph of site I (outflow) in December 2011. (c) Photograph of the terraces in December 2011 with sites I to III indicated by arrows.

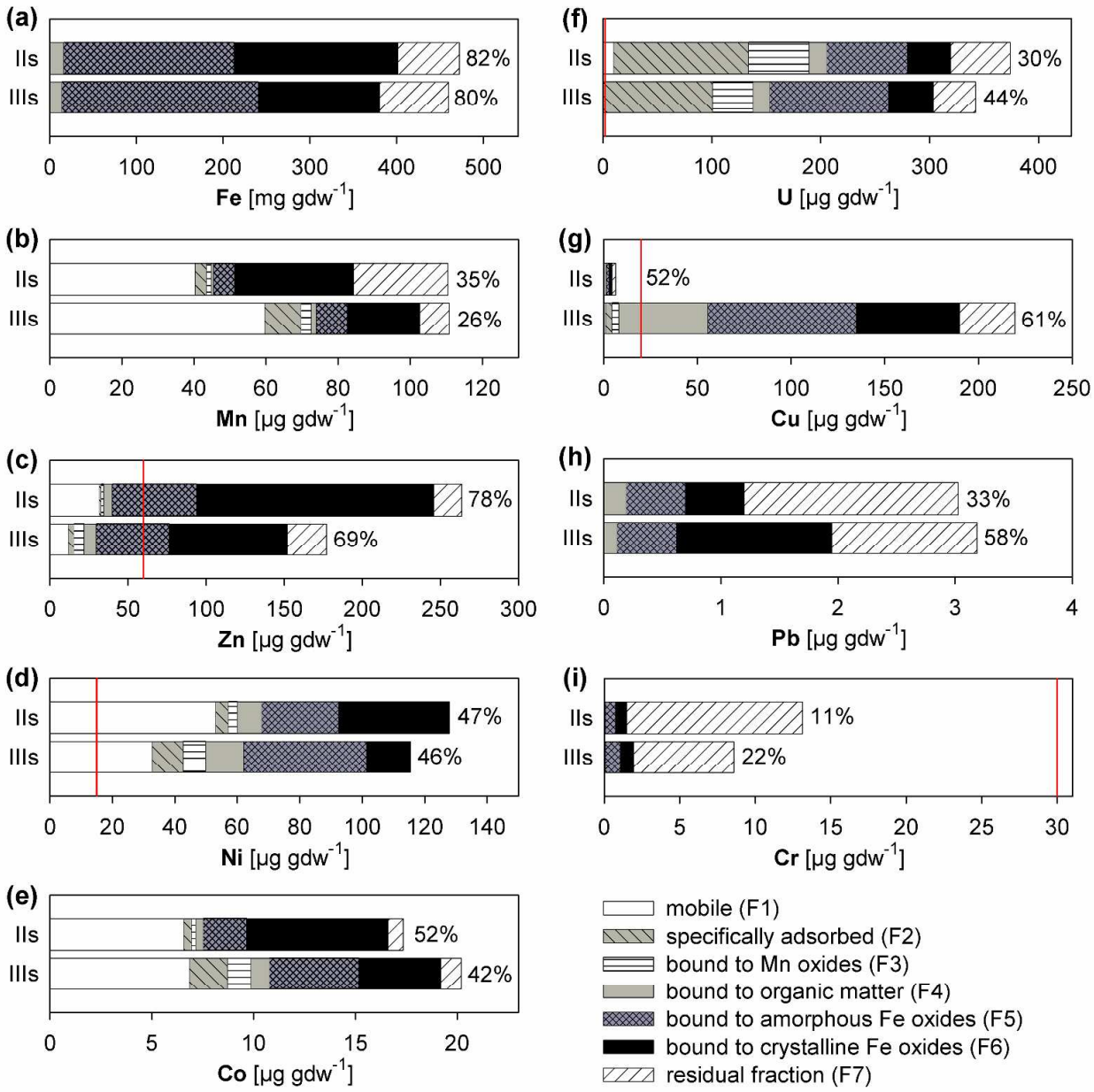

Figure D.2. Concentrations of the metals Fe (a), Mn (b), Zn (c), Ni (d), Co (e), U (f), Cu (g), Pb (h), and Cr (i) in different fractions (F1-F7) of sediment from sites II (IIs) and III (IIIs) in July 2011 in the former uranium-mining district Ronneburg, obtained by sediment sequential extraction and measurement by ICP-MS and -OES. The percentages on the right side of the bars represent the proportion of the total metal content bound to the amorphous and crystalline Fe oxide fractions (F5+F6). Red lines within a graph represent the German soil precautionary values (BBodSchV, 1999) or U background soil level (IAEA, 2014). gdw, gram dry weight.

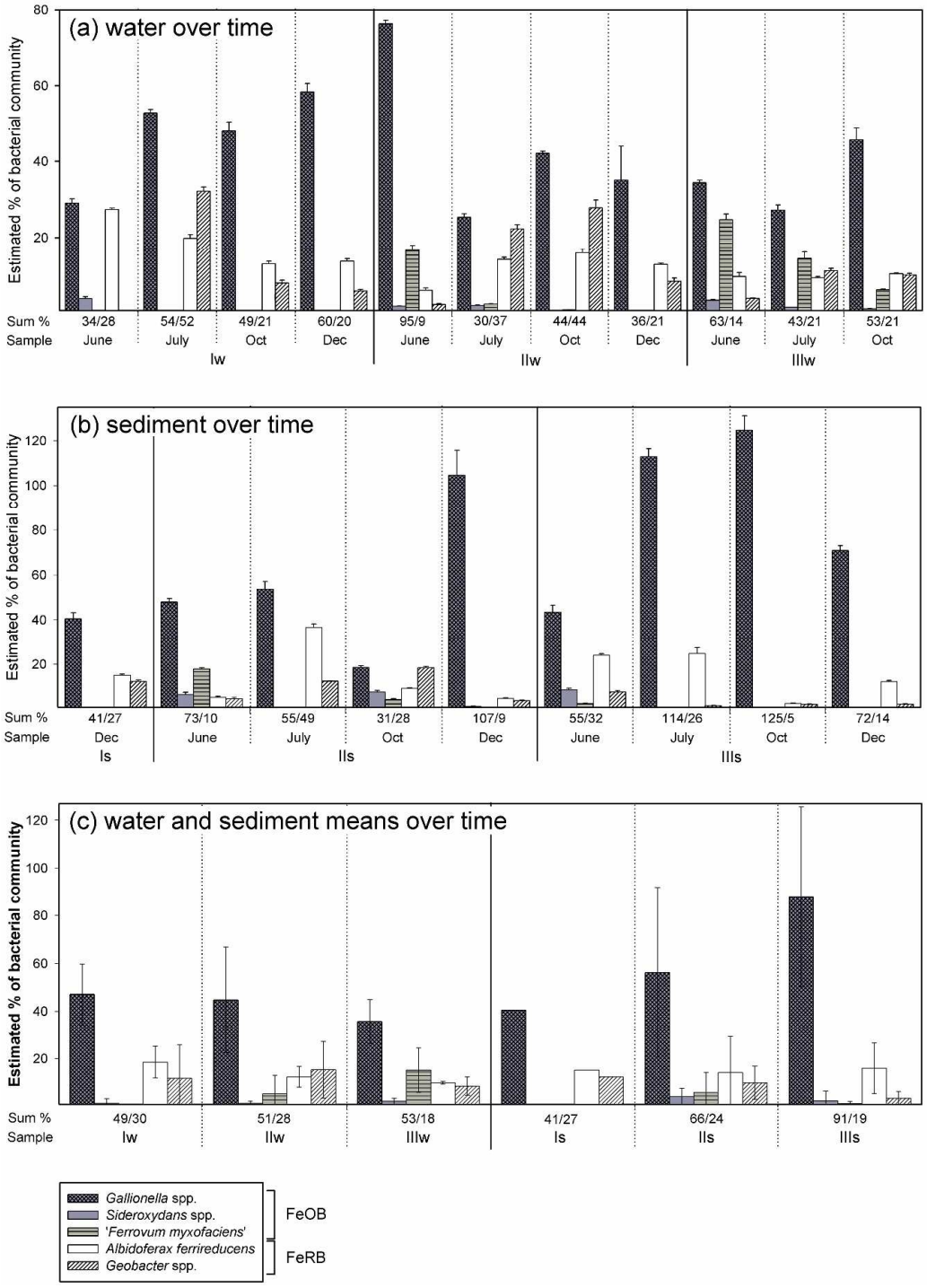

Figure D.3. Estimated percentages of the bacterial communities in water (w) or sediment (s) of sites I to III of different FeOB and FeRB groups. Given are means with standard deviations for each sample at several time points in the year 2011 for water (a) and sediment (b) samples. Means over time of each water and sediment sample are presented in (c). The percentages were estimated based on 16S rRNA gene copy numbers, as determined by triplicate qPCR measurements with group-specific primer sets. The values between the x axis and sample designation represent the sum of the percentages of the various FeOB and FeRB groups (Sum% FeOB / Sum% FeRB) in the respective community, demonstrating the minimum part of the bacterial community related to known FeOB or FeRB.

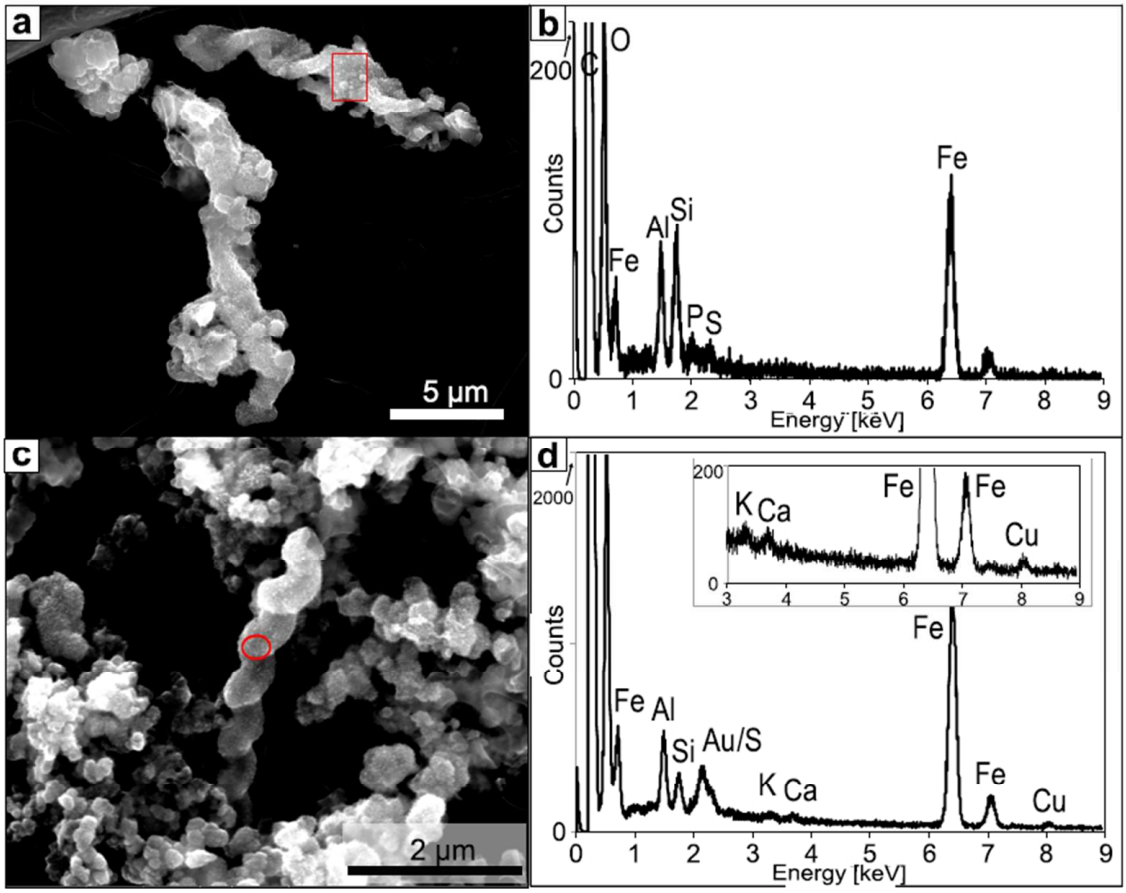

Figure D.4. SEM images and EDS spectra of *Gallionella*-like twisted stalks (EDS areas indicated in red outlines) deposited on glass slides, which were placed in water of site I (a-b) or III (c-d) for 5 weeks. The stalk analyzed in (a) is the same as in Figure 5, though the trace metals Cu and Sn were not visible by SEM-EDS. However, Cu associated with the stalk in (c) was detected by SEM-EDS as shown in (d). The stalks share a similar composition of Fe, O, Si, and trace S and P. Al signals come from the aluminum holder that the sample is mounted on.

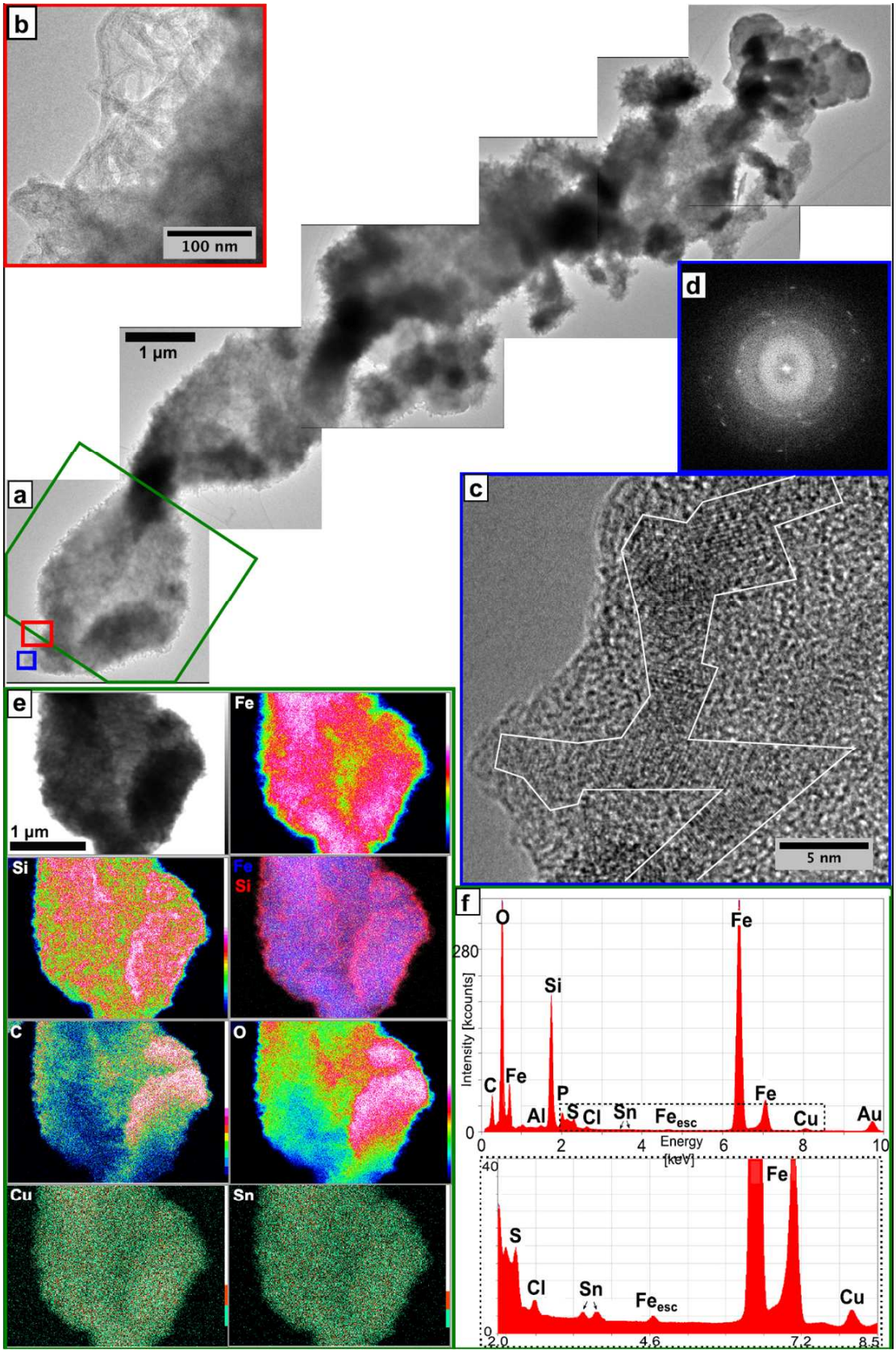
b
100 nm
1 µm
d
a
c
5 nm
e
Fe
1 µm
Si
Fe
Si
C
O
Cu
Sn
f
O
Fe
Si
C
Fe
P
Al
S
Cl
Sn
Fe_esc
Fe
Cu
Au
Intensity [kcounts]
Energy [keV]
Fe
S
Cl
Sn
Fe_esc
Cu

Figure D.5. Transmission electron microscopy of *Gallionella*-like twisted stalks from outflow water (Iw). (a) Composite image of a stalk with many attached iron oxides. Red, blue and green boxes indicate areas (b)-(f), respectively. (b) Medium range image. (c) High resolution image used to match structural d-spacings with known iron oxide structures, with "filaments" of crystalline iron oxides outlined. (d) FFT pattern of (c). (e) STEM-EDS mapping of part of the stalk with elements Fe, Si, Fe and Si overlay, C, O, Cu, and Sn. (f) TEM-EDS full spectrum of the *Gallionella*-like stalk area mapped in (e). Both heavy metals Cu and Sn are present in trace amounts.

APPENDIX E: SUPPLEMENTAL MATERIAL FOR APPENDIX D

Dominance of '*Gallionella capsiferriformans*' and Heavy Metal Retention By Stalk-Forming Iron Oxidizers in Metal-Rich Mine Water Discharge

Maria Fabisch, Gina Freyer, Carol A. Johnson, Georg Büchel, Denise M. Akob, Kirsten Küsel

Table E.1. Concentrations of dissolved heavy metals in water at sites I, II, and III at different time points in 2011 and their means over time (with standard deviations in parentheses).

Sample	Time	Mn (μmol L^{-1})	Zn (μmol L^{-1})	Ni (μmol L^{-1})	Co (μmol L^{-1})	U (μmol L^{-1})	Cu (nmol L^{-1})	Pb (nmol L^{-1})	Cd (nmol L^{-1})	Cr (nmol L^{-1})
Iw	July '11	200.4 (ND)	22.9 (ND)	48.5 (ND)	13.5 (ND)	0.47 (ND)	57 (ND)	BD	33.7 (ND)	4.52 (ND)
	Oct '11	240.9 (0.3)	20.1 (0.3)	40.3 (0.1)	12.7 (0.1)	0.45 (0.01)	224 (193)	0.79 (0.25)	31.6 (1.5)	BD
	Dec '11	216.4 (5.0)	14.3 (0.9)	31.8 (0.7)	10.37 (0.02)	0.30 (0.32)	24.2 (2.3)	BD	23.9 (0.3)	BD
	Mean	**219.2 (20.4)**	**19.1 (4.4)**	**40.2 (8.4)**	**12.2 (1.6)**	**0.40 (0.09)**	**102 (107)**	**NA**	**29.7 (5.2)**	**NA**
IIw	June '11	175.7 (15.2)	22.5 (6.1)	38.0 (3.0)	11.1 (0.9)	0.55 (0.05)	72 (32)	1.8 (0.8)	22.8 (3.9)	BD
	July '11	188.8 (8.7)	16.9 (0.6)	45.3 (2.7)	10.8 (0.6)	0.57 (0.01)	104 (4)	0.97 (0.48)	17.7 (3.2)	12.0 (5.4)
	Oct '11	203.1 (15.9)	7.0 (0.3)	33.1 (2.9)	9.3 (0.8)	0.40 (0.07)	21 (1)	BD	2.1 (0.3)	BD
	Dec '11	208.5 (5.7)	7.0 (2.0)	27.5 (1.6)	8.8 (0.5)	0.22 (0.16)	18.9 (0.0)	BD	6.0 (2.1)	BD
	Mean	**194.0 (14.8)**	**13.4 (7.7)**	**36.0 (7.6)**	**10.0 (1.1)**	**0.43 (0.16)**	**54 (41)**	**NA**	**12.2 (9.7)**	**NA**
IIIw	June '11	282.6 (39.7)	29.9 (20.8)	38.3 (4.8)	15.2 (2.0)	0.44 (0.05)	1095 (316)	12.9 (3.8)	79.6 (16.1)	32.7 (14.5)
	July '11	240.4 (6.9)	15.5 (0.7)	35.6 (1.6)	11.6 (0.4)	0.15 (0.01)	563 (36)	0.68 (0.08)	74.7 (6.0)	10.8 (8.1)
	Oct '11	259.1 (2.0)	14.16 (0.01)	32.8 (0.1)	13.4 (0.1)	0.20 (0.01)	454 (20)	0.56 (0.14)	101.4 (9.6)	BD
	Dec '11	230.2 (6.5)	14.8 (1.7)	31.9 (0.6)	12.5 (0.9)	0.21 (0.14)	411 (217)	BD	65.5 (15.1)	BD
	Mean	**253.1 (23.0)**	**18.6 (7.6)**	**34.6 (2.9)**	**13.2 (1.5)**	**0.25 (0.13)**	**631 (316)**	**NA**	**80.3 (15.2)**	**NA**
OGewV[a]		NG	NG	0.34	NG	NG	NG	34.7	0.7–2.2	NG
WHO[b]		7.3	NG	1.2	NG	0.13	3147	48.3	26.7	962

[a] Given are the environmental quality standards reported in the German ordinance on surface water protection (OGewV, 2011).
[b] Given are WHO drinking water guideline values (WHO, 2011).
ND, not determined. BD, below detection limit. NA, not applicable. NG, not given in the OGewV or WHO guidelines.

Table E.2. Statistical analysis of 16S rRNA gene clone libraries of water from sites I (Iw), II (IIw), and III (IIIw) as well as of sediment from sites II (IIs) and III (IIIs), derived from DNA extracts.

Site	Library	No. of clones	No. of OTUs	Coverage
I	Iw	88	21	86%
II	IIw	73	38	78%
III	IIIw	89	53	63%
II	IIs	91	21	89%
III	IIIs	88	5	98%

OTU, operational taxonomic unit.

Table E.3. Bacterial 16S rRNA gene sequences detected in clone libraries from water (w) and sediment (s) of sites I-III in the former Ronneburg mining district with their phylogenetic group, the closest isolated relative and the number of clones in the respective libraries.

OTU (no. of clones; accession[a])	Phylogenetic group	Closest isolated relative (accession[a]; sequence identity)	No. of clones in respective library (relative abundance in %)					
			all	Iw	IIw	IIIw	IIs	IIIs
1(71; KF424837), 3(2; KF424838), 4(9; KF424839), 6(123; KF424840), 8(1; KF424842), 10(2; KF424844), 12(23; KF424846), 16(1; KF424850), 19(2; KF424853), 83(2; KF424912), 88(1; KF424917), 98(3; KF424924), 99(1; KF424925), 110(1; KF424935), 124(1;KF424946), 136(2; KF424956), 145(2;KF424964), 153(1; KF424972), 159(1;KF424978), 162(2; KF424981)	Betaproteobacteria	'*Gallionella capsiferriformans* ES-2'^{T} (DQ386262; 93–99%; **FeOB**[b])	251 (58.5)	51	23	23	74	80
66(7; KF424895), 86(3; KF424915), 104(9; KF424929)	Deltaproteobacteria	*Geobacter psychrophilus*^{T} (AY653549; 97–99%; **FeRB**[b])	19 (4.4)	6	7	6		
11(15; KF424845), 13(1; KF424847), 102(1; KF424927), 103(1; KF424928)	Betaproteobacteria	*Sideroxydans paludicola*^{T} (DQ386858; 94–96%; **FeOB**)	18 (4.2)	5	6	1	6	
20(1; KF424854), 24(15; KF424858), 53(1; KF424883), 160(1; KF424979)	Betaproteobacteria	'*Sideroxydans lithotrophicus* ES-1'^{T} (DQ386264; 94–96%; **FeOB**)	18 (4.2)		7	4	1	6
17(6; KF424851), 58(2; KF424887), 109(1; KF424934)	Deltaproteobacteria	Bacterium EtOHpelo (AY771935; 82–95%)	9 (2.1)	2	5	1	1	
79(4; KF424908), 93(1; KF424921), 139(2; KF424958)	Betaproteobacteria	*Gallionella ferruginea*^{T} (L07897; 95–99%; **FeOB**)	7 (1.6)	2	1	4		
14(2; KF424848), 125(3; KF424947), 149(1; KF424968)	Bacteroidetes	Bacterium XB45 (AJ229237; 88–96%)	6 (1.4)			4	2	
80(5; KF424909), 156(1; KF424975)	Ignavibacteria	*Ignavibacterium album*^{T} (NR_074698; 83%)	6 (1.4)	4		2		
85(3; KF424914), 87(3; KF424916)	Unclassified Bacteria	*Syntrophorhabdus* sp. TB (AB611035; 81%)	6 (1.4)	6				
126(2; KF424948), 146(1; KF424965), 154(1; KF424973)	Betaproteobacteria	*Gallionellaceae* bacterium HDD (HQ263247; 94–96%; **FeOB**)	4 (0.93)			4		
137(4; KF424957)	Unclassified Bacteria	*Desulfovibrio alkalitolerans*^{T} (AY649785; 81%)	4 (0.93)			4		
78(3; KF424907)	Betaproteobacteria	*Methylibium subsaxonicum*^{T}	3 (0.70)	3				

		(NR_042651; 92%)						
64(3; KF424893)	Betaproteobacteria	*Sulfuritalea hydrogenivorans*^{T} (AB552842; 95%)	3 (0.70)		1	2		
117(1; KF424940), 122(1; KF424944), 158(1; KF424977)	Betaproteobacteria	*Thiobacillus* sp. ML2-16 (DQ145970; 94–95%)	3 (0.70)		2	1		
7(2; KF424841), 121(1; KF424943)	Betaproteobacteria	*Thiomonas* sp. DM-Zn2 (DQ419967; 96–98%)	3 (0.70)		2 (1)		1	
23(3; KF424857)	Betaproteobacteria	Bacterium TP701 (EF636141; 99%)	3 (0.70)	2			1	
113(2; KF424937), 118(1; KF424941)	Bacteroidetes	*Paludibacter propionicigenes*^{T} (NR_074577; 87–97%)	3 (0.70)		3 (2)			
98(3; KF424924)	Spirochaetes	Bacterium SA-10 (AY695841; 93%)	3 (0.70)		1	2		
116(3; KF424939)	Chloroflexi	*Levilinea saccharolytica*^{T} (NR_040972; 89%)	3 (0.70)		2	1		
95(3; KF424922)	Firmicutes	Bacterium G1 (AY529492; 92%; **FeOB**)	3 (0.70)		3			
128(2; KF424950)	Betaproteobacteria	'*Ferritrophicum* radicicola'^{T} (DQ386263; 93%; **FeOB**)	2 (0.47)			2		
32(2; KF424866)	Deltaproteobacteria	*Geobacter* sp. Ply1 (EF527233; 96%; **FeRB**)	2 (0.47)			2		
129(2; KF424951)	Deltaproteobacteria	*Pelobacter propionicus*^{T} (NR_074975; 97%)	2 (0.47)			2		
120(2; KF424942)	Deltaproteobacteria	*Anaeromyxobacter dehalogenans* (NR_074896; 85%)	2 (0.47)		1	1		
81(2; KF424910)	Acidobacteria	Bacterium IGE-005 (GU187033; 89%)	2 (0.47)	2				
25(2; KF424859)	Bacteroidetes	*Alkaliflexus imshenetskii*^{T} (FR839023; 89%)	2 (0.47)					2
141(2; KF424960)	Firmicutes	*Desulfosporosinus* sp. LauIII (AJ302078; 97%)	2 (0.47)			2		
9(1; KF424843), 155(1; KF424974)	Elusimicrobia	*Elusimicrobium minutum*^{T} (NR_074114; 78–85%)	2 (0.47)			1	1	
150(1; KF424969)	Alphaproteobacteria	Bacterium Schreyahn_AOB_Aster_Kultur_5 (AY795761; 88%)	1 (0.23)			1		
142(1; KF424961)	Alphaproteobacteria	Endosymbiont of *Acanthamoeba* sp. S31 (AB506681; 90%)	1 (0.23)			1		
15(1; KF424849)	Betaproteobacteria	*Gallionella* sp. PN013 (HQ117915; 95%; **FeOB**)	1 (0.23)				1	
161(1; KF424980)	Betaproteobacteria	*Gallionellaceae* bacterium R-1 (JN377592; 98%; **FeOB**)	1 (0.23)			1		
130(1; KF424952)	Betaproteobacteria	'*Ferrovum myxofaciens*'^{T} (HM044161; 94%; **FeOB**)	1 (0.23)			1		
38(1; KF424870)	Betaproteobacteria	*Sideroxydans* sp. CL21 (GU134935; 99%; **FeOB**)	1 (0.23)			1		
91(1; KF424920)	Betaproteobacteria	*Formivibrio citricus*^{T} (NR_026478; 96%)	1 (0.23)	1				
143(1; KF424962)	Betaproteobacteria	*Nitrosospira* sp. Nsp65 (AY123813; 92%)	1 (0.23)			1		
148(1; KF424967)	Betaproteobacteria	*Dechlorobacter hydrogenophilus* (AY124797; 99%)	1 (0.23)			1		
144(1; KF424963)	Gammaproteobacteria	*Legionella* sp. LLAP11 (X97362; 98%)	1 (0.23)			1		
34(1; KF424868)	Gammaproteobacteria	*Rhodanobacter* sp. L12 (FR874232; 99%)	1 (1.23)			1		
115(1; KF424938)	Gammaproteobacteria	*Xanthomonadaceae* sp. X11 (FR874227; 99%)	1 (0.23)		1			

84(1; KF424913)	Deltaproteobacteria	*Desulfobulbus mediterraneus*[T] (NR_025150; 89%)	1 (0.23)	1				
105(1; KF424930)	Deltaproteobacteria	Bacterium JN18_A94_J (DQ168651; 98%)	1 (0.23)		1			
140(1; KF424959)	Deltaproteobacteria	*Smithella propionica*[T] (NR_024989; 91%)	1 (0.23)			1		
21(1; KF424855)	Deltaproteobacteria	Bacterium ROMEm4sh241 (AY998129; 98%)	1 (0.23)				1	
37(1; KF442631)	Deltaproteobacteria	*Geobacter bemidjiensis*[T] (AY187307; 97%; **FeRB**)	1 (0.23)		1			
163(1; KF424982)	Unclassified Proteob.	Bacterium IZ4 (AB539996; 94%)	1 (0.23)			1		
101(1; KF424926)	Acidobacteria	*Geothrix fermentans*[T] (U41563; 99%; **FeRB**)	1 (0.23)		1			
152(1; KF424971)	Acidobacteria	Bacterium Ellin5237 (AY234588; 98%)	1 (0.23)			1		
90(1; KF424919)	Bacteroidetes	*Prolixibacter bellariivorans*[T] (NR_043273; 88%)	1 (0.23)	1				
151(1; KF424970)	Bacteroidetes	Bacterium 4F6B (AB623230; 92%)	1 (0.23)			1		
29(1; KF424863)	Actinobacteria	Bacterium BGR 72 (GU167995; 88%)	1 (0.23)			1		
22(1; KF424856)	Ignavibacteria	*Melioribacter roseus*[T] (NR_074796; 89%)	1 (0.23)				1	
82(1; KF424911)	Gemmatimonadetes	Bacterium Ellin5290 (AY234641; 91%)	1 (0.23)	1				
107(1; KF424932)	Spirochaetes	*Spirochaeta zuelzerae*[T] (FR749929; 96%)	1 (0.23)		1			
132(1; KF424953)	Chloroflexi	*Dehalogenimonas lykanthroporepellens*[T] (NR_074337; 85%)	1 (0.23)			1		
134(1; KF424955)	Firmicutes	*Desulfosporosinus* sp. 44a-T3a (AY082482; 98%)	1 (0.23)			1		
147(1; KF424966)	Nitrospirae	*Thermodesulfovibrio yellowstonii*[T] (NR_074345; 89%)	1 (0.23)			1		
18(1; KF424852)	Armatimonadetes	*Armatimonas rosea* (AB529679; 84%)	1 (0.23)				1	
123(1; KF424945)	Unclassified Bacteria	*Moorella* sp. CF4 (HM228402; 89%)	1 (0.23)		1			
108(1; KF424933)	Unclassified Bacteria	*Cytophaga* sp. Dex80-64 (AJ431235; 87%)	1 (0.23)		1			
89(1; KF424918)	Unclassified Bacteria	*Desulfobacca acetoxidans*[T] (NR_074955; 83%)	1 (0.23)	1				
127(1; KF424949)	Unclassified Bacteria	*Anaeromyxobacter dehalogenans* DCP20-E (EU331405; 85%)	1 (0.23)			1		
133(1; KF424954)	Unclassified Bacteria	*Desulfuromonas svalbardensis* strain 60 (AY835390; 82%)	1 (0.23)			1		
106(1; KF424931)	Unclassified Bacteria	*Candidatus Desulforudis audaxviator* MP104C (NR_075067; 81%)	1 (0.23)		1			
112(1; KF424936)	Unclassified Bacteria	Bacterium Ellin504 (AY960767; 86%)	1 (0.23)		1			
157(1; KF424976)	Unclassified Bacteria	Bacterium YJF1-16 (FJ405900; 77%)	1 (0.23)			1		
All			**429**	**88**	**73**	**89**	**91**	**88**

[a] Given are the accession numbers for sequences in the GenBank database.
[b] "**FeOB**" or "**FeRB**" behind the accession number of the isolated representatives indicate if the organism is a reported FeOB (iron-oxidizing bacterium) or FeRB (iron-reducing bacterium), respectively.
OTU, operational taxonomic unit. Proteob., Proteobacteria.

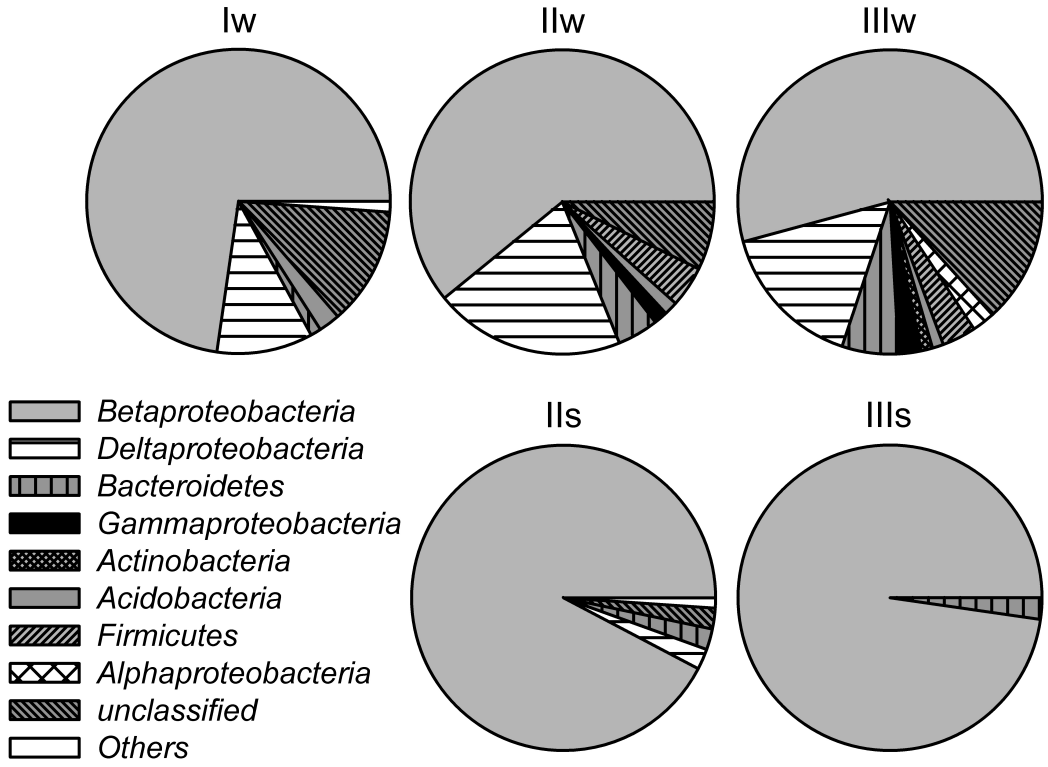

Figure E.1. Bacterial community composition of water from sites I (Iw), II (IIw), and III (IIIw) as well as of sediment from sites II (IIs) and III (IIIs) in the former uranium-mining district near Ronneburg, Germany. Calculations were based on the number of clone sequences affiliated with sequenced representatives at the phylum level, or class level for *Proteobacteria*, in 16S rRNA gene clone libraries. The low abundance groups (<1% of all clone sequences) *Spirochaetes*, *Chloroflexi*, *Gemmatimonadetes*, *Nitrospirae*, *Elusimicrobia*, *Armatimonadetes*, and unclassified *Proteobacteria* are included in the category "others".

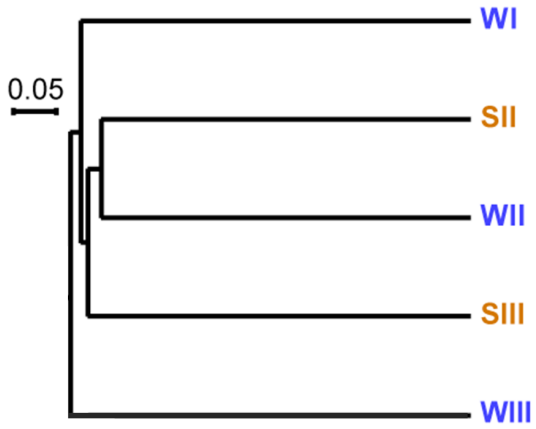

Figure E.2. Similarities of 16S rRNA gene clone libraries of water from sites I (WI), II (WII), and III (WIII) or sediment from sites II (SII) and III (SIII) in the former Ronneburg uranium-mining district, based on Jaccard Similarity values.

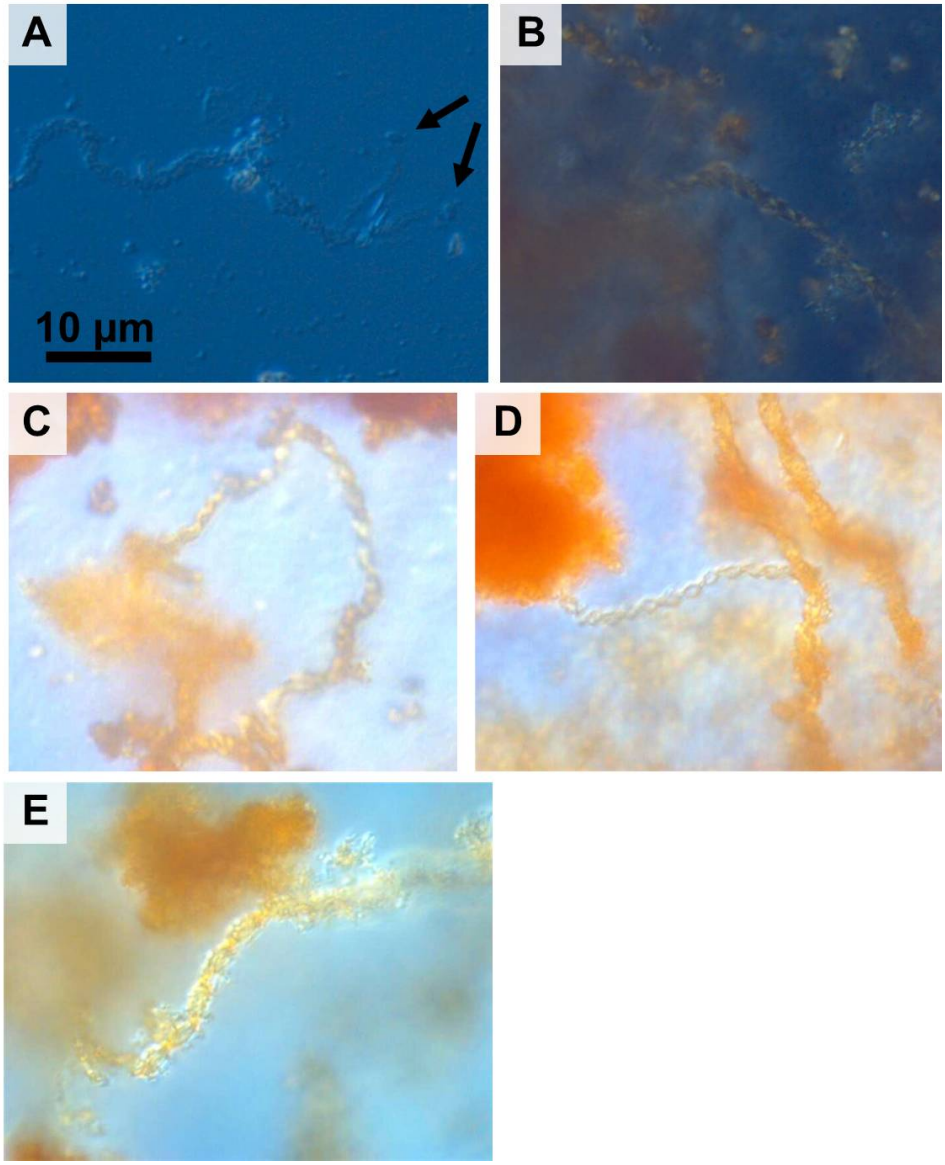

Figure E.3. Light microscopy of *Gallionella*-like twisted stalks from water or sediment. (A) site I water, (B) site II water, (C) site III water, (D) site II sediment, (E) site III sediment. The arrows in A indicate bacterial cells still attached to the ends of the bifurcated stalk.

References

OGewV (2011) Oberflächengewässerverordnung (Surface Water Protection Ordinance). German Federal Ministry of Justice, Available online at: http://www.gesetze-im-internet.de/ogewv/BJNR142900011.html.

WHO (2011) Guidelines for drinking-water quality. World Health Organization Press, Geneva, Switzerland.

APPENDIX F. PERMISSION LETTERS

Approval from CSIRO Publishing to include Ch.2. and Appendix A in this dissertation:

RE: Request to include EN13184 in dissertation - Our Ref: CP2014-154
1 message

Carla.Flores@csiro.au <Carla.Flores@csiro.au> Tue, Sep 2, 2014 at 8:35 PM

To: cjohns49@vt.edu

Dear Carol

Yes, this is fine. You may include your *Environmental Chemistry* paper (as noted below) in your dissertation, provided the appropriate acknowledgement of the source, the authors and CSIRO Publishing is given, including citing the link to your paper on our website. The link is: http://www.publish.csiro.au/nid/188/paper/EN13184.htm.

Should you decide to include the published PDF of your paper, you may do so, however, the PDF must not be stored in any retrieval systems as a stand-alone document; it should always remain part of your thesis.

As a courtesy to your co-authors, you may wish to advise them of their inclusion of the paper in your thesis.

Thank you for seeking our permission.

Good luck with your dissertation.

With best wishes,

Carla

Carla Flores
Rights & Permissions
CSIRO Publishing
E carla.flores@csiro.au T + 61 3 9662 7652 F +61 3 9662 7555
150 Oxford Street (PO Box 1139), Collingwood VIC 3066
www.csiro.au
www.publish.csiro.au

Approval from the U.S. Geological Survey to use Appendices D and E in this dissertation:

From: **Breen, Kevin** <kjbreen@usgs.gov>
Date: Wed, Sep 3, 2014 at 4:56 PM
Subject: Re: Routing task assigned to you for IP-059557
To: Denise Akob <dakob@usgs.gov>
Cc: Harry Jenter <hjenter@usgs.gov>, Pierre Glynn <pglynn@usgs.gov>, Carl LaFrance <clafrance@usgs.gov>, Callie Oblinger <oblinger@usgs.gov>

Dear Denise:
I have completed the requested expedited review on the subject manuscript. It is in great shape and is approved.
The approved files are in the Information Product Data System (IPDS). I had just a few comments in the text file.
Line 26-29--with approval, the predecisional disclaimer can be removed from the thesis material.
Line 394--the wording "...metals were already sedimented in the terraces..." might be viewed by some readers as awkward. Consider "...metals were already incorporated in the sediments of the terraces..." as an alternative.
Tables 1 and 2, titles--minor rewording suggestions are offered.

Please call or write if you have any questions. I did not prepare a memo on this approval.
Best regards,
Kevin

Kevin J. Breen
Bureau Approving Official, Hydrologist
Office of Science Quality and Integrity
U.S. Geological Survey
215 Limekiln Rd.
New Cumberland, PA 17070
w: 717.730.6970
c: 717.571.8940